

LITHOSPHERIC STRUCTURE OF THE WESTERN TURKEY
AND AEGEAN REGION

by

Tuğçe Ergün

B.S., Geophysical Engineering, İstanbul Technical University, 2002

M.S., Geophysics, Boğaziçi University, 2006

Submitted to the Kandilli Observatory and
Earthquake Research Institute in partial fulfillment of
the requirements for the degree of
Doctor of Philosophy

Graduate Program in Geophysics

Boğaziçi University

2019

Dedicated to my father Sierdem AFACAN,

ACKNOWLEDGEMENTS

I would like to express my deepest appreciation to my advisor Prof. Hayrullah Karabulut for his guidance and encouragement. I am grateful to him for his endless support and patience during my PhD study. It is always a pleasure to be one of his students and work with him.

This research and the related field work would not have been possible without the support from Boğaziçi University, Kandilli Observatory and Earthquake Research Institute, TÜBİTAK-Marmara Research Center and Republic of Turkey Prime Ministry Disaster & Emergency Management Presidency. Special thanks to Dr. Anne Paul from the Institute des Sciences de la Terre (France) for providing the SIMBAAD data (funded by ANR France, contract 06-BLAN-0317). She also provided guidance on receiver function analysis

I also want to express my gratitude to the department members of National Earthquake and Tsunami Monitoring Centre and Geophysics department; for tolerating me through the tough times. I would like to sincerely thank to Prof. Cemil Gürbüz who has been a second father to me, for his incredible guidance and supporting me in a lot of different ways.

I am deeply indebted to my long-term friend, Doğan Aksarı like brother to me whose assistance and encouragement made this work possible towards the end, life wouldn't be easy without the support of him. I feel myself privileged to know my dearest friend Dr. Ugur Mustafa Teoman, would like to thank for his endless support during the hard times of this study and my life. I would like to thank Dr. Selda Altuncu Poyraz who made my life so easier with her support.

Finally I would like to thank to my dear spouse Gürsoy Ergün. He turned my dreadful times to feast with his limitless tolerance and patience. I would not be myself without him. I would like to thank to my son Kıvanç, to my mother Güngör Afacan, to my aunt Gönül İyigün, to my sister Nur Darga and to my huge family for being in my life and for their endless support.

ABSTRACT

LITHOSPHERIC STRUCTURE OF THE WESTERN TURKEY AND AEGEAN REGION

Aegean-Anatolia region undergoes an intense internal deformation as evidenced by the existence of major active faults, intense seismic activity and the marked thinning of the crust. It makes the region center of attraction to the study the interaction between the deep structure with the surface deformation. The aim of this study is to provide constraints on the crustal and uppermost mantle structure by using seismic data of permanent broad-band network of Kandilli Observatory and Earthquake Research Institute (KOERI-RETMC), and a temporary array of Seismic Imaging beneath Aegean-Anatolia Domain (SIMBAAD) experiment. Seismic stations of Republic of Turkey Prime Ministry Disaster and Emergency Management Presidency (AFAD), Incorporated Research Institutions for Seismology (IRIS) and previous experiment called Western Anatolia Seismic Recording Experiment (WASRE) were used to complement the network. In this regard we present two high resolution lithospheric images along a ~650 km transect crossing western Anatolia at 28°E longitude from the Black Sea to the Mediterranean and a ~550 km transect crossing central Anatolia at 30.5°E longitude. A total of 5250 receiver functions are computed from the records of teleseismic earthquakes at 40 broadband seismic stations for each of the profiles with an average spacing of ~15 km. Lateral variations of crustal thickness, V_p/V_s are inferred from both H-K, and common conversion point stacks (CCP). In order to have a better idea on the accuracy of the estimated crustal parameters we also performed a search scheme based on the Neighborhood Algorithm. The receiver functions are inverted for a 1-D layered medium to determine the layer thicknesses, V_s and V_p/V_s . The CCP images reveals a long-wavelength variations of Moho depth from ~31 km in the Thrace basin to ~25 km beneath the Marmara Sea, ~25 km beneath the Menderes Massif and ~20 km on the coast of the Mediterranean on the western Anatolia transect. On the eastern transect, a smooth Moho topography is observed with a sharp discontinuity at depths ranging from 34 km beneath the Black Sea coast, ~35 km beneath the Sakarya Zone with mafic composition to 43 km beneath the Antalya Bay on the central Anatolia profile. The Moho of the subducted African lithosphere is imprinted between ~40 and ~60 km depth at the southern end of the western

Anatolia profile, dipping northward where the subducted Cyprus lithosphere is observed dipping northward with an angle of 40° between ~ 40 and ~ 100 km depths beneath the Antalya Bay on the central Anatolia transect.

ÖZET

BATI TÜRKİYE VE EGE BÖLGESİNİN LİTOSFERİK YAPISI

Ege-Anadolu bölgesi, aktif fayların varlığı, yoğun sismik aktivite ve kabuğun belirgin şekilde incilmesi ile kendini gösteren yoğun bir deformasyona maruz kalmaktadır. Bu durum bölgeyi, yüzey deformasyonunu derin yapılar ile ilişkilendirmek adına cazibe merkezi kılar. Çalışmanın amacı, kabuk ve üst manto yapısına ilişkin çeşitli parametreleri, Kandilli Rasathanesi ve Deprem Araştırma Enstitüsü (KOERI-RETMC) ve Ege-Anadolu bölgesi sismik görüntüleme deneyi (SIMBAAD) verilerini kullanarak hesaplamaktır.

Sismik ağı tamamlamak ve daha yoğun hale getirmek adına Türkiye Cumhuriyeti Başbakanlık Afet ve Acil Durum Yönetimi Başkanlığı'nın (AFAD) sismik istasyonları, Birleşmiş Sismoloji Araştırma Kurumları (IRIS) ve Batı Anadolu Sismik Kayıt Deneyi (WASRE) nin bazı istasyonları çalışmaya dahil edilmiştir. Bu bağlamda, batı Anadolu'da 28°D boylamından geçen Karadeniz'den Akdeniz'e kadar uzanan yaklaşık 650 km ve orta Anadolu'da 30.5°D boylamından geçen yaklaşık 550 km uzunluğunda iki profil boyunca yüksek çözünürlüklü litosferik görüntüler elde edilmiştir. Her bir profilede ortalama istasyon aralığı 15 km olup 40 geniş bant istasyonda kaydedilmiş teleseismik deprem kayıtlarından toplam 5250 alıcı fonksiyonu hesaplanmıştır. Kabuk kalınlığının yanal değişimleri ve Vp/Vs oranları hem H-K hem de CCP yöntemleri kullanılarak elde edilmiştir. Elde edilen kabuk parametrelerinin doğruluğu komşuluk algoritması (NA) kullanılarak test edilmiştir. Alıcı fonksiyonlar, tabaka kalınlıklarını, Vs ve Vp/Vs oranlarını belirlemek için 1-B katmanlı bir ortamda ters çözülmüştür. CCP görüntüleri, Batı Anadolu profili için Moho derinliğinin, Trakya havzasında ~30 km'den, Marmara Denizi altında ~25 km'ye, Menderes Masifi'nin altında ~28 km'den Akdeniz kıyılarında ~20 km'ye kadar olan değişimini ortaya koymaktadır. Profil boyunca ortalama Moho derinliği 27km ve ortalama Vp/Vs 1.78 dir. Orta Anadolu profilinde ise Moho derinliği, Karadeniz kıyılarının altında 34 km, Sakarya Bölgesi'nin altındaki mafik kompozisyonda ~35 km ile Antalya Körfezi'nin altında yaklaşık 43km'dir. Profil boyunca ortalama Vp/Vs değeri 1.85 dir. Afrika litosferi, Batı Anadolu profilinin güney ucunda ~40 ila ~60 km derinliğinde kuzeye doğru dalmaktadır. Kıbrıs

litosferi ise orta Anadolu profilinde Antalya K rfezinin altında, kuzeye dođru yaklaşık 40⁰ açı ile ~40 ila ~100km derinlikleri arasında dalmaktadır.

TABLE OF CONTENTS

ACKNOWLEDGEMENTS.....	iv
ABSTRACT.....	v
ÖZET.....	vii
TABLE OF CONTENTS	ix
LIST OF FIGURES.....	xi
LIST OF TABLES	xviii
LIST OF SYMBOLS	xix
LIST OF ACRONYMS / ABBREVIATIONS.....	xxi
1. INTRODUCTION	1
2. REGION OF INTEREST: WESTERN TURKEY AND AEGEAN REGION.....	4
2.1. Geology And Tectonic Settings.....	4
2.1.1. Tectonics	4
2.1.2. Local Geology	9
2.2. Previous Studies.....	14
2.3. Seismicity	16
3. METHODOLOGY.....	20
3.1. Receiver Function	20
3.1.1. Frequency Domain RF Estimation	22
3.1.2. Iterative Time Domain RF Estimation.....	24
3.2. H-K Stacking	26
3.3. Common Conversion Point Stackking	28
3.4. 1-D Inversion	31
3.4.1. Voronoi Cells	33
3.4.2. The Behavior of the Neighborhood Search Algorithm.....	34
3.4.3. The Gibbs Sampler	35
3.4.4. Sampling Voronoi cells using exact intersections.....	37
3.4.5. Finding acceptable models with NA.....	38
4. DATA ACQUISITION AND PROCESSING	40
4.1. Data And Earthquake Distribution.....	40
4.2. Receiver Function Computation	43

5.	RECEIVER FUNCTION ANALYSIS	47
5.1.	H-K Stacking	47
5.2.	1-D Inversion	52
5.3.	Crustal Thickness Maps	57
5.4.	CCP Imaging.....	59
5.4.1.	Western Anatolia Profile (WAP).....	59
5.4.1.1.	Results	63
5.4.1.1.	Discussion.	67
5.4.2.	Central Anatolia Profile	73
5.4.2.1.	Results	76
5.4.2.1.	Discussion.	79
6.	CONCLUSIONS.....	84
	REFERENCES	86
	APPENDIX A: Station Coordinates and Parameters of Crustal Structure.....	100

LIST OF FIGURES

- Figure 2.1. Tectonic map of the Aegean and Anatolian region showing the main active structures (black lines), the main sutures zones (thick violet or blue lines), the main thrusts in the Hellenides where they have not been reworked by later extension (thin blue lines), the North Cycladic Detachment (NCDS, in red) and its extension in the Simav Detachment (SD), the main metamorphic units and their contacts; AIW: Almyropotamos window; BD: Bey Daglari; CB: Cycladic Basement; CBBT: Cycladic Basement basal thrust; CBS: Cycladic Blueschists; CHSZ: Central Hellenic Shear Zone; CR: Corinth Rift; CRMC: Central Rhodope Metamorphic Complex; GT: Gavrovo–Tripolitza Nappe; KD: Kazdag dome; KeD: Kerdylion Detachment; KKD: Kesebir–Kardamos dome; KT: Kephallonia Transform Fault; LN: Lycian Nappes; LNBT: Lycian Nappes Basal Thrust; MCC: Metamorphic Core Complex; MG: Menderes Grabens; NAT: North Aegean Trough; NCDS: North Cycladic Detachment System; NSZ: Nestos Shear Zone; OIW: Olympos Window; OsW: Ossa Window; OSZ: Ören Shear Zone; Pel.: Peloponnese; ÖU: Ören Unit; PQN: Phyllite–Quartzite Nappe; SiD: Simav De- tachment; SRCC: South Rhodope Core Complex; StD: Strymon Detachment; WCDS: West Cycladic Detachment System; ZD: Zaroukla Detachment (Jolivet et al., 2013)..... 5
- Figure 2.2 GPS-derived velocities with respect to Eurasia (velocity field has been decimated for clarity). GPS velocity uncertainties are 95% confidence ellipses. (Reilinger et al., 2006)..... 7
- Figure 2.3. Major terranes in the Aegean and Anatolian regions, modified after Moix et al. (2008). Afyon/mln/dn=Afyon zone, Ören Unit and Dilek Nappe; NAFZ=North Anatolian Fault Zone; NAT = North Aegean Trough; PST = Pliny & Strabo Trenches (South Aegean left-lateral strike-slip system) (Hinsbergen et al., 2010)..... 10

Figure 2.4.	Seismicity of the eastern Mediterranean region for the period of 1975-2018, earthquakes with magnitudes greater than 4.0 (EMSC Catalog).....	17
Figure 2.5.	Focal mechanisms of earthquakes over the Aegean Anatolian region (Joviet et al., 2013).	18
Figure 3.1.	The amplitudes and the arrival times of converted phases and multiples depend on the Pwave incidence angle, depth of the velocity contrast m (Cassidy, 1992). (a) The conversions (Ps) and multiples (PsPms (PpPs), PpSms (PpSs), and PpPms (PpPs)) on the RF and (b) the corresponding ray paths (Zor, 2002).	21
Figure 3.2.	Schematic expression of a teleseismic event in the layered earth (Top). Displacement response as the convolution of source, structure and instrument (Bottom).	22
Figure 3.3.	Schematic representation of CCP migration. Left, computed RF trace in its theoretical path. Right, its mesh gridded amplitudes (red indicates positive, blue indicates negative) (Hetenyi, 2007 PhD).	30
Figure 3.4.	(a) 10, (b) 100 and (c) 1000 random points and their Voronoi cells. (d) Contour of the test function. The black areas represent the minima (Sambridge, 1999a).	34
Figure 3.5.	A uniform random walk in the shadowed Voronoi cell by using a Gibbs sampler. The conditional probability density function (PDF) plotted above, outside the cell is zero (Sambridge, 1999a).....	36
Figure 4.1.	Permanent and temporary seismic stations deployed during the 2007–2009 SIMBAAD experiment. Green and yellow stars in the circles are the medium band stations on the profiles, red stars in the circles are the SIMBAAD broadband stations and blue triangles represents the permanent networks.....	40

Figure 4.2.	Equidistant projection of the locations of teleseismic events used in this study.....	42
Figure 4.3.	Vertical component waveforms of a teleseismic event from Pacific subduction zone at 05:00:00 h on 2008 July 17 (distance 57° , depth 120 km and magnitude $M_w=6.7$). The waveforms are aligned to the first P-onset time.	43
Figure 4.4.	Data preparation steps.....	44
Figure 4.5.	Two examples of computed radial and transverse receiver functions for stations BALB and W18.	46
Figure 5.1.	Top: RFs at station BLCB sorted by epicentral distance and backazimuth. Traces in every 0.4° are displayed. H-k stack of the RFs with estimated V_p/V_s and crustal thickness. Uncertainties of H (0.5 km) and k (0.03) are presented in the H-k stack. Bottom: Travel time observations of local earthquakes recorded at station BLCB. The average crustal V_p and V_s values are estimated from the slope of the related travel time curves (red dotted line: $V_p = 6.4$ km/s, blue dotted line: $V_s = 3.7$ km/s).....	50
Figure 5.2.	Top: RFs at station BALB sorted by epicentral distance and backazimuth. Traces in every 0.4° are displayed. H-k stack of the RFs with estimated V_p/V_s and crustal thickness. Bottom: Travel time observations of local earthquakes recorded at station BALB. The average crustal V_p and V_s values are estimated from the slope of the related travel time curves (red dotted line: $V_p = 6.2$ km/s, blue dotted line: $V_s = 3.5$ km/s).....	51
Figure 5.3.	RFs at station LOD sorted by epicentral distance and backazimuth. Traces in every 0.4° are displayed. H-k stack of the RFs with estimated V_p/V_s and crustal thickness.	52
Figure 5.4.	Inversion of the receiver function of the BLCB broadband station for the shear wave velocity structure using the neighborhood algorithm. Top:	

Density plot of the best 1000 data-fitting S-velocity models generated with the first random seed. The best data fitting model is plotted in red. The colour scale shows the increase in data-fit, from yellow to green. Bottom: RFs of the true (black) and best fit models (blue). 54

Figure 5.5. Inversion of the receiver function of the BALB broadband station for the Shear wave velocity structure using the neighborhood algorithm. Top: Density plot of the best 1000 data-fitting S-velocity models generated with the first random seed. The best data fitting model is plotted in red. The colour scale shows the increase in data-fit, from yellow to green. Bottom: RFs of the true (black) and best fit models (blue). 55

Figure 5.6. Inversion of the receiver function of the LOD broadband station for the Shear wave velocity structure using the neighborhood algorithm. Top: Density plot of the best 1000 data-fitting S-velocity models generated with the first random seed. The best data fitting model is plotted in red. The colour scale shows the increase in data-fit, from yellow to green. Bottom: RFs of the true (black) and best fit models (blue). 56

Figure 5.7. Top: The map of the seismic stations used in this study. The colors indicate the crustal thicknesses estimated from receiver function analysis. Bottom: the crustal thickness map computed from the receiver function measurements at stations shown in top figure. The crustal thickness estimates for the Black Sea (Starostenko et al. (2004); Yegorova et al. (2013)) are included prior to interpolation. Blue color indicates the thick crust (>40 km), while red colors indicate thin crust (<30 km). 58

Figure 5.8. Seismic stations of WAP installed during SIMBAAD experiment between 2007-2008, blue stars indicates the location of the stations. Main tectonic features and morpho-tectonic units are also labeled; ATB, Anatolide-Tauride Block; AZ, Afyon Zone; BFZ, Bornova Flysh Zone; BMG, Büyük Menderes Graben; GG, Gediz Graben; GB: Gökova Bay; Gg, Gökova Graben; SG, Simav Graben; IZ, Istanbul Zone; LN, Lycian Nappes; MM, Menderes Massif; PT, Pontides; RS, Rhodope-Strandja

Basin; SZ, Sakarya Zone; IASZ, Izmir-Ankara Suture Zone; Ms, Marmara Sea; Mi, Marmara Island; NAFZ, North Anatolian Fault Zone; Ri, Rhodos Island; ThB, Thrace Basin; TZ, Tavşanlı Zone. Stures are shown by red lines with black triangles on. The main normal faults of the grabens are shown by the thin light blue lines. The magenta line shows the NAF. The ophiolite outcrops labeled with dark green units. Western Anatolia profile shown as a blue line. Geological map modified from Okay and Tüysüz, 1999, and van Hinsbergen et al, 2010 (Karabulut et al., 2013)..... 60

Figure 5.9. Migrated depth sections of Ps (a), PpPs (b) and PpSs+PsPs (c) modes. The black line shows the crust-mantle boundary..... 63

Figure 5.10. Migrated depth section of radial receiver function records of the WAP. Distance is measured with respect to the northernmost station. (a) Topography profile (black), receiver locations (magenta) and Bouguer gravity anomaly (red). (b) Geological units along the profile (c) Common-conversion point depth migrated cross-section (no vertical exaggeration). Red represents positive P-to-S converted amplitudes and indicates sharp increase in velocity with depth. The Moho is the continuous band between 26 and 32 km depth. (d) Common-conversion point depth migrated cross-section with seismicity and major interpreted structures (vertical exaggeration 2). The seismic activity covers a period from 1998 to 2010 with magnitudes $M_l > 3.0$. (e) Ratio R of stacking amplitudes for each station. (f) Crustal thickness (black) and V_p/V_s (red) variations. (g) 20 sec Love wave group velocities (red) and P_n velocities (black). Same abbreviations as in Figure 5.8. 64

Figure 5.11. (a) Synthetic-CCP-migrated depth section computed from the crustal thickness and V_p/V_s models estimated in this study (Appendix A Table 1). (b) Synthetic-CCP-migrated depth section zoomed for the upper part of model response. (c) Model geometry and V_p/V_s used for the synthetic CCP depth section. Layer parameters for the subducting plate; $V_p = 6.7$ km/s, $H = 15$ km. 69

- Figure 5.12. Seismic stations of Central Anatolia profile installed during SIMBAAD experiment, blue stars are temporary and white stars are permanent stations. Main tectonic features and morpho-tectonic units are also labeled; ATB, Anatolide-Tauride Block; AZ, Afyon Zone; BFZ, Bornova Flysh Zone; BMG, Büyük Menderes Graben; GG, Gediz Graben; GB: Gökova Bay; Gg, Gökova Graben; SG, Simav Graben; IZ, Istanbul Zone; LN, Lycian Nappes; MM, Menderes Massif; PT, Pontides; RS, Rhodope-Strandja Basin; SZ, Sakarya Zone; IASZ, Izmir-Ankara Suture Zone; Ms, Marmara Sea; Mi, Marmara Island; NAFZ, North Anatolian Fault Zone; Ri, Rhodos Island; ThB, Thrace Basin; TZ, Tavşanlı Zone. Stures are shown by red lines with black triangles on. The main normal faults of the grabens are shown by the thin light blue lines. The magenta line shows the NAF. The ophiolite outcrops labeled with dark green units. Western Anatolia profile shown as a blue line. Geological map modified from Okay and Tüysüz, 1999, and van Hinsbergen et al, 2010, Karabulut et al., 2013. 74
- Figure 5.13. Migrated depth sections of Ps (a), PpPs (b) and PpSs+PsPs (c) modes. Moho is labeled with a black line..... 76
- Figure 5.14. Central Anatolia profile CCP results, migrated depth sections. (a) Topography profile (black), receiver locations (magenta) and Bouguer gravity anomaly (red). (b) Geological units along the profile (c) Common-conversion point depth migrated cross-section (no vertical exaggeration). Red represents positive P-to-S converted amplitudes and indicates sharp increase in velocity with depth. (d) Common-conversion point depth migrated cross-section with seismicity and major interpreted structures (vertical exaggeration 2). The seismic activity covers a period from 1998 to 2012 with magnitudes $M_l > 3.0$. (e) Ratio R of stacking amplitudes for each station. (f) Crustal thickness (black) and V_p/V_s (red) variations. (g) 20 sec Love wave group velocities (red) and Pn velocities (black). Same abbreviations as in Figure 5.12. 77

Figure 5.15. (a) Synthetic CCP migrated depth section computed from the crustal thickness and V_p/V_s models estimated in this study (Appendix A Table 2). (b) Synthetic CCP migrated depth section zoomed for the upper part of model response; (c) Model geometry and V_p/V_s used for the synthetic CCP depth section. Layer parameters for the subducting plate; $V_p=6.7\text{km/s}$, $H=15\text{km}$; 81

LIST OF TABLES

Table A.1. Western Profile	100
Table A.2. Central Anatolia Profile	101
Table A.3. Broadband Stations	102

LIST OF SYMBOLS

C_M	Matrix that non-dimensionalizes the parameter space
d	Observations
$D(t)$	Displacement response for P wave
$\overline{D_v}(w)$	Complex conjugate of $D_v(w)$
d_j^2	Set of perpendicular distances
$E(t)$	Impulse response of the earth structure
$G(w)$	Gaussian filter
H	Crustal thickness
$I(t)$	Instrument impulse response
K	V_p/V_s ratio
m	Model parameters
n_s	Initial set of random models
n_r	Models with the lowest misfit
n_a	discretization of the axis is
P_s	Converted P wave from Moho discontinuity
s	Unit ramp function
$s(t)$	Synthetic waveform
S	Seismic source function
T_{ps}	Arrival time difference between P_s and P
T_{misfit}	True misfit
T_{FM}	Computational time of forward modelling
T_{NN}	Computational time for nearest neighbor search
V_s	S wave velocity
V_p	P wave velocity
V_{mi}	Voronoi cells
w_i	Weighting factors
x_t	Observed signal
Z	Depth
δ	Dirac delta function

Δ_N	Approximation error
λ	Wavelength
σ_s	Variance of $s(H,K)$
φ	Data fit measure
φ_t	Tolerance level
φ_R	Reversed misfit function,

LIST OF ACRONYMS / ABBREVIATIONS

AFAD	Republic Of Turkey Prime Ministry - Disaster & Emergency Management Authority - Presidential of Earthquake Department
AF	Afyon Zone
BD	Bey Daglari
BFZ	Bornova Flysch Zone
CA	Central Anatolia
CAP	Central Anatolia Pprofile
CB	Cycladic Basement
CBBT	Cycladic Basement Basal Thrust
CBS	Cycladic Blueschists
CCP	Common Conversion Point
CG	Conjugate Gradient
CHSZ	Central Hellenic Shear Zone
CMP	Common Midpoint Stacking
CR	Corinth Rift
CRMC	Central Rhodope Metamorphic Complex
EMSC	European Mediterranean Seismological Center
FBFZ	Fethiye-Burdur Fault Zone
GA	Genetic Algorithm
GG	Gediz Graben
H	Moho Depth
HP-LT	High Pressure-Low Temperature
HT-LP	High Temperature-Low Pressure
IRIS	Incorporated Research Institutions for Seismology
IASP91	A parameterised velocity model that has been constructed to be a summary of the travel time characteristics of the main seismic phases. (Kennett & Engdahl 1991)
K	Vp/Vs Ratio
KD	Kazdag Dome
KKD	Kesebir–Kardamos Dome

KOERI	Kandilli Observatory and Earthquake Research Institute
KT	Kephalonia Transform Fault
LN	Lycian Nappes
LNBT	Lycian Nappes Basal Thrust
MC	Monte Carlo Methods
MCC	Metamorphic Core Complex
MG	Menderes Grabens
MM	Menderes Massif
MMC	Menderes Methamorphic Complex
MMM	Main Menderes Methemorphism
NA	Neighbourhod Algorithm
NAF	North Anatolian Fault
NAFZ	North Anatolian Fault Zone
NAT	North Aegean Trough
NCDS	North Cycladic Detachment System
NEIC	National Earthquake Information Center
OSZ	Ören Shear Zone
ÖU	Ören Unit
PSD	Probability Density Function
PQN	Phyllite–Quartzite Nappe
RF	Receiver Function
RETMC	Regional Earthquake-Tsunami Monitoring Center
SA	Simulated Annealing
SAC	Seismic Analysis Code
SiD	Simav Detachment
SIMBAAD	Seismic Imaging of the Mantle beneath the Aegean-Anatolian Domain
SF	Sultandagi Fault
Sid	Simav Detachment
SIMBAAD	Seismic Imaging of the Mantle beneath the Aegean-Anatolian Domain
SRCC	South Rhodope Core Complex
ThB	Thrace Basin
TZ	Tavşanlı Zone
TÜBİTAK	The Scientific and Technological Research Council of Turkey

USGS	United States Geological Survey
WA	Western Anatolia
WARSE	Western Anatolia Seismic Recording Experiment
WAP	Western Anatolia Profile
WAEP	Western Anatolia Extensional Province
WCDS	West Cycladic Detachment System
ZD	Zaroukla Detachment

1. INTRODUCTION

It is widely recognized that the continental crust is a combination of brittle upper crust and a lower crust where deformation takes place in the form of ductile flow. However, the transition from brittle to ductile zone and the coupling of these zones are not always clear. Clarifying these concepts has significant implications for relating surface observations to deep processes and understanding continental dynamics. To accomplish this goal, earth scientists have adopted numerous seismological techniques and extracted valuable information from the earth's crust, mantle and core with the use of indirect observations (Thurber, 1993). In this sense, teleseismic receiver functions (RFs) have been introduced about three decades ago (Langston, 1977a; 1977b). For the last twenty years, it has become an accepted standard for imaging the lithospheric structure of the earth underneath the station by using the information from teleseismic earthquakes recorded at a three component seismograph (Langston, 1979; Owens et al., 1984; Ammon, 1990, 1991). The RF technique has several advantages such as; structures are illuminated by waves from below, thus the penetration depth is not limited; signals are strong with an intermediate frequency range (>1 Hz), therefore they are not sensitive to small scale (sub-kilometer) heterogeneities and still have high enough spatial resolution (a few kms) to detect important structural variations; rays have steep incident angles, which lead to high lateral resolution capability; the primary P-to-S converted waves travel only one way from target to receiver and are therefore less contaminated by shallow heterogeneous structures; the technique benefits from travel time differences between the direct P wave and latter P-to-S converted waves (Zhu, 2002).

Recent RF studies (Kind et al., 2015, Vanacore et al., 2013, Tezel et al., 2013) shed light on the crustal thickness variations and the Moho topography, which plays an important role in comprehending the process in extensional regions such as western Anatolia. Western Anatolia-Aegean province and central Anatolia is a natural laboratory to study the relationship between the surface deformation and flow in the asthenospheric mantle and the induced strain at the base of the lithospheric mantle. Numerous seismological studies have been extensively performed in order to provide valuable insights on the lithospheric structure of the region, which is experiencing a large variety of complex tectonic processes such as

subduction, basin and range type pervasive roughly north-south continental extension, strike slip faulting and rotation of different blocks and micro-plates.

In this research, our primary objective is to provide insights on the mechanisms of continental deformation with high resolution images of lithospheric structures along western and central Turkey. Determination of reliable Moho depth maps and V_p/V_s ratios will also lead us to put accurate constraints on the African lithospheric structure beneath western Turkey and Aegean region. The area has been experiencing a large variety of tectonic processes such as the most active continental N-S extension since late Oligocene and located at the junction region of two subducting slabs along Hellenic and Cyprus arcs. In this respect, we adopted CCP technique (Zhu, 2000; Zhu et al., 2006) to image the crustal structure along the profiles, which is an effective technique for subsurface imaging of both shallow and deep crustal structures. Moreover, the dense spatial coverage of the profiles is highly required to delineate velocity discontinuities in the mantle such as the boundaries of the subducting slabs or the mantle heterogeneities.

In chapter two, region of interest will be extensively overviewed in terms of tectonics, local geology, previous seismological studies and seismicity. The present-day geodynamics of Turkey, the tectonic processes related with the surface deformation, seismicity of the region together with the previous seismic studies will be explained in detail.

Chapter three consists of basic receiver function definitions, converted waves, their generation and propagation characteristics and relevant receiver function techniques, Moho depth (H)- V_p/V_s (K) ratio stacking technique, common conversion point technique (CCP) and neighborhood search algorithm.

In chapter four, data acquisition and receiver function computation will be displayed. Data, the geometry of the profiles and the computation steps of RFs will be explained.

Chapter five includes the construction and results of H-K stacks, 1-D inversion results, crustal thickness maps and CCP images. Two dense transects crossing the Turkey from Black sea coast to Mediterranean will be presented in detail. Derived CCP images, crustal

thicknesses, V_p/V_s ratios, imprints of the subducting African and Cypryn lithospheres will be briefly emphasized in this chapter.

In chapter 6 conculuding remarks of this research will be presented.

2. REGION OF INTEREST: WESTERN TURKEY AND AEGEAN REGION

2.1. Geology And Tectonic Settings

2.1.1. Tectonics

How continents deform has been debated since the earliest days of the development of the plate tectonic model (McKenzie, 1977; Nyst and Thatcher, 2004). Tectonically generated dynamic topography, active faulting and the wide distribution of seismicity give an insight to active continental deformation taking place over broad regions (Nyst and Thatcher, 2004). End-member models have been proposed for this deformation in two different ways: the continental lithosphere deforms as a set of rigid or elastic blocks separated by major strike-slip faults (Tapponnier et al., 1982) or the continental deformation is quasicontinuous (England and McKenzie, 1982).

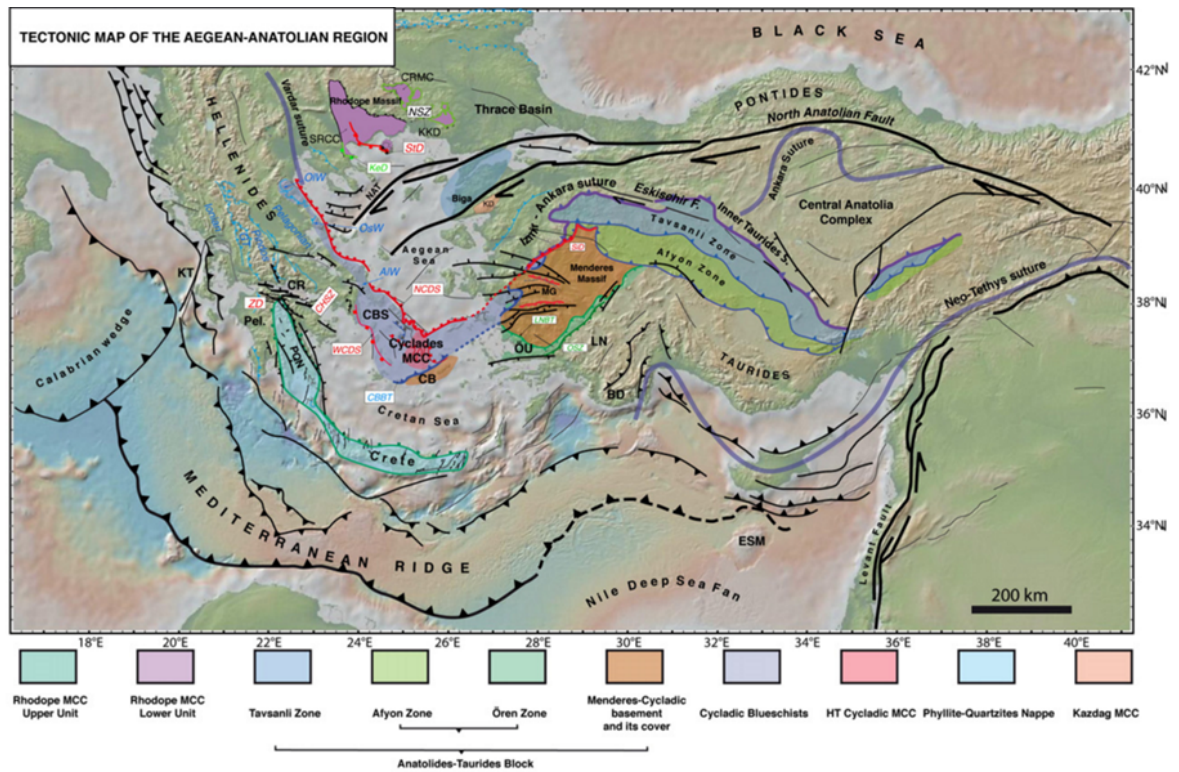


Figure 2.1. Tectonic map of the Aegean and Anatolian region showing the main active structures (black lines), the main sutures zones (thick violet or blue lines), the main thrusts in the Hellenides where they have not been reworked by later extension (thin blue lines), the North Cycladic Detachment (NCDS, in red) and its extension in the Simav Detachment (SD), the main metamorphic units and their contacts; AIW: Almyropotamos window; BD: Bey Daglari; CB: Cycladic Basement; CBBT: Cycladic Basement basal thrust; CBS: Cycladic Blueschists; CHSZ: Central Hellenic Shear Zone; CR: Corinth Rift; CRMC: Central Rhodope Metamorphic Complex; GT: Gavrovo–Tripolitza Nappe; KD: Kazdag dome; KeD: Kerdylion Detachment; KKD: Kesebir–Kardamos dome; KT: Kephalaria Transform Fault; LN: Lycian Nappes; LNBT: Lycian Nappes Basal Thrust; MCC: Metamorphic Core Complex; MG: Menderes Grabens; NAT: North Aegean Trough; NCDS: North Cycladic Detachment System; NSZ: Nestos Shear Zone; OIW: Olympos Window; OsW: Ossa Window; OSZ: Ören Shear Zone; Pel.: Peloponnese; ÖU: Ören Unit; PQN: Phyllite–Quartzite Nappe; SiD: Simav Detachment; SRCC: South Rhodope Core Complex; StD: Strymon Detachment; WCDS: West Cycladic Detachment System; ZD: Zaroukla Detachment (Jolivet et al., 2013).

Tectonically Turkey lies within the Alpine-Himalayan orogenic zone. Present-day tectonic regime of Turkey is ruled by tectonic interactions of African, Eurasian and Arabian plates and ongoing internal deformation along their boundaries (Figure 2.1). These interactions impose a large assortment of tectonic processes such as collision, subduction, back-arc extension, strike-slip faulting. The collision of the Arabian and the Eurasian plates along a localized collision front across the Bitlis-Zagros suture zone since middle Miocene (McKenzie, 1978) and the subduction of African plate beneath the Aegean-Anatolian domain along Hellenic and Cyprian arcs since the late Cretaceous (Westaway, 1994), play an essential role in understanding the major tectonic features in the region. Two different regimes; compressional regime in eastern Anatolia and the extensional regime in the Aegean Sea region is connected by the northern boundary of the westward moving Anatolian block: The North Anatolian Fault (NAF) (Barka, 1992; McKenzie, 1972; Şengör, 1979). Crustal extension and the volcanism in the overlying Aegean extensional province is governed by northward subduction of the African plate beneath western Turkey and the Aegean region. While Eastern Turkey has been experiencing crustal shortening and thickening because of northward motion of the Arabian plate relative to Eurasia and the attendant postcollisional magmatism (Taymaz et al. 1990, 1991a, b; McClusky et al. 2000, 2003; Dilek & Pavlides 2006).

Global Positioning system measurements (Figure 2.2) indicate differential plate motions of Africa ($< 10\text{mm/year}$) and Arabia ($< 18\text{mm/year}$) in a Eurasia fixed reference frame (Reillinger et al., 1997, 2006, 2010). This velocity difference causes major strike-slip faulting along Dead Sea Transform Fault Zone (DSTFZ) leading to westward extrusion of Anatolian plate where its movement is partitioned along North Anatolian Fault Zone (NAFZ) to the north and East Anatolian Fault Zone (EAFZ) to the south (Reillinger et al., 1996) (Figure 2). The right-lateral NAF extends for about 1200 km from eastern Turkey to Aegean Sea in an arc parallel to the Black Sea coast controls the tectonic escape of the Anatolian plate (Barka and Kadinski-Cade, 1988). The general trend of total displacement along the main part of the NAFZ decreases from 40 ± 5 km in the east to 25 ± 5 km in the west (Barka and Gülen, 1988) due to the influence of north-south (N-S) continental lithospheric extension in the Aegean and Western Turkey (Oral et al., 1993).

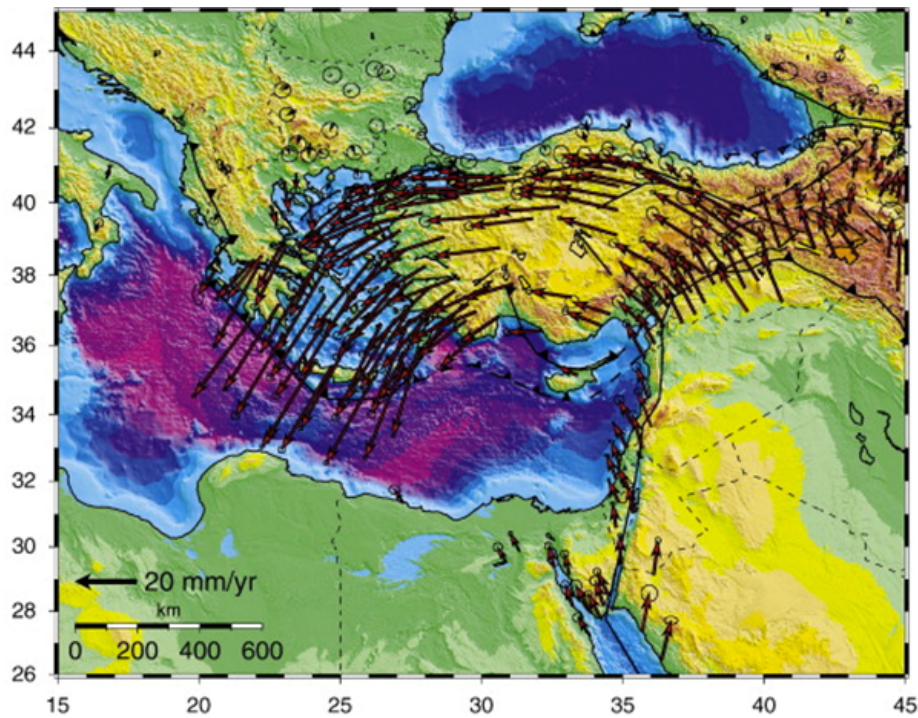


Figure 2.2 GPS-derived velocities with respect to Eurasia (velocity field has been decimated for clarity). GPS velocity uncertainties are 95% confidence ellipses. (Reilinger et al., 2006).

Aegean and East Mediterranean region is characterized by subduction tectonics and is in the initial stages of collision driven orogenic buildup (Dilek, 1996). The ongoing subduction of African plate beneath Eurasia since the late Cretaceous, has been occurring along Hellenic and Cyprian arcs (Hinsbergen et al., 2005). The Hellenic arc is characterized by relatively steep retreating subduction according to slab rollback when compared with Cyprian arc that seems to involve a shallow subduction (Jolivet and Facenna 2000, Facenna et al., 2003). The overall GPS velocity field of the Anatolian–Aegean block relative to Eurasia speeds up towards the Hellenic trench with $\sim 40\text{mm/yr}$ and decreases to 10mm/yr across the Cyprus Arc (Reilinger et al. 1997, 2006, McClusky et al., 2000, 2003).

The segmentation of the Hellenic and Cyprus arcs further compartmentalize the tectonics on the Anatolia (Barka and Reilinger, 1997). The Isparta Angle, a wedge shaped geometry bounded by NW-SE trending Sultandağ thrust fault on the east and the transtensional left-lateral NE-SW trending Fethiye Burdur fault zone on the west (Yağmurlu et al., 1997; Price and Scot 1994), constitutes the junction between the Cyprus and Hellenic

arcs. Subduction along the Hellenic arc has been clearly mapped by relatively higher seismic velocities in various studies with a 1500 km single slab. The long-lived Hellenic subduction is more matured and the slab is probably partly anchored in the lower mantle (Jolivet and Brun, 2010). In the Western Cyprus and Hellenic arcs, the distribution of earthquake hypocenters outlines a Wadati–Benioff zone reaching depths of 110 and 180km, respectively while there is no indication of a Benioff zone in the eastern Cyprus arc. The Cyprus arc has a much lower seismicity rate than the Hellenic arc. This is consistent with the convergence rate across the Hellenic Arc (~35 mm/yr) being about three times faster than across the Cyprean Arc (Reilinger et al. 2006). Tearing of the subducting and retreating African lithosphere at the eastern end of the Hellenic trench has been proposed in a number of publications based on geological and geophysical arguments (Barka & Reilinger, 1997; de Boorder et al.1998; Govers & Wortel 2005; Biryol et al. 2011; Özbakır et al. 2013, 2017). There are different hypotheses about the role of subducting processes on the surface deformation. Jolivet and Facenna indicated that subduction rollback along Hellenic trench is resulted in upper plate N-S extension in western Anatolia (Jolivet and Facenna 2000; Facenna et al., 2003,2013), while Meijer and Wortel (1997) and Özbakır (2017) propose a combined effect of the Arabian push and Hellenic trench pull as main driving boundary conditions for this deformation zone.

Central Anatolia is the westernmost part of the Iranian-Anatolian high plateau at an average elevation of 1.5-2 km. It is located in-between the strongly stretched Western Anatolia and the collisional belt of Eastern Anatolia (Figure 2.1). Its transitional character is attested by undisturbed Miocene sediments observed at an elevation > 1000 km (Cosentino et al., 2012). The present-day internal deformation in CA appears to be significantly less than in WA and EA as evidenced from seismic activity. The uplift of the central Anatolian plateau is recent (8 Ma; Schildgen et al., 2014) and assumed to be related to delamination and slab break-off on its propagation from EA.

The tectonics of western Turkey were shaped by the convergence between the Sakarya continent in the north and Africa in the south, with the Anatolide–Tauride Block (ATB) between two strands of the Neotethyan Ocean (Hinsbergen et al., 2010). The collision started at least ~95–90 Myr ago and continued until 35 Ma when the African slab under western Turkey is decoupled from the African Plate. Slab break-off in western Turkey probably

occurred ~15 Myr ago. The region is characterized by a N-S lithospheric extensional process. The origin and age of the extension in the Aegean have been subjects of discussion for many years. According to Jolivet et al., 2013 the Aegean extension started in Eocene with the formation of Rhodope Metamorphic Core Complexes, and it is widespread to the Cyclades and the northern Menderes Massif in Oligocene and Miocene. When the North Anatolian fault penetrated the Aegean Sea after Messinian times, extension has been localized only in Western Turkey such as late Eocene to present crustal deformation in the Aegean backarc has localized progressively during slab retreat. Several models have been proposed for the extension in the region; 1) slab retreat along the Aegean subduction zone and resulting back-arc extension 2) collapse of an overthickened crust following the latest Paleocene collision across Neotethys along the Izmir-Ankara-Erzincan suture zone during the late Oligocene-early Miocene 3) tectonic escape model along the plate boundaries (Nyst and Tatcher, 2004; Hinsbergen et al, 2010; Jolivet et al., 2013; Facenna et al., 2013; Pourteau et al., 2016). The continental extension is mainly characterized by the exhumation of metamorphic core complexes, where high-grade metamorphic rocks originating in the middle to lower crust are exposed at the surface, and late stretching of crust and a consequent graben formation along Plio-Quaternary high-angle normal faults. The east-west grabens and related normal faults are the most prominent neotectonic features in the region. There are about ten approximately east-west oriented grabens, which are restricted by east-west, subparallel, normal faults, in western Anatolia. The most destructive earthquakes having normal mechanisms striking E-W that fit well with N-S extensional tectonics occurred within the 100-150km long and 10-15km wide Büyük Menderes and Gediz grabens (Eyidoğan & Jackson, 1981). The analysis of GPS observations indicates 140 nstrain/yr across major grabens and 50 nstrain/yr throughout the western Turkey (Aktug, 2009).

2.1.2. Local Geology

The western Anatolia profile (WAP) and central Anatolia profile (CAP) crosscuts several continental fragments, different morphotectonic units that were accreted by the Early Cenozoic closure of the Tethys Ocean and consequent continent-continent collisions (Okay and Tüysüz, 1999). From north to south, Thrace basin (ThB), İstanbul zone (IZ), Sakarya zone (SZ), Bornova Flysch zone (BFZ), Tavşanlı zone (TZ), Menderes Massif (MM), Afyon zone (AZ), Lycian nappes (LN) and Anatolide-Tauride Block (ATB).

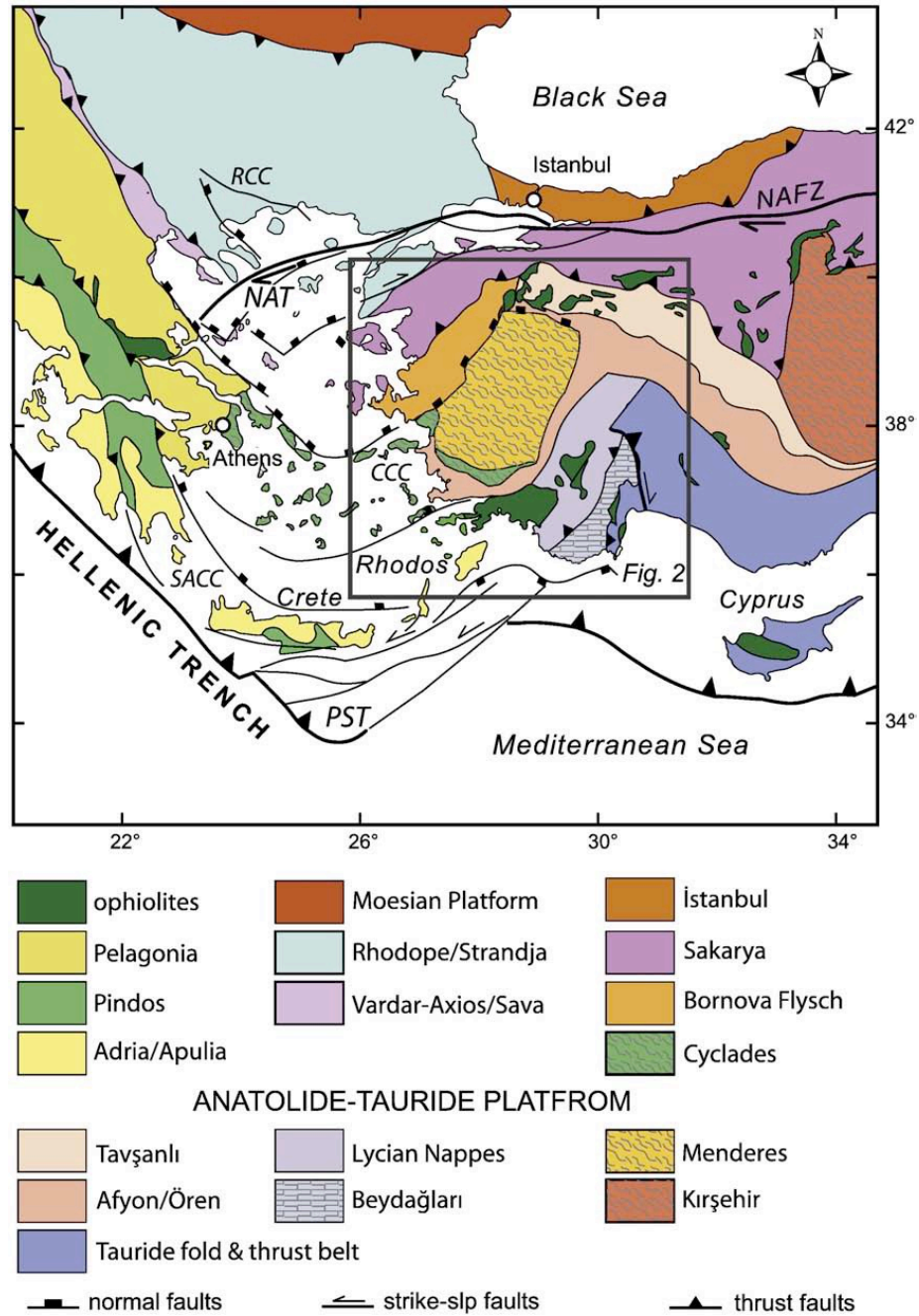


Figure 2.3. Major terranes in the Aegean and Anatolian regions, modified after Moix et al. (2008). Afyon/mln/dn=Afyon zone, Ören Unit and Dilek Nappe; NAFZ=North Anatolian Fault Zone; NAT = North Aegean Trough; PST = Pliny & Strabo Trenches (South Aegean left-lateral strike-slip system) (Hinsbergen et al., 2010).

Eocene-Oligocene aged, triangular shaped Thrace basin (ThB) is located in the northwest Turkey (Figure 2.3). It is a clastic basin on the complex junction between the Strandja, Rhodope, Sakarya and Istanbul terranes (Okay, 2008; Görür & Okay 1996). The sedimentary rocks exceed up to 8 km at the center of the basin, which are composed of sandstone and shale (Okay, 2008; Görür & Okay 1996). The sedimentary sequence begins with Eocene marine turbidites and ends with sandstone, shale and lignite of Oligocene. (Okay, 2008).

On the southwestern margin of the Black Sea; 400 km long and 55 km wide continental fragment is called the İstanbul zone (IZ) (Figure 2.3). It is mainly composed of gneiss, amphibolite, metavolcanic rocks, metaophiolite and voluminous Late Precambrian granitoids based on a late Precambrian crystalline basement (Okay, 2008). The İstanbul zone is characterized by a well developed, unmetamorphosed and little deformed continuous Paleozoic sedimentary succession extending from Ordovician to the carboniferous overlain with a major unconformity by latest Permian to lower most Triassic continental red beds (Hoşgören, 1997). The stratigraphy of IZ is very different from adjacent units. IZ also differs from the neighboring tectonic units by the lack of major deformation. In addition IZ has not experienced metamorphism during major geological times. The Intra-Pontide suture of Late Triassic-Early Jurassic age separates İstanbul and Sakarya zones. İstanbul zone has a Paleozoic basement (Hoşgören, 1997).

The Sakarya zone (SZ) is elongated from the Aegean in the west to the Eastern Pontides in the east (Figure 2.3). On the contrary to the IZ, SZ have a complex Triassic basement instead of Paleozoic basement. This Triassic age basement called the Karakaya complex and it is composed of strongly deformed and low grade metamorphosed basic volcanic rocks, limestones and greywackes with limestone olistoliths (Hoşgören, 1997). The crystalline basement can be roughly divided into three groups. (1) A high-grade Variscan metamorphic sequence of gneiss, amphibolite, marble and scarce metaperidotite; (2) Palaeozoic granitoids with Devonian, Carboniferous or Permian crystallization ages; (3) A low-grade metamorphic complex with minor marble and phyllite dominated by Permo-Triassic metabasite with lesser amounts of marble and phyllite (Okay, 2008 and the references therein). The sedimentary sequence in the terrane starts with Lower Jurassic sandstones (Okay 2008).

The Bornova Flysch zone (BFZ) is a small tectonic zone located between the MM and the İzmir-Ankara suture with dimensions of 50 to 90 km wide and ~230 km long (Figure 2.3). It is characterized by upper Maastrichtian-Lower Palaeocene greywacke and shale with blocks of Mesozoic limestone, mafic volcanic rock, radiolarian chert and serpentinite (Erdoğan 1990; Okay et al. 1996). Mesozoic limestone blocks in the unit are huge exceeding to 10 km or more.

The Tavşanlı zone (TZ) is a relatively narrow (250 km long and 50 km wide) belt located between İzmir-Ankara suture and Afyon zone (Figure 2.3). Subducted and exhumed passive continental margin of the Anatolide-Tauride terrane shows itself as blueschists and ophiolites in the TZ. TZ is composed of oceanic accretionary complexes overlying a coherent stratigraphic sequence of distal continental margin (Okay et al. 1996, Pourteau, A., et al., 2016), distal sediments and volcanic rocks, which underwent a Late Cretaceous subduction metamorphism. The data examined from Blueschists indicates Late Cretaceous high pressure-low temperature (HP/LT) metamorphism is present (Okay, 2008).

The MM is a major metamorphic complex, which are exposures of deep crust exhumed due to magmatic extension, in western Turkey. It is tectonically bounded by the AZ and LN in the south, BFZ and AZ in the north (Figure 2.3). During the geologic times, the MM has been reworked by shallow-dipping detachments and then steeply-dipping normal faults bounding the present grabens (extensional structures) (Hinsbergen et al., 2010 and references therein). Ensuing orogenic collapse and backarc spreading stimulated continental extension and the Early Miocene exhumation of the Menderes metamorphic core complex. It is composed of a gneissic core, rock formed by high-grade metamorphic process from pre-existing formation igneous or sedimentary rock, a schist cover, medium grade metamorphic rock, and a marble, metamorphic carbonate calcite or dolomite (Jolivet et al., 2013). In extensional areas, it is expected to see the horst and graben formations bounded with normal faults. East-west trending Neogene grabens subdivide the Menderes Massif into southern, central and northern submassifs (Okay, 2008). Southern submassif is the best part of the massif to understand the MM sequence due to its simple and well known structure. The others are more complicated and involves large scale overturning and thrusting (Okay, 2008). The terrane experienced different kind of deformation and metamorphism at different

ages. First Eocene nappa stacking and crustal thickening occurred in HP-LT metamorphic conditions near the front of subduction and then crustal thinning in the back-arc region in HT-LP conditions in the Oligocene and Miocene (Jolivet et al., 2013). Generally, MM is characterized by Barrovian type metamorphism (Oberhänsli et al., 2001) and has its own metamorphism type with its name called Main Menderes Metamorphism (MMM) (Jolivet, 2013). The HP-LT MMM has been account for crustal thickening caused by the transport of the Lycian Nappes and Neotethyan ophiolites away from the plate boundary (Okay and Tüysüz, 1999; Sengör et al., 1984; Jolivet et al., 2013).

The Afyon zone (AZ) is located between the MM and TZ. It is characterized by carbonateclastic Palaeozoic series overlain by Mesozoic marbles (Okay, 2008) (Figure 2.3) and blueschist metamorphosed sediments. It has a Tauride stratigraphy. Carpholite and local sodic amphibole shows that area has experienced a high-pressure metamorphism (Oberhänsli et al., 2001). According to stratigraphy, regional metamorphism occurred between latest Cretaceous and Palaeocene (Okay, 2008).

Lycian Nappes (LN) (Figure 2.3) located between AZ and Anatolide-Tauride block and tectonically lies within the flysch sequence. Nappes or thrust sheets are large sheetlike body of rocks that have moved 2-5 km above a thrust fault from its original position. Nappe stacks occur on the continental collision zones and on the overriding plate in active subduction zone. The flysch and the blocks are unconformably overlain by undeformed late Early Eocene (late Cuisian) neritic limestones (Okay, 2008)

Anatolide-Tauride Block (ATB) is on the southern part of Turkey just the opposite of Pontides (Figure 2.3). It was in the footwall position during the obduction, subduction and continental collisions through Late Cretaceous and Palaeocene that is why it has experienced much stronger Alpine deformation and metamorphism than that observed in the Pontic zones (Okay, 2008). Ophiolite and ophiolitic melange occur throughout the A-T including common glacial deposits of Late Ordovician age. Beneath the oceanic thrust sheet Northern part of the zone experienced HP/LT metamorphism at depths of over 70 km (Okay, 2008). Due to different age and type Alpine metamorphism, A-T zone has three metamorphic zones; (1) In the north, a Cretaceous blueschist belt (TZ), (2) at the center lower grade HP metamorphic belt (AZ), in the south Barrovian-type Eocene metamorphic belt (MM) (Okay, 2008).

2.2. Previous Studies

Numerous seismic studies have been extensively performed to image the lithosphere and subduction zones. These include travelttime tomography (Spakman et al. 1993; Koulakov and Sobolev, 2006; Piromallo & Morelli 2003; Biryol et al. 2011), receiver-function analyses (Van Der Meijde et al., 2003; Li et al., 2003; Sodoudi et al., 2006; Zhu et al., 2006; Çakır and Erduran., 2011; Tezel et al., 2013; Karabulut et al., 2013; Vanacora et al., 2013, Kind et al., 2015), surface-wave dispersion (Cambaz and Karabulut, 2010; Hubans, 2010; Bakırcı et al, 2012; Salaun et al., 2012), and seismic anisotropy measurements (Biryol et al. 2009; Paul et al., 2013). The deep lithospheric structure (>100 km) is known from travelttime (Biryol et al. 2011; Spakman et al. 1993; Piromallo & Morelli 2003), surface wave (Pasyanos et al., 2001; Salaun et al., 2011) and Pn (Mutlu and Karabulut, 2011) tomography and gravity studies (Ateş et al., 1999; Tirel et al., 2004). Most of the studies have spatial resolution more than 100 km. Geodetic data measurements (Aktug et al., 2009; Floyd et al., 2010; Le Pichon and Kreemer, 2010; Nyst and Thatcher, 2004; Reilinger et al., 2010, 2006) also performed in the region to determine the motions and deformation rates.

Piromallo and Morelli (2003) performed travel time tomography to discover the upper mantle P wave velocity structure below the Euro-Mediterranean area, down to 1000 km depth. They observed that the subducted slabs at the 660 km discontinuity plays an role in the mantle dynamics of the Aegean and eastern Mediterranean. Moho depth map computed by Hubans (2010) from ambient noise tomography shows a gradual increase of Moho depth from the western Anatolia to the central Anatolia. The teleseismic P-wave tomography by Biryol et al. (2011) displayed fast wave speed anomalies up to 660 km beneath Anatolia that dip steeply. They identified a large gap as wide as 300 km between subducted Aegean and the Cyprus slabs beneath Anatolia. Surface wave tomography of Salaun et al. (2012) represents a spread low-velocity zone between 80 and 200 km depths beneath Anatolia. Evidencing warm asthenosphere underlying a thin mantle lithosphere. According to the existence of dipping high-velocity anomalies at depths larger than or equal to 160 km, velocities are high beneath Anatolia.

Tirel et al. (2004) published a map of the Aegean crustal thickness from the inversion of gravity data. They found mean crustal thickness of 25 km and marked the the Cyclades by a rather flat Moho at 25 km which might be the western counterpart of the Mendere Massif. Moreover, indicated that the Aegean Moho appears to be rather flat with variations of only ± 2 km when compared to the whole region. They proposed two stage extension to explain the Moho depth change. An Oligocene to mid-Miocene generalized gravitational collapse would have thinned the over-thickened crust of the Hellenides to a homogeneous thickness of 25 km in a Basin and Range type spreading of a weak and hot crust. Then, from the Mid-Miocene onwards, the extrusion of Anatolia would have amplified the extension by transtension in the North Aegean trough leading to Moho depths smaller than 24 km, while the retreat of the Hellenic slab would have induced localized stretching in the Cretan Sea to a crustal thickness of 22–23 km, leaving the crust of the Cyclades almost unaffected. Recent crustal thickness studies did not provide high-resolution images due to sparse distribution of stations (Soudoudi et al., 2002; Saunders et al., 1998; Li et al., 2003) until Zhu et al., 2006. Zhu presented the first high-resolution crustal structure image by performing CCP in the central MM in-between the Gediz and Büyük Menderes grabens along a 100km long receiver function profile. They determined comparatively flat Moho at a depth of 26-28 km along the profile but also declared that the size of the profile was insufficient to talk about the geometry of the Moho depth change across the boundaries of the core complex.

Crustal thickness maps for the region have been compiled from sparse data (CRUST2.0, EUcrust, Tesauro et al., 2008), while more regional ones have been computed from higher quality datasets based on receiver functions analysis (Vanacore et al., 2013; Tezel et al., 2013). Çakır and Erduran (2011) fulfilled a study of joint inversion of P wave receiver functions and surface wave dispersion curves. They included S wave receiver function in the inversion procedure to resolve the structures at lithospheric and asthenospheric depths in a small portion in central Anatolia. They found 38 km Moho depth beneath central Anatolia. Tezel et al. (2013) performed a receiver function study with the 120 permanent broadband seismic stations in Turkey to delineate the crustal structure. They used genetic algorithm (GA) to obtain both 1-D S wave model and the Moho depth beneath each seismic station. They found thinner crust in the western Turkey, the Moho depth changes between 24 and 48 km. The thickest Moho observed in the eastern Turkey. The shear wave velocity is 4.0 km/s in the uppermost mantle beneath western Turkey, which is lower than

the global average due to molten or hot upper mantle material. They found 40 km Moho depth beneath Antalya bay where African and Eurasian plates meet. Another noteworthy detailed receiver function study has been implemented in Turkey with 300 stations by Vanacore et al. (2013). They have performed H–K stacking of receiver functions to produce Moho and Vp/Vs ratio maps of the Anatolian Plate. They have found thin crust in the western Turkey less than 30 km with an average Vp/Vs ratio of 1.77. Generally normal Moho depths in the central Anatolia between 37 – 47 km and high Vp/Vs ratios 1.85, which are associated with the recent volcanism. Beneath the LOD station, Moho depth is 38 km Vp/Vs ratio is 1.8.

2.3. Seismicity

The Western Turkey and the Eastern Mediterranean regions are the one of the most seismically active and rapidly deforming areas along the whole Alpine-Himalaya chain. The distribution of seismicity within the Alpine–Himalaya system is not homogeneous, the seismic activity being mostly concentrated along the plate boundaries. The location of earthquake clusters together with active fault systems provide a key role in identifying the boundaries of the assumed microplates. Subduction of African plate beneath the Aegean-Anatolian microplate along the Hellenic and the Cyprian arcs complicates the overall picture. Seismic activity mostly takes place at the brittle crust, earthquake depths are generally within 30 km, except subduction zones, Antalya and Gökova bays where the events occur at intermediate and high depths (>50 km) (Figure 2.4).

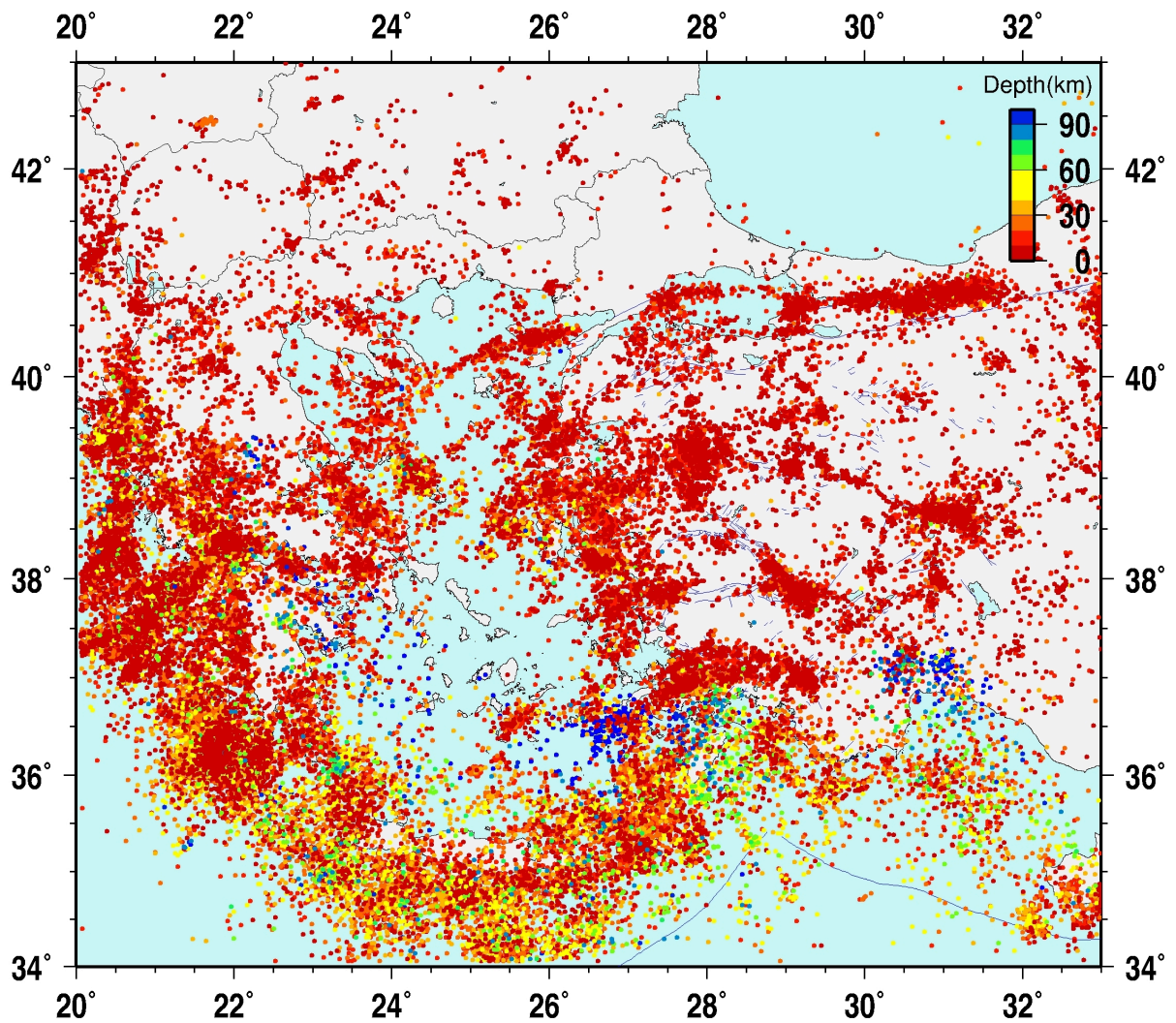


Figure 2.4. Seismicity of the eastern Mediterranean region for the period of 1975-2018, earthquakes with magnitudes greater than 4.0 (EMSC Catalog).

Earthquakes with magnitudes greater than 4 occurred between 1975-2018 years are mapped in Figure 2.4. The overall seismicity distribution is highly consistent with the major tectonic features.

Seismicity along the Hellenic arc is typical of subduction zones with deeper events toward the back-arc region (Figure 2.4). Seismicity zone terminates at a depth of about 180 km (Papazachos et al., 2000). Intermediate depth events (depth: 60-150 km) are mainly located in the inner part of the arc and in Antalya Basin along the Aksu Thrust (AT). Shallow events are widespread along the Hellenic Arc, Greece-Turkey mainlands and the Aegean Sea (Figure 2.4).

Cyprian Arc is less active in terms of seismicity when compared to Hellenic arc (Engdhal 1998; Wdowinski et al., 2006); majority of the earthquakes are located below Anaximander Mountains as well as below the Florence Rise (Figure 2.4). There are no indications for a Benioff zone in the eastern Cyprus arc that forms the plate boundary between the Anatolian plate in the north and the Sinai plate in the south (Wdowinski et al., 2006).

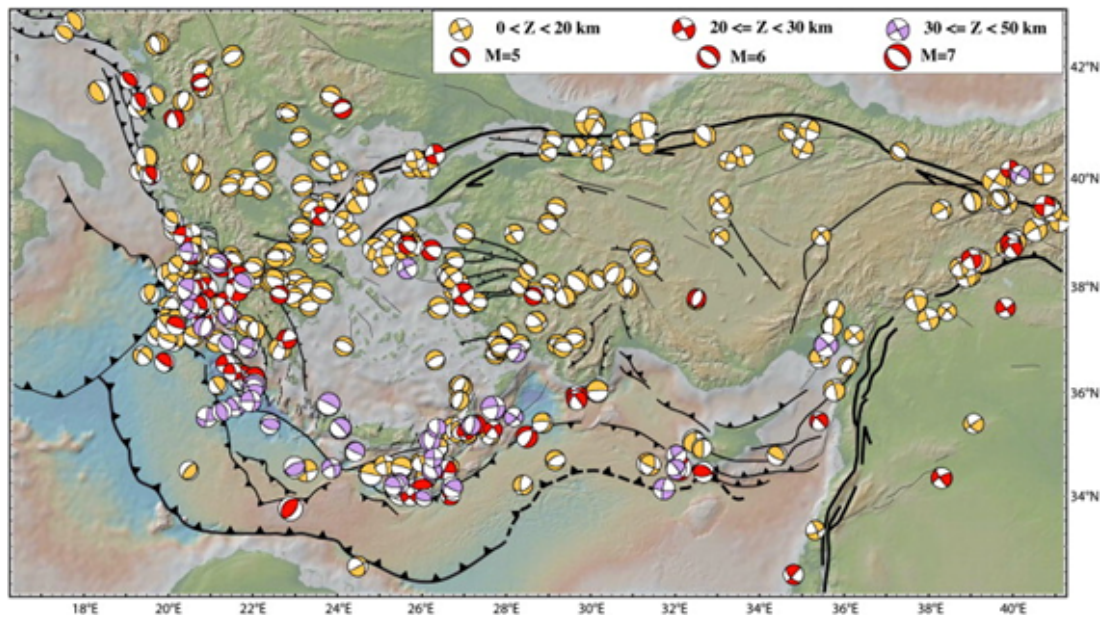


Figure 2.5. Focal mechanisms of earthquakes over the Aegean Anatolian region (Joviet et al., 2013).

The moment tensor solutions of earthquakes with magnitudes greater than 5.0 between 1955 and 2000 in the region presented in Figure 2.5 (Jolivet et al., 2013). Strike slip mechanisms observed along NAF, EAF, North Aegean Trough and south of North Aegean Trough (Taymaz et al., 1991; Roumelioti et al., 2011). As an outcome of extension tectonics, mostly Normal faulting is observed on Western Anatolia, Eastern and Northern Greece and Northern part of the Aegean Trench. In addition, reverse faulting is observed on Aegean Trench and Western Greece.

N-S extension and E-W shortening in western Turkey leads to a several horsts and grabens bounded by oblique E-W trending normal faults system which are getting along with

the focal plane solutions (Figure 2.5). Some of the destructive earthquakes show dominantly normal faulting such as 1969 Alasehir ($M = 6.9$), Gediz ($M = 7.3$) events.

The Marmara region is a tectonically active transition zone between the dextral strike-slip regime of the North Anatolian Fault and the extension regime of the Aegean Sea. The North Anatolian Fault Zone has been subjected to repeated moderate and strong earthquakes like 1999 İzmit ($M_w=7.4$) and Düzce ($M_w=7.2$) earthquakes.

3. METHODOLOGY

3.1. Receiver Function

Teleseismic receiver functions (RFs) have been introduced about three decades ago (Langston, 1977a; 1977b), for the last fifteen years it has become an accepted standard for imaging the lithospheric structure of earth underneath the station by using the information from teleseismic earthquakes recorded at a three component seismograph (Langston, 1979; Owens et al., 1984; Ammon, 1990,1991).

In 1977, Langston and Burdick noticed strong anomalous particle motions on the teleseismic long period P wave records, which were the conversions caused by the velocity discontinuities beneath the receiver. They computed synthetic seismograms for different crustal models to obtain the best fit with the observed waveforms. In 1991, an inverse modeling was introduced by Charles J. Ammon to model the shear wave converted phases and multiples. He used spectral deconvolution with a simple addition to Langston's equalization technique. In 1999, Ligorría and Ammon described and applied an "iterative time domain deconvolution" approach to RF estimation. This technique offers some advantages such as long period stability, multiwaveform deconvolution and high signal to noise ratios. Today this method is most widely used technique for estimating the RFs. In 2000, Lupei Zhu and Hiroo Kanamori posed a straightforward H-k domain stacking which is a very good point measurement under stations. The method is not sensitive to crustal V_p but sensitive to V_p/V_s ratios. Lupei Zhu modified CMP stacking method in 2000 and developed the RF CCP stacking technique and obtained high resolution of crustal images especially along the profiles.

RF techniques are viewed as the primary source of detailed information on the S -wave velocity contrasts within the upper mantle (Morozov and Dueker, 2003). Rotation of 3-component recordings of distant earthquakes into local Z-R-T ray based coordinate system isolates the P to S converted phases on the radial component. The final radial receiver function contains, in addition to the primary converted phases, multiple phases such as P_s , P_sPms (named P_sPs when the interface is Moho), P_pSms (P_pSs) and P_pPms (P_pPs) (Figure

3.1) generated by reflections between the earth's surface and major velocity discontinuities. The time delay between converted S and direct P wave is proportional to the depth of converting interface and the average velocity structure above it.

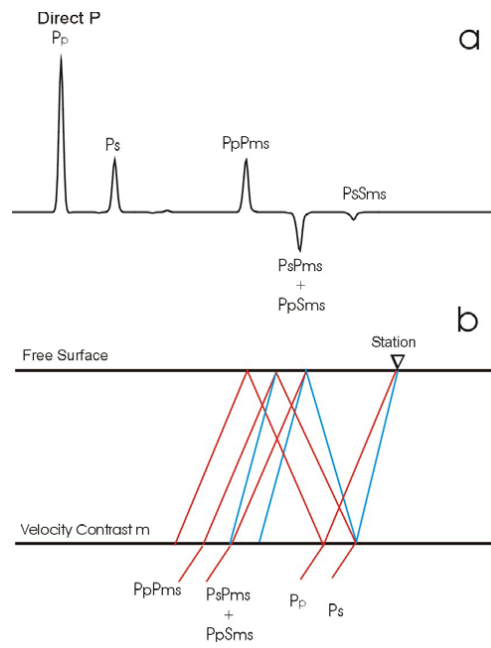


Figure 3.1. The amplitudes and the arrival times of converted phases and multiples depend on the Pwave incidence angle, depth of the velocity contrast m (Cassidy, 1992). (a) The conversions (P_s) and multiples (P_sP_m (P_pP_s), P_pS_m (P_pS_s), and P_pP_m (P_pP_s)) on the RF and (b) the corresponding ray paths (Zor, 2002).

Receiver function estimation has four main steps; data selection; windowing; rotating the seismogram and the deconvolution. The signal at the seismograms are the convolution of seismic source function, impulse response of the recording instrument and the impulse response of the earth structure (Figure 3.2).

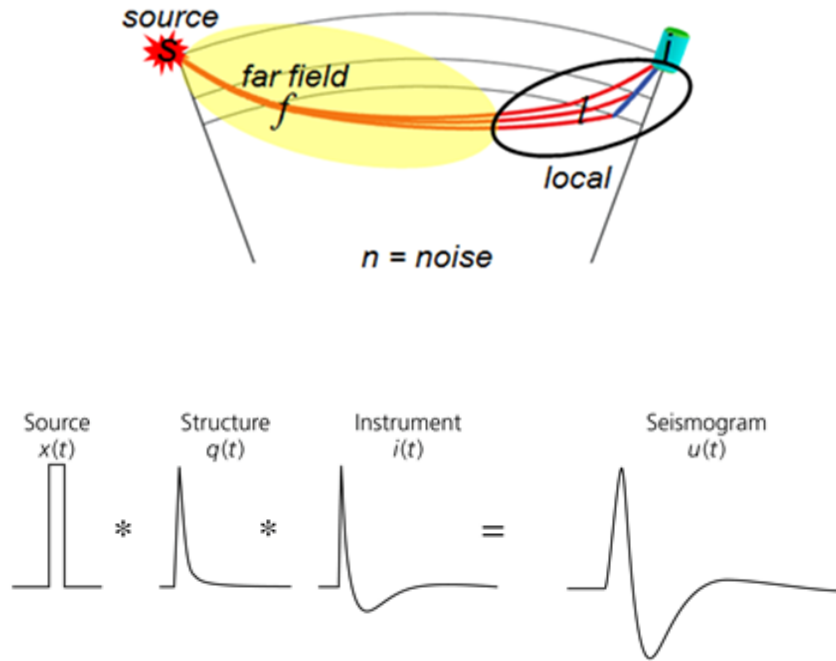


Figure 3.2. Schematic expression of a teleseismic event in the layered earth (Top). Displacement response as the convolution of source, structure and instrument (Bottom).

Theoretical displacement response for a P wave at the station can be represented by,

$$\begin{aligned}
 D_V(t) &= I(t) * S(t) * E_V(t) \\
 D_R(t) &= I(t) * S(t) * E_R(t) \\
 D_T(t) &= I(t) * S(t) * E_T(t)
 \end{aligned} \tag{3.1}$$

Where subscripts V , R and T represent vertical, radial and transverse components. $I(t)$ is instrument impulse response; $S(t)$ is seismic source function and $E(t)$ is the impulse response of the earth structure. Therefore calculating the RF is a deconvolution problem. There are various types of deconvolution techniques but the most prominent ones are frequency domain deconvolution with water level and iterative time domain deconvolution.

3.1.1. Frequency Domain RF Estimation

The vertical, radial and transversal displacements are given by equation (3.1). The theoretical calculations can be simple or complex due to epicentral distances. At distances

30° and 90°, steeply incident P wave consists of a large direct arrival, thus the vertical component behaves as a pulse (Owens et. al., 1984). In 1979 Langston made an assumption in source equalization scheme that

$$E_V(t) \approx \delta(t) \quad (3.2)$$

where $\delta(t)$ is the Dirac delta function. This assumption have some errors but they are tolerable when compared with the advantages it provides. From (3.1) and (3.2) we can write

$$D_V(t) \approx I(t) * S(t) \quad (3.3)$$

$D_V(t)$ contains earthquake source and path effects that we wish to remove from the observed seismograms. By deconvolving the vertical component from the radial component we get

$$E_r(w) = \frac{D_r(w)}{D_v(w)} \quad (3.4)$$

In order to make the denominator real we multiply the denominator and the right hand side of the equation (3.4) with the complex conjugate of $D_v(w)$, $\overline{D_v(w)}$

$$E_r(w) = \frac{D_r(w) \cdot \overline{D_v(w)}}{D_v(w) \cdot \overline{D_v(w)}} \quad (3.5)$$

We can write the tangential RF in the same way just substituting the $D_r(w)$ with $D_T(w)$. Equation (3.5) is valid for the whole frequency band in order to limit the final frequency band we multiply the right side with a low pass Gaussian filter $G(w)$. The Gaussian filter was chosen due to its zero phase distortion, lack of side-lobes and symmetric shape (Langston, 1979).

$$E_r(w) = \left[\frac{D_r(w) \cdot \overline{D_v(w)}}{D_v(w) \cdot \overline{D_v(w)}} \right] \cdot G(w) \quad (3.6)$$

$$G(w) = e^{-w^2/4\alpha^2} \quad (3.7)$$

Where α is responsible for the width of the Gaussian filter used to remove the high frequency noise (Zor, 2002 PhD). In equation (3.6), the small or zero values of the denominator can cause singularities (Langston, 1979) and this will end up with numerically unstable results. In 1971, Helmberger and Wiggins proposed a technique to eliminate the instability by changing the denominator with the $\varphi(w)$ given in equation (3.8).

$$\varphi(w) = \max\{D_r(w) \cdot \overline{D_v(w)}, c \max[D_r(w) \cdot \overline{D_v(w)}]\} \quad (3.8)$$

In equation (3.8) c is the minimum allowable spectral amplitude of the vertical component, the water level, expressed as the maximum spectral amplitude (Owens et. al., 1984). The small amplitude on the vertical component is a result of an attenuation of spectral energy at frequencies caused by replacing small values with larger ones in the denominator (Ammon, 1991). RF is finally defines by

$$E_r(w) = \left[\frac{D_r(w) \cdot \overline{D_v(w)}}{\varphi(w)} \right] \cdot G(w) \quad (3.9)$$

3.1.2. Iterative Time Domain RF Estimation

Frequency domain RF estimation has a problem with small and noisy events, sometimes it might give false bumps in RF which are not a result of velocity contrasts; this will create insufficient and noisy RFs. If the signal to noise ratios are small, another deconvolution technique called iterative time domain deconvolution can be used to calculate RFs. The iterative technique was successfully used in earthquake time function studies in 1980s. Kikuchi and Kanamori in 1982 used the technique to estimate the source time function of the large earthquakes. In 1999, Ligorria and Ammon applied the technique to estimate the RFs. The technique offers some advantages in RF estimation like; first the largest RF arrivals come into prominence and then the details on the seismogram, long period stability as a result of the deconvolution of the sum of Gaussian pulses and gives a chance to deconvolve multiwaveforms for a single RF estimate (Ligorria and Ammon, 1999).

The purpose of the method is to minimize the difference between the observed horizontal seismogram and the predicted signal generated by the convolution of an iteratively updated spike train with the vertical component seismogram (Ligorria and Ammon, 1999). To generate the spike train, the lag of the spikes and amplitudes should be iteratively updated. The source time function is expressed by the superposition of ramp functions in equation (10) (Kikuchi and Kinamori, 1982).

$$S(t) = \sum_i m_i s(t - t_i) \quad (3.10)$$

Where $s(t)$ is the unit ramp function, m_i is the amplitude t_i is the onset time of the i^{th} ramp function. First consider a single wavelet and find m_1 and t_1 by minimizing the error defined by

$$\Delta_1 = \int_0^{\infty} [x(t) - m_1 s(t - t_1)]^2 dt \quad (3.11)$$

Where $x(t)$ is the observed signal and $s(t)$ is the synthetic waveform (source time function). Then apply the procedure to second wavelet and find m_2 and t_2 and so on. The above procedure is iterated until no more significant decrease in the error occurs (Kikuchi and Kinamori, 1982). After N iterations, the largest m_i 's and corresponding t_i 's are determined, by using equation (3.10) source time functions (synthetic waveforms) are calculated and the approximation error can be obtained by,

$$\Delta_N = \int_0^{\infty} [x(t) - S(t)]^2 dt \quad (3.12)$$

Δ_N can be written in terms of correlation functions,

$$\Delta_N = r_x(0) - r_s(0) \left[\sum_{i=1}^N m_i^2 \right] \quad (3.13)$$

$$m_i = \frac{r_{sx}(t_i)}{r_s(0)} \quad (3.14)$$

In equation (3.13) $r_x(0)$ and $r_s(0)$ are the zero-lag auto correlation of observed and unit ramp function. In equation (3.14) $r_{sx}(t_i)$ is the cross correlation of the observed waveform and unit ramp function at i^{th} onset time t_i .

Ligorria and Ammon applied the same procedure to deconvolve the vertical component from the radial and tangential components in time domain where $s(t)$ is the unit ramp function, $S(t)$ is the source time function and observed waveform $x(t)$ is the vertical component motion, RF and radial component of the function.

3.2. H-K Stacking

In 2000, Zhu and Kanamori proposed a new stacking technique that sums the amplitudes of RF at predicted travel times of the converted phases by different crustal thicknesses H and crustal V_p/V_s ratios K . Without identifying the converted phases and picking their arrival times, time domain RFs transform directly into the H-K domain (Zhu and Kanamori, 2000). There are some main advantages of the algorithm like; large amount of data can be conveniently processed, no need to pick the arrival times of the converted phases, lateral structure effects are suppressed by stacking RFs from different distances and directions and average crustal model is obtained. The method provides a good point measurement.

A different modified form of frequency domain deconvolution is used by dividing the spectrum $R(w)$ of teleseismic P waveform by the source spectrum equation (3.15);

$$r(t) = (1 + c) \int \frac{R(w) \overline{S}(w)}{|S(w)|^2 + c\sigma_0^2} e^{-\frac{w^2}{4\alpha^2}} e^{iwt} dw \quad (3.15)$$

Where $\overline{S}(w)$ is the complex conjugate of $S(w)$. Water level $c\sigma_0^2$ is used to suppress the holes in the spectrum $S(w)$ to stabilize the deconvolution, auto correlation σ_0^2 of $S(t)$ is used to normalize the water level so that c can be selected for a narrow range for different

size earthquakes. Gaussian type low pass filter is added to remove the high frequency noise, $(1 + c)$ factor is used to compensate the amplitude loss due to the water level (Zhu and Kanamori, 2000).

On the radial receiver function, the prominent signal following the direct P wave is the P_s wave converted from Moho discontinuity. The crustal thickness H beneath the station can be calculated from the arrival time difference t_{ps} between P_s and P . The thickness estimate is not sensitive to crustal P wave velocity, as much as to the crustal V_p/V_s ratio K due to the differential travel time between S and P waves is used. This tradeoff between the H and K can be reduced significantly by adding multiply converted phases, namely PpP_s and $PpS_s + P_sP_s$ (Zhu, 1993; Zandt et al., 1995; Zhu et al., 2006).

The crustal thickness can be estimated from the time separation between P and P_s given below in equation (3.16),

$$H = \frac{t_{ps}}{\sqrt{\frac{1}{V_s^2} - p^2} - \sqrt{\frac{1}{V_p^2} - p^2}} \quad (3.16)$$

Where p is the ray parameter. The ambiguity can be reduced by using additional multiples, in equation (3.17) H is calculated for PpP_s and in equation (3.18) for $PpS_s + P_sP_s$,

$$H = \frac{t_{PpP_s}}{\sqrt{\frac{1}{V_s^2} - p^2} + \sqrt{\frac{1}{V_p^2} - p^2}} \quad (3.17)$$

$$H = \frac{t_{PpS_s} + t_{P_sP_s}}{2\sqrt{\frac{1}{V_s^2} - p^2}} \quad (3.18)$$

It is not so easy to identify Moho P_s and multiples and measure their travel times on a single RF trace due to background noise, conversions from other velocity discontinuities and scatterings from crustal heterogeneities. To get rid of these, one can use multiple events to

stack in order to increase the signal to noise ratio (SNR). Zhu and Kanamori (2000) proposed a straightforward H - K domain stacking given below in equation (3.19).

$$s(H, K) = w_1 r(t_1) + w_2 r(t_2) + w_3 r(t_3) \quad (3.19)$$

Where $r(t)$ is the radial receiver function, t_1 , t_2 and t_3 are the predicted Ps , $PpPs$ and $PpSs+PsPs$ arrival times corresponding to H and K as given in equations (3.16), (3.17) and (3.18). The w_i 's are the weighting factors of the phases and the sum of them should be equal to one, $\sum w_i = 1$. The values are chosen to balance the contributions of the converted three phases. Ps is the most dominant one with the highest SNR so it is given higher weight than the others. Usually a simple relation $w_1 > w_2 + w_3$ is used because the later two multiples have similar slopes in H - K plane (Zhu and Kanamori, 2000).

We can obtain variances of H and K given in equations (3.20) and (3.21), by expanding it in to Taylor series at the maximum and omitting the high-order terms.

$$\sigma_H^2 = 2\sigma_s / \frac{\partial^2 s}{\partial H^2} \quad (3.20)$$

$$\sigma_K^2 = 2\sigma_s / \frac{\partial^2 s}{\partial K^2} \quad (3.21)$$

Where σ_s is the estimated variance of $s(H, K)$ from stacking.

3.3. Common Conversion Point Stacking

Common Conversion Point (CCP) stacking technique is used to image the crustal structure along the profile. In 1997, Dueker and Sheehan used the idea of common midpoint (CMP) stacking in reflection seismology and developed RF CMP stacking method by geographically binning receiver functions at certain depths according to their piercing points (Zhu, et. al., 2006). A shortcoming of the method is the change in the location of piercing point with depth due to the slope of ray-path. Therefore Zhu (2000) modified the CMP

stacking method and developed CCP stacking technique. While CMP stacking and migration is dealing with reflected waves, CCP is applied to converted waves.

The method consists of two main steps: backprojection and stacking. The aim of backprojection method is to project the data, which is recorded at the station, along the ray path from receiver to source. At the end model parameters of the ray passed medium were obtained by using the relation between ($d = g(m)$) observations (d) and model parameters (m). In backprojection methods, model is designed with constant slowness (velocity) blocks. Therefore, it can be linearized by using the relationship between traveltimes d and slowness perturbations m .

First ray-paths are calculated by using a background velocity model. RFs are corrected for incidence angle effect. An assumption is made: every amplitude on the radial receiver function following the direct P is assumed to be generated by a single P to S conversion along the whole ray-path. Then the amplitude at each point on RF is projected to corresponding location on the ray-path where the P to S conversion occurred, using its delay time with respect to direct P (Zhu, 2000). This amplitude represents the velocity change (impedance change) of the medium at the conversion point. After back projecting the RFs, the volume along the profile is divided into designated size bins. The horizontal dimension of the bin size depends on the wavelength of signals and the vertical dimension is determined by the sampling rate of the receiver function (Zhu, 2000). In order to obtain the average amplitude and variance, all the amplitudes in each bin is summed up in other words to obtain the structural image, all amplitudes in the same bin are stacked. (Figure 3.3).

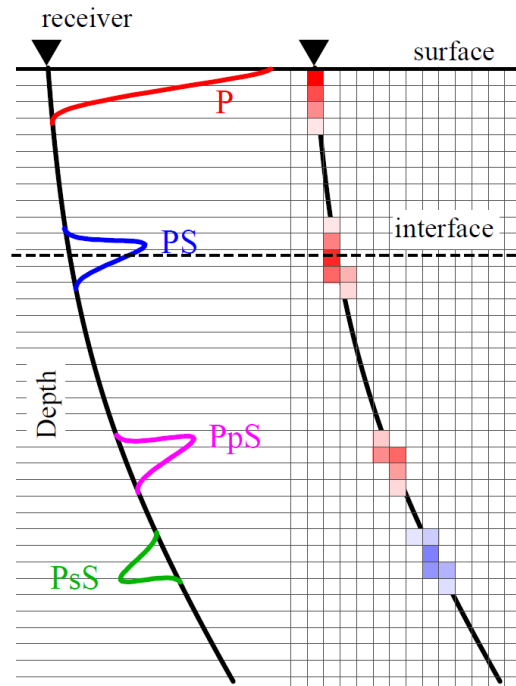


Figure 3.3. Schematic representation of CCP migration. Left, computed RF trace in its theoretical path. Right, its mesh gridded amplitudes (red indicates positive, blue indicates negative) (Hetenyi, 2007 PhD).

Due to the steep incidence angle of the Ps ray-path, technique has the potential to obtain high lateral resolution. The lateral resolution of CCP image is determined by the size of Fresnel zone of the incident P wave, which varies with depth z as $\sqrt{\lambda z}$ (Zhu et al., 2006). The vertical resolution of the image depends on seismic discontinuities being separated by more than $1/4$ of S-wave wavelength (Zhu et al. 2006). The true uncertainties result from V_p/V_s and V_p , for a 3% uncertainty in crustal P wave velocity it is less than 1km and 2 km for a 3% uncertainty in crustal V_p/V_s ratio (Zhu and Kanamori, 2000).

Multiple reflections travel longer paths in the heterogeneous shallow crust and have extra reflections at the surface that's why they tend to be less coherent than the primary conversions. Multiples generated from same interface with different incident angles will be mapped to different depths. To enhance the primary conversions while suppressing the multiples and noise, stacking many receiver functions from different events and receivers should be performed. An array of densely distributed stations and a good azimuthal distribution of earthquakes are necessary to achieve a successful CCP stacking (Zhu, 2002).

3.4. 1-D Inversion

One of the main problems in geophysics is to find the earth structure that satisfies the observed data. The model is fully described by N_{dim} parameters m . Model space contains all possible parameter sets and each point in this space is a valid description of the system. Given a model m and a physical law G , we can predict a set of data values d . In this manner forward problem can be written by equation (3.22)

$$d = G. [m] \quad (3.22)$$

The inverse problem is to find an appropriate model m that corresponds to observed data d , can be expressed as:

$$m = G^{-1}[d] \quad (3.23)$$

However, it is not always possible to find G^{-1} for inverse problems especially when the model parameters and model response have nonlinear functional relation. The way of dealing with nonlinear problems is to try and invoke linearization about a chosen model, and make use of linear inversion techniques. These are often inadequate when the nonlinearity becomes severe and when calculated for a single best data fit model they can produce overly optimistic resolution estimates (Sambridge, 2001). Also it is not always easy and possible to calculate the partial derivatives with respect to model parameters. Therefore derivative free ‘direct search’ algorithms are attractive alternatives.

In the last few decades, by the exponential increase in computer speed, derivative free algorithms based more on exploration than on exploitation have made it possible to solve these problems. The early direct search methods based on uniform pseudo random sampling of a parameter space though they are not user friendly in the existence of high dimension parameter spaces. Monte Carlo methods (Hammersley & Handscomb, 1964) used extensively for probabilistic or randomized searching of a finite dimensional parameter space. The main problem with these early direct search methods was that they were limited by the dimensionality of the parameter space due to computational constraints (Kim, Hyun-

seung., 2007). Moreover, early direct search and linearized methods, had difficulties to determine model parameters uniquely, none or an infinite number of models can satisfy the data. To address this issue, the simulated annealing (SA) method was introduced into geophysics (Kirkpatrick et al., 1983). This stochastic direct search method developed for global optimization problems. After SA, genetic algorithm (GA) was introduced into geophysics (Stoffa and Sen, 1991) from computer science (Holland, 1975), which also seeks a model giving a globally optimal data misfit value within a pre-defined finite dimensional parameter space. For both SA and GA, the basic method needs more applications to determine suitable control parameters to fit the data to a satisfactory level (Gallagher and Sambridge, 1994; Sen and Stoffa, 1995); however, it is not always so easy to determine these parameters. In addition, it is possible to have many local minima, or a very complex data misfit function. It may be inappropriate to optimize the model properties. In such cases, it is not possible to find the optimal model (Kim, Hyun-seung., 2007).

In 1999, Malcom Sambridge proposed a new derivative free search method to do optimization in inverse problems named neighborhood search algorithm (NA). The objective of the method is to sample the region of parameter space that contains models of acceptable data fit or any other objective function, select the most promising regions, and sample these regions more thoroughly in a manner such that the most heavily sampled areas corresponds to the areas where model fits data best and then to extract robust information from the ensemble of models obtained. The algorithm based on assuming the misfit of each of the previous models as a representative of the region of space in its neighborhood (Sambridge, 1999a).

The algorithm uses the geometrical constructs known as Voronoi cells to drive the parameter space. The algorithm only relies on two control parameters, namely the number of new samples per iteration n_s and the number of promising models to select for further inspection, n_r , this is the main advantage of the algorithm. If the ratio n_s/n_r is close to 1 the algorithm will explore the model space, if the ratio is close to 0 the algorithm will behave more exploiting (Sambridge, 1999a). While exploiting algorithm utilizes local information to select better models, exploring algorithm explore the whole space regardless of local areas of interest.

3.4.1. Voronoi Cells

The NA makes use of simple geometrical concepts known as Voronoi diagram that divides the d -dimensional space into n_p regions called Voronoi cells. Each cell is simply the nearest neighbor region about one of the previous samples, as measured by a particular distance measure (Sambridge, 1999a). The distance between models m_a and m_b in L_2 norm is given by equation (3.24),

$$\|(m_a - m_b)\| = \sqrt{((m_a - m_b)^T C_M^{-1} (m_a - m_b))} \quad (3.24)$$

Where C_M is the matrix that non-dimensionalizes the parameter space such a prior model covariance matrix. C_M adjusts the size and shape of the Voronoi cells. By choosing a diagonal matrix with the elements $1/s_i^2$, C_M can be reduced to an identity by rescaling each parameter axis by a set of scale factors, $s_i (i=1 \dots d)$. Then C_M matrix can be reduced.

Set of points in d -space is $P = \{m_1 \dots m_{n_p}\}$, where $2 \leq n_p \leq \infty$, and let $m_i \neq m_j$ for $i \neq j$. The Voronoi cell at each point m_i can be expressed by equation (25),

$$V(m_i) = \{x \mid \|x - m_i\| \leq \|x - m_j\| \text{ for } j \neq i, (i, j = 1, \dots, n_p)\} \quad (3.25)$$

Figure 3.4 indicates a set of irregularly distributed Voronoi cells about 10, 100 and 1000.

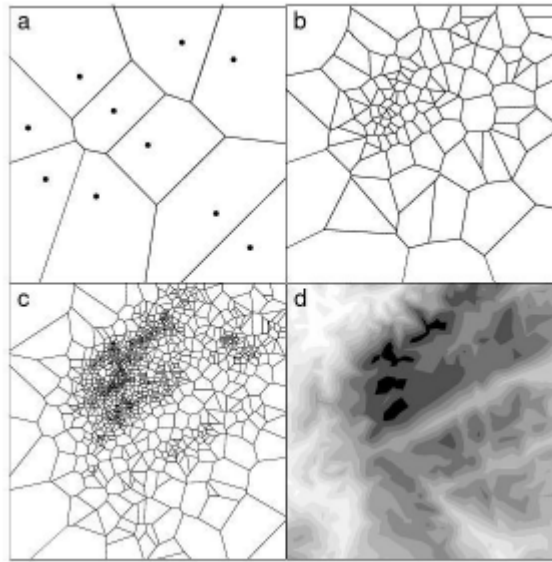


Figure 3.4. (a) 10, (b) 100 and (c) 1000 random points and their Voronoi cells. (d) Contour of the test function. The black areas represent the minima (Sambridge, 1999a).

Since the data misfit function is known at all previous samples, the NA approximation to the misfit surface (NA surface) is generated by setting the misfit to a constant inside each cell. It is required to find the closest previous samples to evaluate the approximate misfit at any new point (Sambridge, 1999).

3.4.2. The Behavior of the Neighborhood Search Algorithm

In figure 3.4 different stages are illustrated. The main idea is to generate new samples by resampling the chosen Voronoi cells with a locally uniform density. We can separate the algorithm into four steps as follows,

1. Constitute an initial set of random models n_s uniformly in the model space.
2. Calculate the misfit for each of the recently generated set of models, n_s and find n_r models with the lowest misfit.
3. Generate n_s new random models by performing a uniform random walk in the Voronoi cell of each of the n_r chosen models. In other words, generate n_s/n_r new random models inside each of the n_r cells.

4. Recycle the process until the desired amount of models generated (go to step two and generate new n_s).

Gibbs sampler is convenient to generate the uniform walk. At each step i th component of the current model, x_A , is replaced with a uniform random perturbation restricted to the boundaries of the current Voronoi cell (Sambridge, 1999).

The misfit of each of the previous models stands for the region of space in its neighborhood (Sambridge, 1999a). Two main advantages of the algorithm are, the size and shape of the neighborhoods are determined automatically and uniquely by the all previous samples, the algorithm uses only the rank of the misfit function instead of misfit function itself. Therefore it only requires models to be assessed for their relative fit to the data.

3.4.3. The Gibbs Sampler

In contrast to other sampling methods, a perturbation to a model is generated and always accepted in Gibbs sampler (for details see German and German, 1984). Figure 3.5 indicates an example of random walk.

Where T_{FM} the computational time of forward modelling, model is is perturbed randomly along one of its d parameter axes, discretization of the axis is n_a . With the NA surface,

$$T_{NA} = T_{FM} + T_{NN}n_ad \quad (3.27)$$

T_{NN} is computational time for nearest neighbor search. This leads to a cost ratio which is given in equation (3.28)

$$\frac{T_{NA}}{T_{misfit}} = \frac{1}{n_ad} + \frac{T_{NN}}{T_{FM}} \quad (3.28)$$

3.4.4. Sampling Voronoi cells using exact intersections

Neighborhood algorithm only requires to find the intersection points of the Voronoi diagrams, instead of determining the full details. i^{th} axis passing through a given point x_A intersects with the boundaries of the d -dimensional Voronoi cell (Sambridge, 1999).

It is essential to calculate the exact intersection point between the Voronoi cell and the nearest neighbor along a given dimension. Define k th Voronoi cell as the one about sample v_k , and the point where the boundary between cell k and j intersects the axis as x_j (Figure 3.5),

$$\|(v_k - x_j)\| = \|(v_j - x_j)\| \quad (3.29)$$

In the i th dimension of the model space equation (3.29) can be expressed as,

$$d_k^2 + (v_{k,i} - x_{j,i})^2 = d_j^2 + (v_{j,i} - x_{j,i})^2 \quad (3.30)$$

By taking $C_M = I$. Where d_k is the perpendicular distance of sample k from current axis, and a subscript of i denotes the i th component of the corresponding vector. This expression can be solved to find the exact intersection point x_{ij} given in equation (3.31).

$$x_{j,i} = \frac{1}{2} \left[v_{k,i} + v_{j,i} + \frac{(d_k^2 - d_j^2)}{(v_{k,i} - v_{j,i})} \right] \quad (3.31)$$

Equation (3.31) has to be calculated for all n_p cells and the two closest points at each side of x_A retained to find the required boundaries of the Voronoi (See Sambridge, 1999a for details). A set of perpendicular distances d_j^2 ($j = 1, \dots, n_p$), calculated for the initial axis and recursively updated for each new axis is required at each step of the random walk. Walk moves from x_A to x_B after the i th step has been completed, the current set of d_j^2 values can be calculated for the $(i+1)$ th axis by using equation (3.32),

$$(d_j^2)_{i+1} = (d_j^2)_i + (v_{j,i} - x_{B,i})^2 - (v_{j,i+1} - x_{B,i+1})^2 \text{ for } (j = 1, \dots, n_p). \quad (3.32)$$

The time spend for each independent sample is then,

$$T_{NA} = T_{FM} + \lambda_2 n_p d \quad (3.33)$$

Where λ_2 a constant of proportionality and n_p is the amount of models in the space at the time (Sambridge 1999a).

3.4.5. Finding acceptable models with NA

Data fit measure $\varphi(m)$, is necessary to find acceptable models by the time the new ensemble is ready. It is L_2 norm of the differences between the observed and predicted seismograms from an Earth model. For a φ_t , representing the tolerance level, an acceptable model is then one for which,

$$\varphi(m) \leq \varphi_t \quad (3.34)$$

If the data misfit is below tolerance level, modify set $\varphi(m)$ to a constant (Sambridge, 2001),

$$\begin{aligned}
\varphi_F(m) &= \varphi(m) \left(\text{if } \varphi(m) > \varphi_t \right) \\
\varphi_F(m) &= \varphi_t \left(\text{if } \varphi(m) \leq \varphi_t \right)
\end{aligned}
\tag{3.35}$$

The definition (3.35) makes the algorithm only ‘sees’ a uniform objective function in all regions of parameter space which are acceptable (Sambridge, 2001). The algorithm behaves exploring on a local level by the misfit definition.

In order to increase the sampling densities near the edges of the model space reversed misfit function, $\varphi_R(m)$ is introduced (Equation (3.36)). Misfit function with very low values near the edge of an interesting area makes the algorithm to sample the edges.

$$\begin{aligned}
\varphi_R(m) &= \varphi(m) \left(\text{if } \varphi(m) > \varphi_t \right) \\
\varphi_R(m) &= \varphi_t - \varphi(m) \left(\text{if } \varphi(m) \leq \varphi_t \right)
\end{aligned}
\tag{3.36}$$

Overall the objective of the NA search algorithm is to extract robust information from the set of obtained models to sample the parameter space that contains models of acceptable data fit (Sambridge, 1999a).

4. DATA ACQUISITION AND PROCESSING

4.1. Data And Earthquake Distribution

In order to provide insights on the complex lithospheric structure beneath Aegean and the surroundings, SIMBAAD project, which was based on the establishment of a dense network of seismic stations on the Aegean and Western Turkey (Figure 4.1) was started on June 2007. The temporary network was deployed for a period of two years in cooperation with the Laboratoire de Géophysique Interne et Tectonophysique (France).

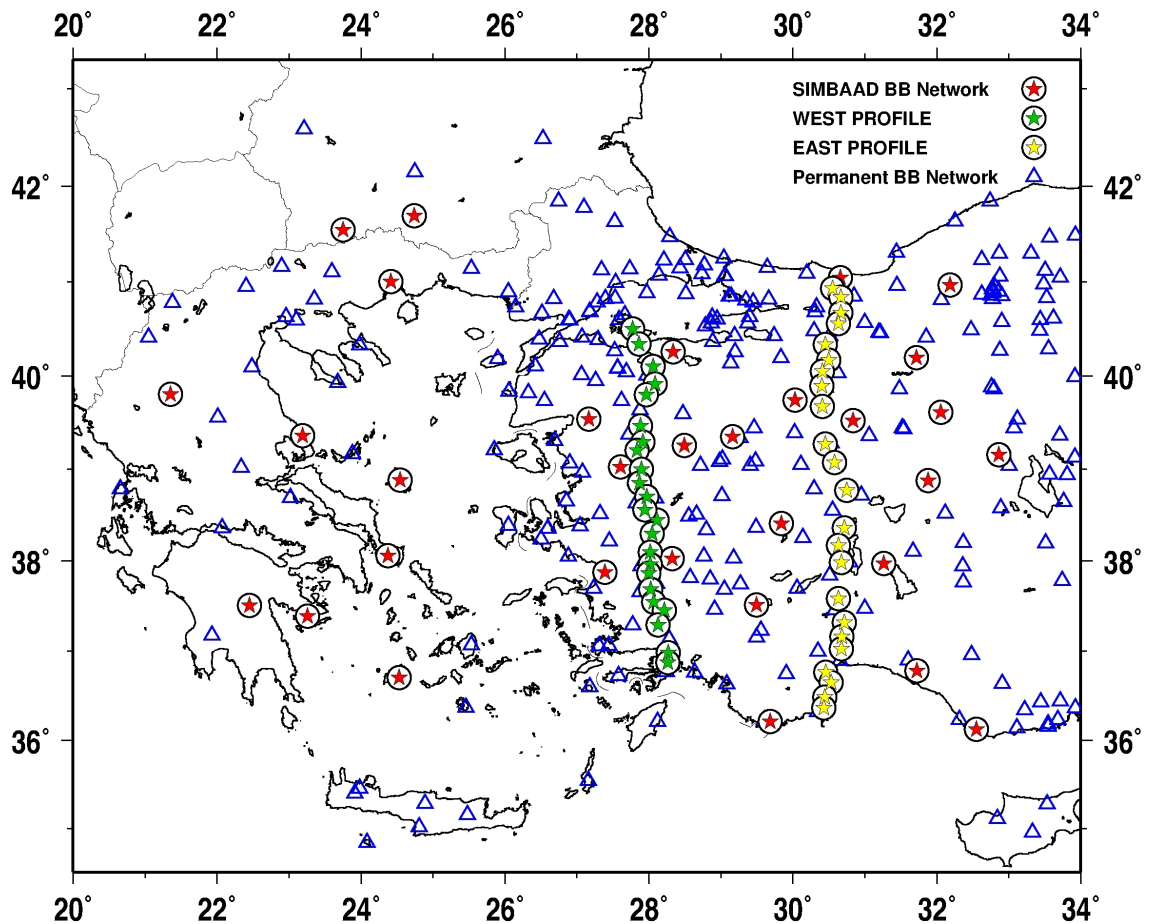


Figure 4.1. Permanent and temporary seismic stations deployed during the 2007–2009 SIMBAAD experiment. Green and yellow stars in the circles are the medium band stations on the profiles, red stars in the circles are the SIMBAAD broadband stations and blue triangles represents the permanent networks.

A total of 33 broadband and 23 medium band seismic stations were installed in Central and Western Turkey, Greece and Southern Bulgaria for a 2 year duration (Figure 4.1) in order to complement the permanent network of Kandilli Observatory and Earthquake Research Institute (KOERI-RETMC) of nearly 90 broadband seismometers, with an average spacing of 100 km (Appendix A, Table 1, 2 and 3). To enhance the density of the seismic stations, permanent network of AFAD, IRIS and temporary network of previous experiment WASRE were involved to the research. The network includes broadband sensors with 90s-120s responses (Streckheisen STS-2 and CMG3-ESP) to record low-frequency surface waves which penetrate at 200-300 km into the mantle while the stations on the profiles contained medium band sensors (CMG40T and Lennartz Le3D-5s). The data were continuously recorded by Agecodagis Minititan digitizers with 50 sample per second.

In order to image velocity discontinuities in the mantle like the boundaries of the subducting slabs or the mantle discontinuities from receiver functions, 2 dense profiles in Western Anatolia and Central Anatolia were installed along the coast of the Aegean sea crossing almost perpendicular to the tectonic strike of east-west trending structures. North-South extending Western Anatolia profile (WAP) centered on 28 °E, 23 temporary stations (sensors CMG40T with natural period of 30 or 60s) deployed in the experiment (green stars in circles in Figure 4.1). The length of the profile increased to 650km by the use of permanent seismic stations at the Rhodes Island in the south and Thrace in the north. The broadband data from previous WARSE experiment (Zhu et al., 2006) and permanent networks increased the number of stations on the profile up to 40 with an average interstation distance of 15 km (see Appendix A, Table 1). After one year of recording the stations on the line were removed and installed along the second profile, ~200km east of the first profile at 30.5 °E longitude. The permanent stations increased the number of stations to 32 on the profile with an average interstation distance of 15 km (yellow stars in dark blue circles in Figure 4.1) (Appendix A, Table 2).

The one year deployment on the WAP leads more than 100 events with magnitudes greater than 5.5. Teleseismic distances selected between 30° and 95° due to the complication on the seismograms by upper mantle travel path effects for distances closer than 30°, and the stations are located within the shadow zone of the direct P-wave for greater than distances further

than $\sim 95^\circ$. The events were visually checked and 60 events with fair signal-to-noise ratio were selected for the analysis. The azimuthal coverage is non-uniform as majority of events comes from the Western Pacific subduction zone and few from Indian and Atlantic Oceans (Figure 4.2) which provided a fairly good azimuthal coverage. The data from the permanent stations on the profile, which are available for longer durations, were also included in the analysis. The WAP removed 200km east and the Central Anatolia profile (CAP) centered at 30.5°E longitude after one year, nearly same amount of events were recorded and analyzed according to the same criteria.

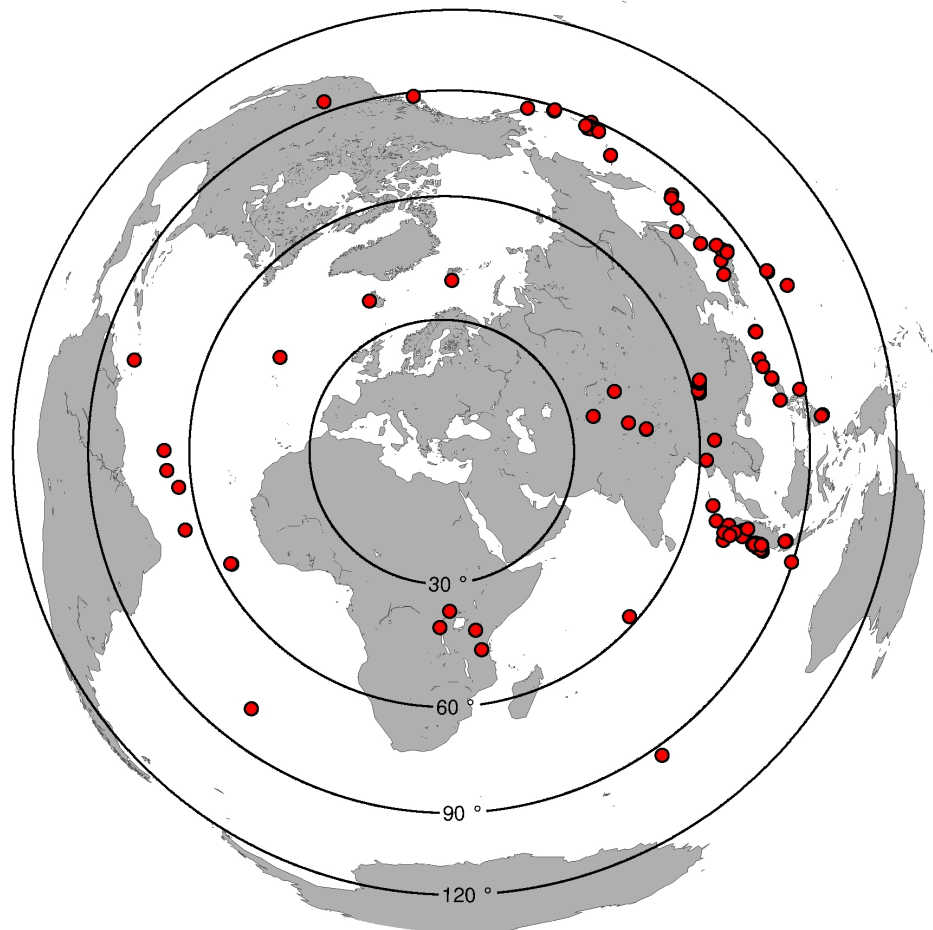


Figure 4.2. Equidistant projection of the locations of teleseismic events used in this study.

The data quality and quantity along the profiles had a large variations. Most of the sites recorded more than 50 events with exceptions of W11 and W20 (Figure 4.1) due to malfunction and low SNR. The noise levels of the stations installed along the profiles depend on the local geology. Lower SNR is observed at sedimentary basins such as GG and MG on

the WAP while SNR is more uniform along the CAP. The 90 permanent stations of KOERI provided data for longer time interval (between 2004 and 2015) therefore we adopted a larger magnitude threshold ($M_w > 6.3$) for a higher SNR. Figure 4.3 represents the waveforms of a teleseismic event occurred in the Pacific subduction zone on 17th July 2008. The record section displays vertical components of the seismograms.

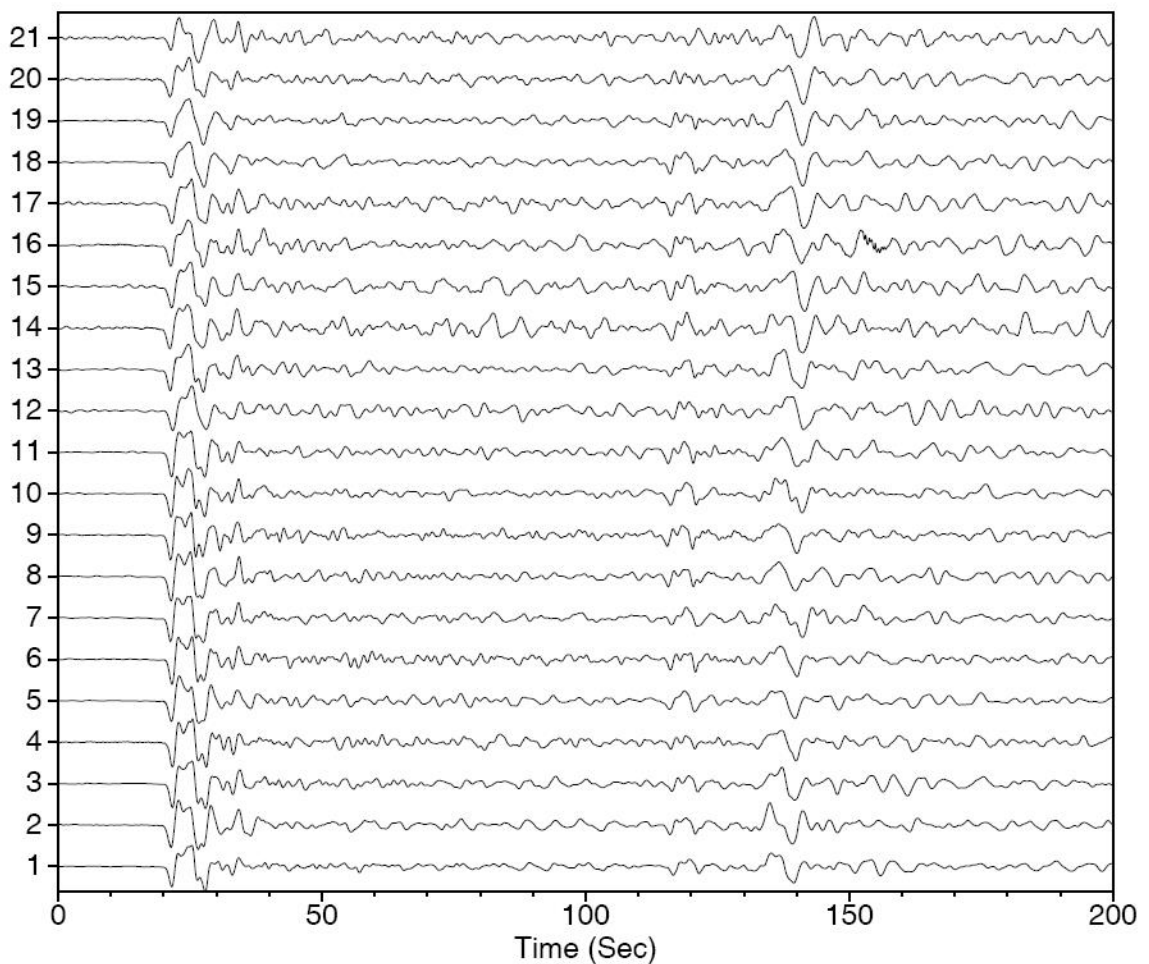


Figure 4.3. Vertical component waveforms of a teleseismic event from Pacific subduction zone at 05:00:00 h on 2008 July 17 (distance 57° , depth 120 km and magnitude $M_w=6.7$).

The waveforms are aligned to the first P-onset time.

4.2. Receiver Function Computation

We computed radial and transverse RFs via time domain iterative deconvolution method of Ligorría & Ammon (1999) (please see chapter 3 for further information). To

compute the RFs the three component data rotated to ray based Z-R-T coordinate system than the data downsampled and decimated to 20 sps (Figure 4.4).

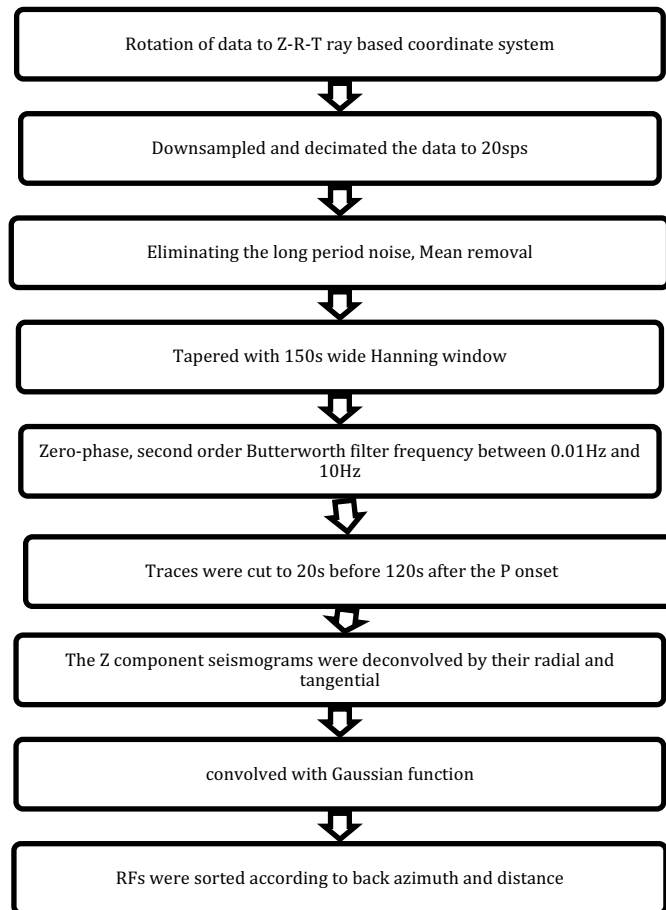


Figure 4.4. Data preparation steps.

The mean of each trace removed and tapered with 150s wide Hanning window. Band-pass filtering applied using zero-phase, second order Butterworth filter with frequency between 0.01Hz and 10Hz. Then the traces cut to 20s before 120s after the P onset. The vertical component seismograms deconvolved by their radial and tangential components. The time series convolved with a Gaussian function for different alpha parameters (2.5, 3.5, 4.5, 5.5, 6.5, and 7.5) equivalent to low-pass filter with cut-off frequencies 0.5, 0.7, 1.0 respectively and 4.5 was chosen for final calculation. Gaussian function has been chosen due to its zero phase distortion, lack of sidelobes and symmetric shape. The RFs were sorted according to back azimuth and distance and visually checked due to noise levels. Radial and transverse RFs with anomalous shapes and amplitudes were emitted. Finally, we obtained

more than 2600 RFs along the WAP and 2650 RFs along the CAP. Totally more than 7000 RFs are calculated for the area of interest. Figure 4.5 displays two examples of RFs recorded in BALB and W18.

Moreover, we used common source time function for each event (Tseng & Chen 2006) to compute the RFs. High SNR station used as a reference station and the waveforms were aligned on the first P wave arrival time using cross correlation for each teleseismic event. To attain the source time functions, vertical components of an event with similar instruments along each profile were stacked. Two source time functions were calculated for each event representing each halves of the profile. When we compare two methods, both of them ensured consistent results when the SNR is high. Nevertheless, higher quality receiver functions were obtained in deconvolution with common source time functions when the SNR was low for the vertical component, therefore we united both approaches to estimate receiver functions at each station.

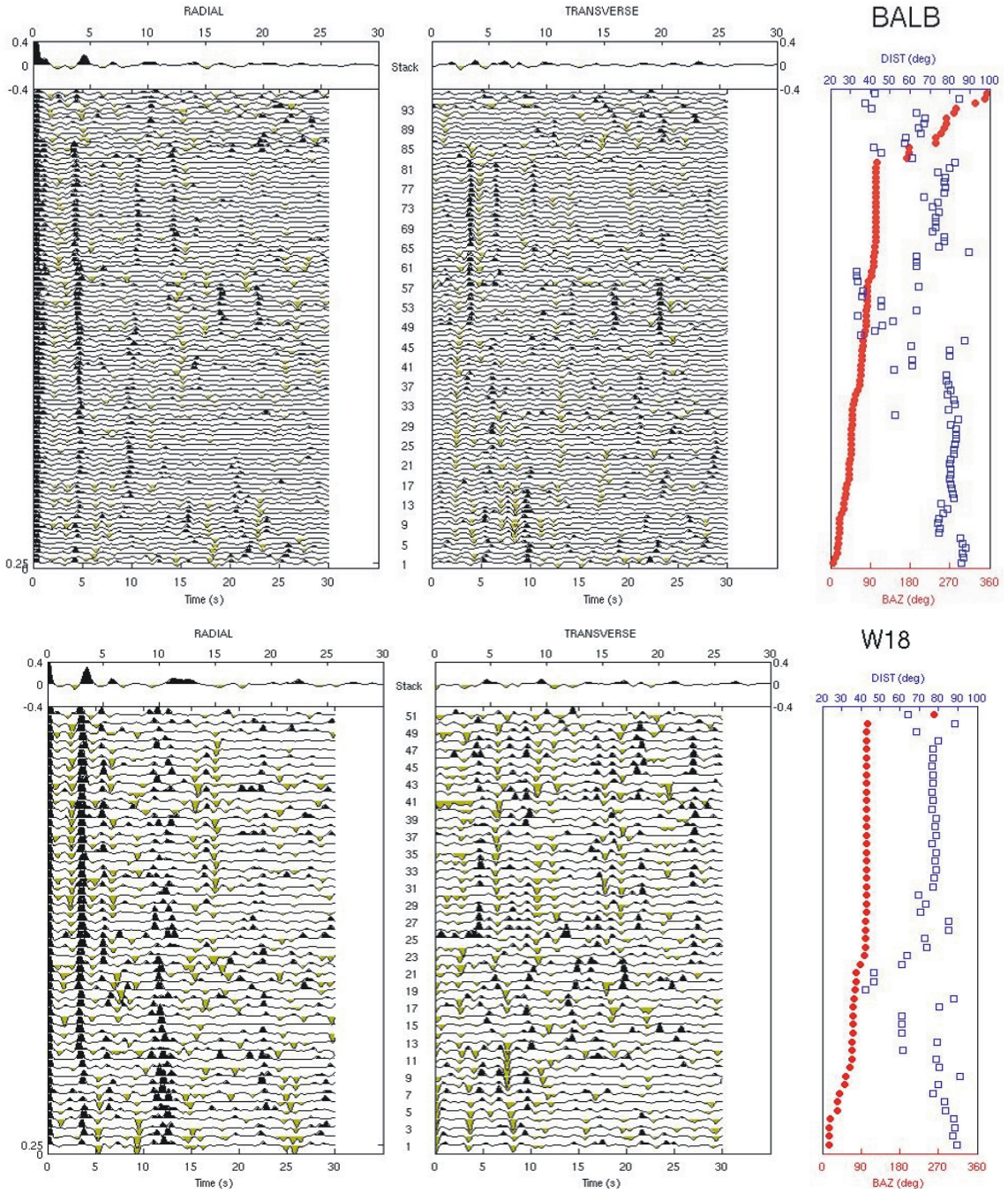


Figure 4.5. Two examples of computed radial and transverse receiver functions for stations BALB and W18.

5. RECEIVER FUNCTION ANALYSIS

The RF technique is used to determine crustal thickness and V_p/V_s ratios which provides reliable indications on the characteristics of crustal structure via H-k stacking (Zhu and Kanamori, 2000) described in chapter 5.1. In order to have a better idea on the accuracy of the estimated crustal parameters we also applied a stochastic search scheme based on the Neighbourhood Algorithm (Sambridge, 1999) which will be given briefly in the preceding chapter 5.2. Crustal thickness map for the area of interest will be given in chapter 5.3. To present high resolution images of lithosphere and upper mantle structure along nearly 650km transects crossing Western Anatolia and Central Anatolia, we performed CCP migration by using the method described by Zhu (2000) in chapter 5.4.

5.1. H-K Stacking

The initial estimate of crustal thickness (H) and V_p/V_s (k) obtained from a grid-search stacking of the Ps phase and the multiples, PpPs and PsPs+PpSs (Zhu and Kanamori 2000). The prominent signal following the direct P wave on the radial receiver function is the P-to-S converted wave (Ps) from the Moho discontinuity. The conversion point lies within 10 km in the horizontal distance from the station. The arrival time difference t_{ps} between Ps and P on the receiver function can be used to estimate the crustal thickness H beneath the station. The differential travel time between S and P waves used, therefore the thickness estimate is not sensitive to crustal P wave velocity, as much as to the crustal V_p/V_s ratio (K). This tradeoff between the H and K can be reduced significantly by adding multiple converted phases, namely PpPs and PpSs + PsPs (Zhu, 1993; Zandt et al., 1995). In addition including the multiples in the RF analysis provides additional information on the depth of the discontinuity and the average Poisson's ratio above it (Zandt and Ammon, 1995; Zhu and Kanamori, 2000). Therefore, we used a stacking algorithm, which sums the amplitude of receiver functions at predicted arrival times of converted phases for different crustal thicknesses H and V_p/V_s ratios, developed by Zhu and Kanamori (2000) (Please see chapter 3.2 for further information). This transforms the time domain receiver functions directly into the H-k domain without need to identify the converted phases and to pick their arrival times.

This analysis supposes that the incoming P wave is sampling the structure beneath the receiver composed of locally flat homogeneous layers. We stacked RFs with the estimated V_p values using unequal weights (0.7, 0.2, 0.1) for P_s phase and multiples, PpPs, PsPs+PpSs phases (Zhu and Kanamori, 2000). The resulting V_p/V_s values represent an average for the entire crust from the Moho to the surface. Poisson's ratio, which is proportional to V_p/V_s , is sensitive to variations in rock composition can be used to determine changes in the amount of quartz, iron, and magnesium in crustal rocks. Lower values of V_p/V_s (<1.71) tend to characterize more quartz-rich, felsic rocks, whereas higher values (>1.74) are associated with more iron and magnesium-rich, mafic rocks (Christensen, 1996). Three multiples add constructively hence amplitude of stacked traces is maximized. The success of the technique depends on the good azimuthal coverage of events and the existence of multiple reflected energy in the RFs (Karabulut et. al., 2013). The permanent broadband stations provided better estimations of the V_p/V_s (Figure 5.1) ratios when compared to one year deployment of temporary stations with V_p/V_s estimations with larger uncertainties. When the event coverage was poor we interpolated the crustal thickness and V_p/V_s between receivers. The variances of H and k can be calculated from the width of the energy spot in the H - k plane. Large uncertainties are due to the absence of multiple energy or the breach of the hypothesis of a locally flat, homogeneous Earth structure beneath the station. This analysis was performed for all the stations on the profiles and for all broadband stations, the results are presented in Table 1, 2 and 3 (see Appendix A, Table1, 2, 3). To develop the CCP migration and double-check the outputs of H - k stacking, V_p values were calculated from the earthquakes occurred on the profiles during the deployment. A total of 20 earthquakes with magnitudes $4.0 > M > 3.0$ were selected for this analysis. The earthquakes occurred within the 10km distance from the profile were located and travel-time distance curves were formed. The maximum offset was limited to 120km. Therefore, the raypaths from the hypocenter sample only upper and lower crust. Simple two layer velocity models for each travel-time curve were fitted and average V_p along ~ 120 km of the profile were obtained. We also utilized the earthquake clusters on the profiles to determine average V_p and V_s values from the Wadati diagrams. The V_p values at the receiver points are obtained from the regional V_p topography map (Komec and Karabulut, 2010) (see Appendix A, Table1, 2). Both methods; travel-time curves and H - k method lead us to consistent estimates of V_p/V_s ratios.

Figure 5.1 represents the results of H-k analysis at permanent station BLCB located within the Bornova Flysh Zone in the western Turkey. They have high S/N and relatively uniform azimuthal coverage. The Moho multiples can be observed clearly with a sharp Moho conversion at ~ 3 s. The crustal thickness and V_p/V_s estimated as 29 km and 1.695. The uncertainties on H and k are estimated from 95% of the maximum peak of the H-k image. Specially acceptable values; for H is 0.5 km and for k is 0.03 are presented in the H-k stack. The estimates of V_p/V_s and H from travel-time curves are reasonably consistent with H-k findings. Figure 5.2 indicates the results of H-k analysis at permanent station BALB located within the Sakarya Zone. It has a good S/N compared to other stations on the western profile. The Moho multiples can be observed clearly in Figure 5.2 with a sharp Moho conversion at ~ 4 s. The crustal thickness and V_p/V_s are estimated as 32 km and 1.85, respectively. LOD permanent broadband station, which is located in the Sakarya Zone near Ankara in the central Turkey, is shown in Figure 5.3. As expected, thicker crust with 37 km and 1.77 V_p/V_s ratio, sharp Moho conversions at ~ 5 s.

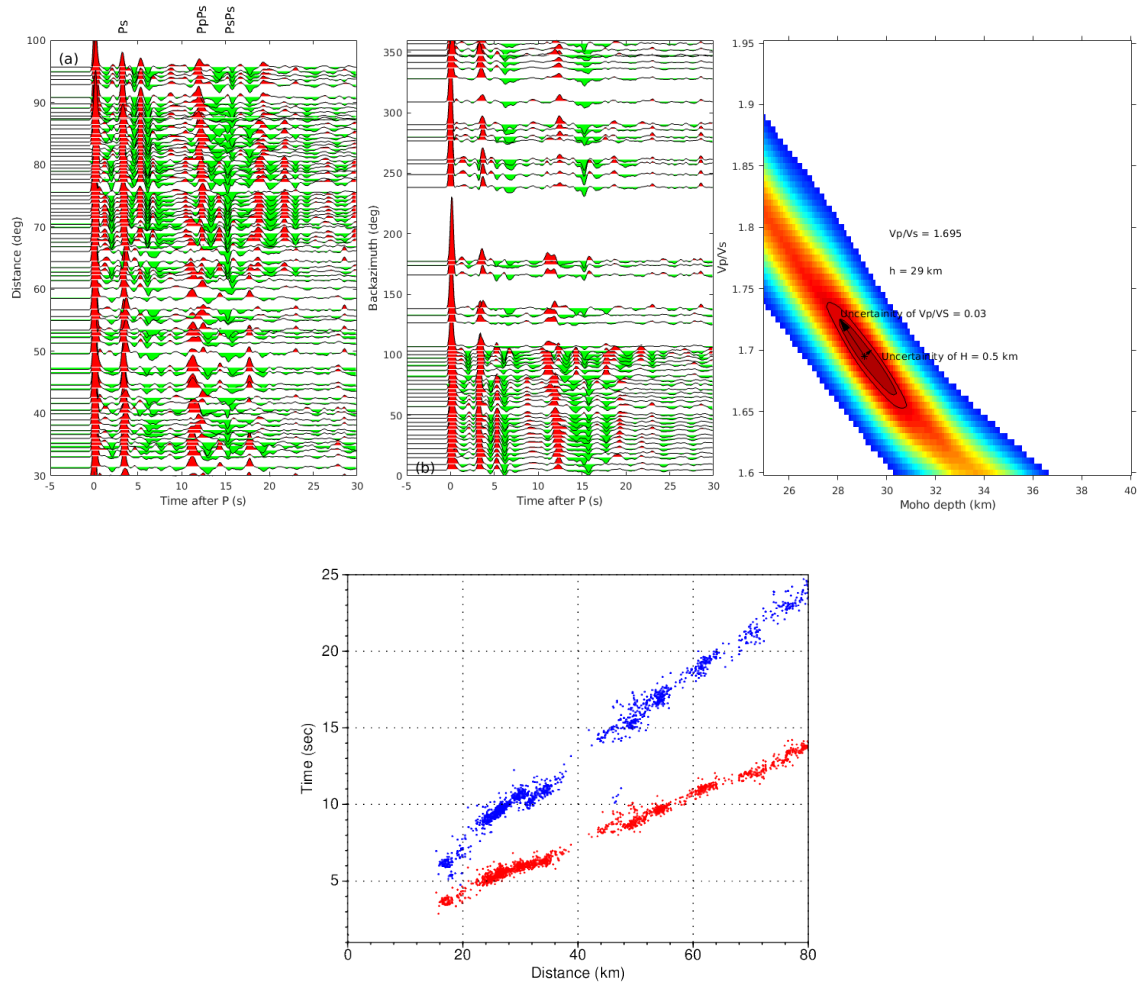


Figure 5.1. Top: RFs at station BLCB sorted by epicentral distance and backazimuth. Traces in every 0.4° are displayed. H-k stack of the RFs with estimated V_p/V_s and crustal thickness. Uncertainties of H (0.5 km) and k (0.03) are presented in the H-k stack. Bottom: Travel time observations of local earthquakes recorded at station BLCB. The average crustal V_p and V_s values are estimated from the slope of the related travel time curves (red dotted line: $V_p = 6.4$ km/s, blue dotted line: $V_s = 3.7$ km/s).

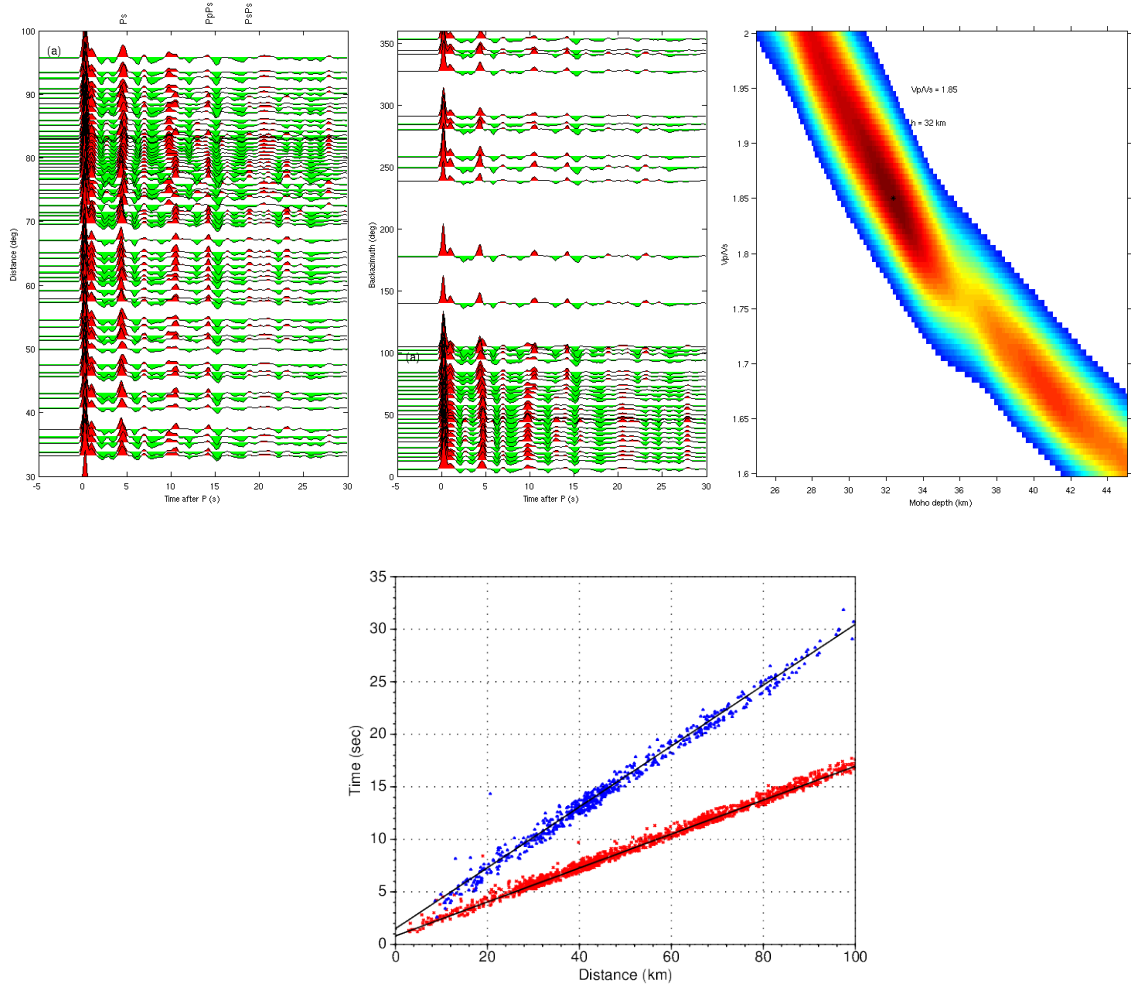


Figure 5.2. Top: RFs at station BALB sorted by epicentral distance and backazimuth. Traces in every 0.4° are displayed. H-k stack of the RFs with estimated V_p/V_s and crustal thickness. Bottom: Travel time observations of local earthquakes recorded at station BALB. The average crustal V_p and V_s values are estimated from the slope of the related travel time curves (red dotted line: $V_p = 6.2$ km/s, blue dotted line: $V_s = 3.5$ km/s).

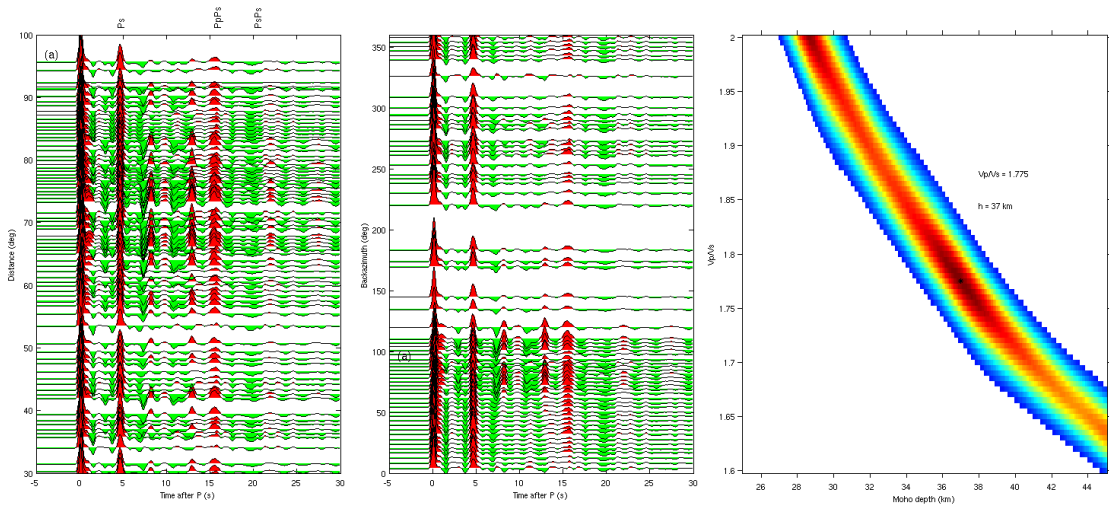


Figure 5.3. RFs at station LOD sorted by epicentral distance and backazimuth. Traces in every 0.4° are displayed. H-k stack of the RFs with estimated V_p/V_s and crustal thickness.

While H-k stacks are a fast and efficient way to estimate crustal thickness and average V_p/V_s ratios. The method assumes relatively simple layering in the crust with no azimuthal variations. A significant trade off between crustal thickness and V_p/V_s implies nonuniqueness and requires a priori knowledge on the range of parameters. In general the uncertainties of V_p/V_s is spread into a larger interval than crustal thickness. However, the real uncertainties are functions of a more complicated set of parameters. In this manner, in order to have a better idea on the accuracy of the estimated crustal parameters we also performed a search scheme based on the Neighborhood Algorithm (Sambridge, 1999) that is given in chapter 5.2.

5.2. 1-D Inversion

Receiver function inversion is well-known to be a complex non-linear problem. It is difficult or impossible to solve it with a linearized approximation since the linearization requires calculation of partial derivatives of data with respect to model parameters. Therefore, the derivative-free direct search methods are commonly used for this complex non-linear and non-unique problem. To check the precision of the estimated crustal parameters we also applied a search scheme based on the Neighborhood Algorithm (Sambridge, 1999). The Neighborhood Algorithm (NA) is a stochastic search method that

effectively samples the areas of interest of parameter space using Voronoi cells (for detailed information please see chapter 3.4). The receiver functions for all stations included in the study are inverted for a 1-D layered medium to determine the layer thicknesses, V_s and V_p/V_s by using a similar methodology as Sambridge (1999).

The crustal Earth model is divided into 8 horizontal layers, representing crust and upper mantle structures. The model has four parameters in each layer: the layer thickness (km), S-velocity at topmost point in the layer (km/s), S-velocity at bottommost point in the layer (km/s), and V_p/V_s in the layer. A linear gradient in velocity is assumed in each layer (Sambridge, 1999).

Seismic stations, BLCB in western Anatolia, BALB in WAP and LOD in the Central Turkey are presented below. In Figure 5.4, on the S wave velocity depth section, Moho happens to be at ~29 km and V_p/V_s is 1.71, which are very close to the values obtained from H-k analysis. Figure 5.5 presents the result of the inversion for BALB station. S wave velocity depth section, specifies the Moho depth as 32km which is exactly same with the H-k outcomes. In LOD station, shear wave velocity depth section indicates a deeper Moho with 34km depth and V_p/V_s as 1.78 in Figure 5.6 which proves the stability of the H-k stacks.

Estimated crustal parameters which are double checked with 1-D inversion are presented in map view in chapter 5.3.

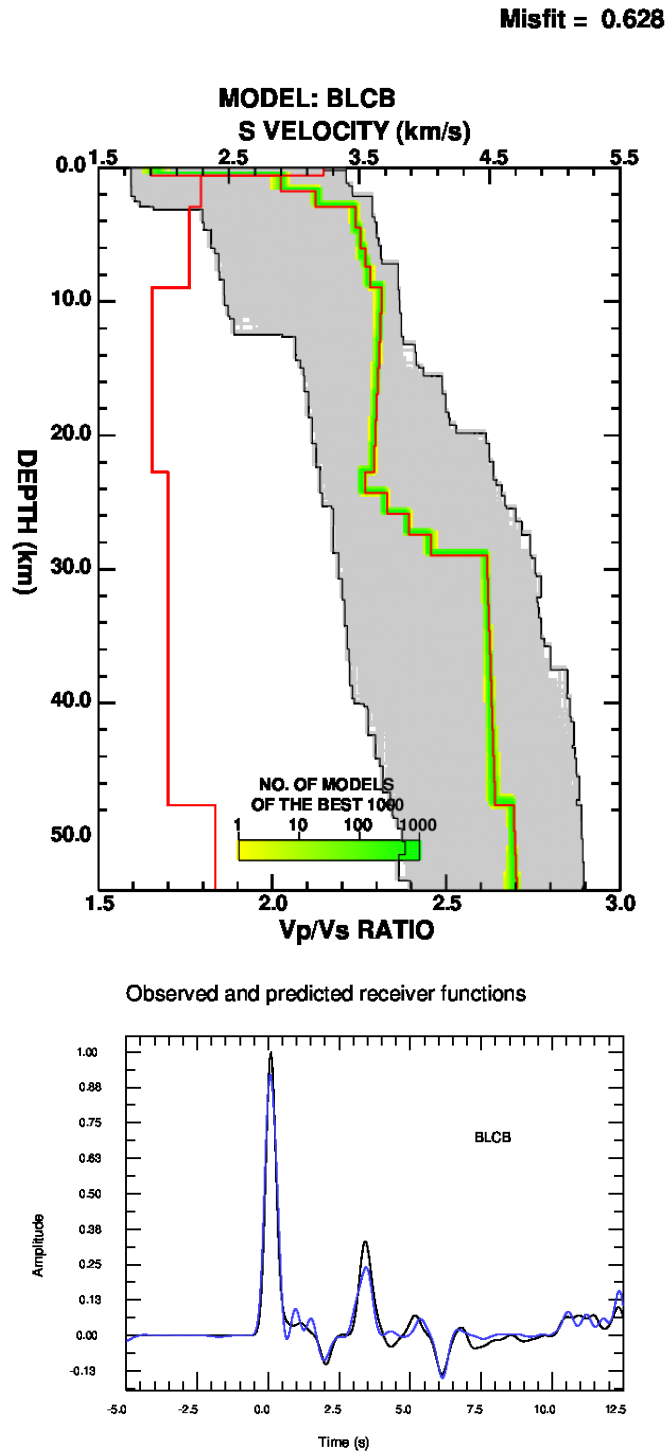


Figure 5.4. Inversion of the receiver function of the BLCB broadband station for the shear wave velocity structure using the neighborhood algorithm. Top: Density plot of the best 1000 data-fitting S-velocity models generated with the first random seed. The best data fitting model is plotted in red. The colour scale shows the increase in data-fit, from yellow to green. Bottom: RFs of the true (black) and best fit models (blue).

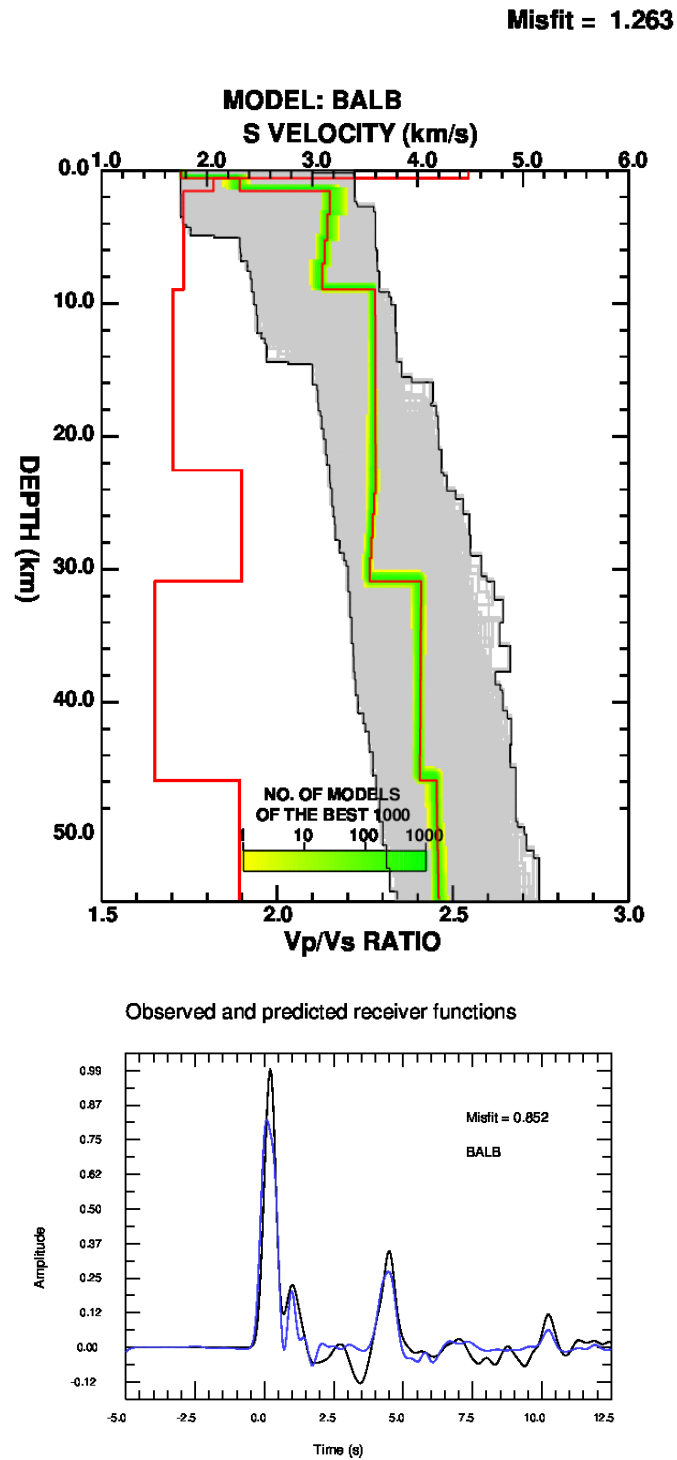


Figure 5.5. Inversion of the receiver function of the BALB broadband station for the Shear wave velocity structure using the neighborhood algorithm. Top: Density plot of the best 1000 data-fitting S-velocity models generated with the first random seed. The best data fitting model is plotted in red. The colour scale shows the increase in data-fit, from yellow to green. Bottom: RFs of the true (black) and best fit models (blue).

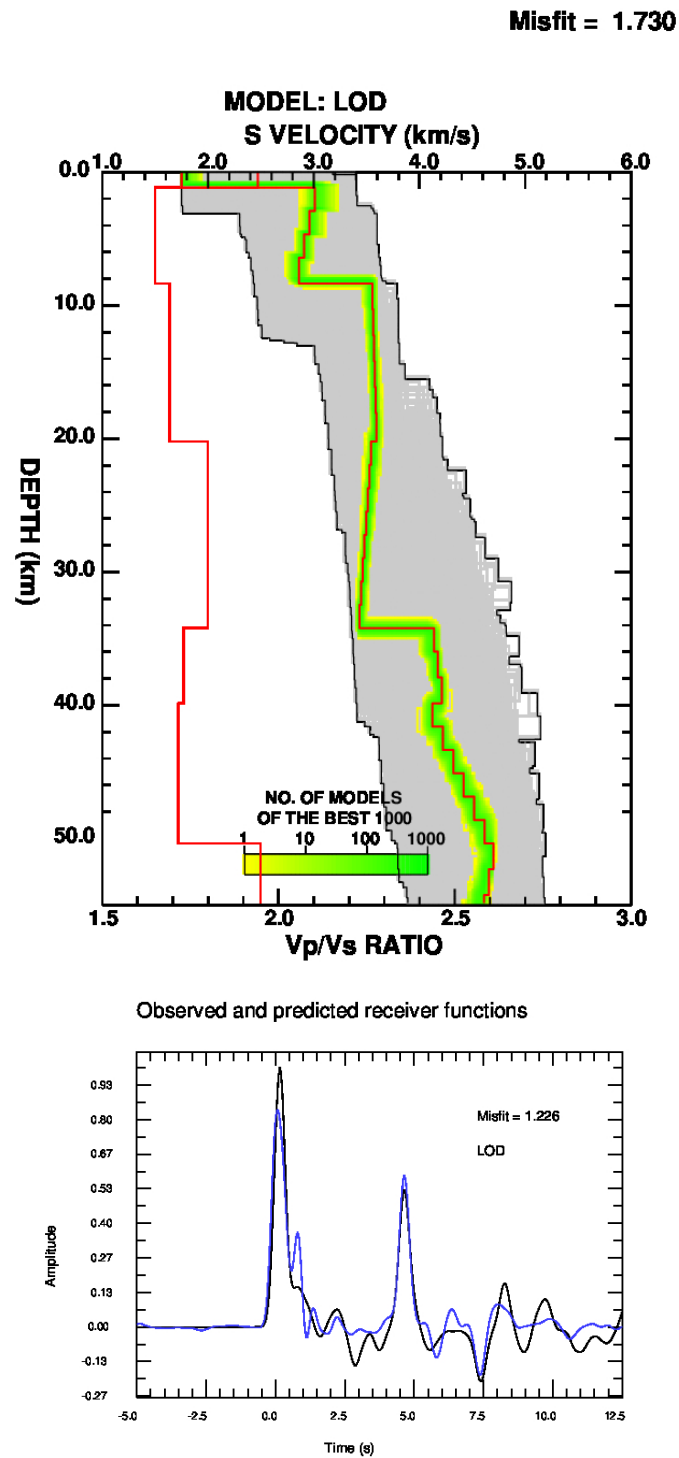


Figure 5.6. Inversion of the receiver function of the LOD broadband station for the Shear wave velocity structure using the neighborhood algorithm. Top: Density plot of the best 1000 data-fitting S-velocity models generated with the first random seed. The best data fitting model is plotted in red. The colour scale shows the increase in data-fit, from yellow to green. Bottom: RFs of the true (black) and best fit models (blue).

5.3. Crustal Thickness Maps

Utilizing all available crustal parameters from H-k stacking and 1-D inversion we carried out crustal thickness maps in order to see the change over a strongly deformed area on the western Turkey and surrounding region. 135 stations have a good spatial coverage in Turkey (with a maximum 40 km inter station spacing) and surrounding countries; mainland Greece, Bulgaria and Romania, allow us to obtain reliable estimates of crustal thickness variations with uncertainties of 2-4 km. In Figure 5.7 top panel we plotted the point-wise estimates of the crustal thickness and interpolated for a crustal thickness map (Figure 5.7 bottom) by using a Variogram-Kriging algorithm (Chu 2000). Algorithm can be seen as a point interpolation which uses a point map as input and returns a raster map with estimations. The estimations or predictions are calculated as weighted averages of known input point values. To overcome the deprivation of data in the Black Sea, we included the crustal thicknesses estimated by Starostenko et al. (2004) and Yegorova et al. (2013) from the modelling of gravity data.

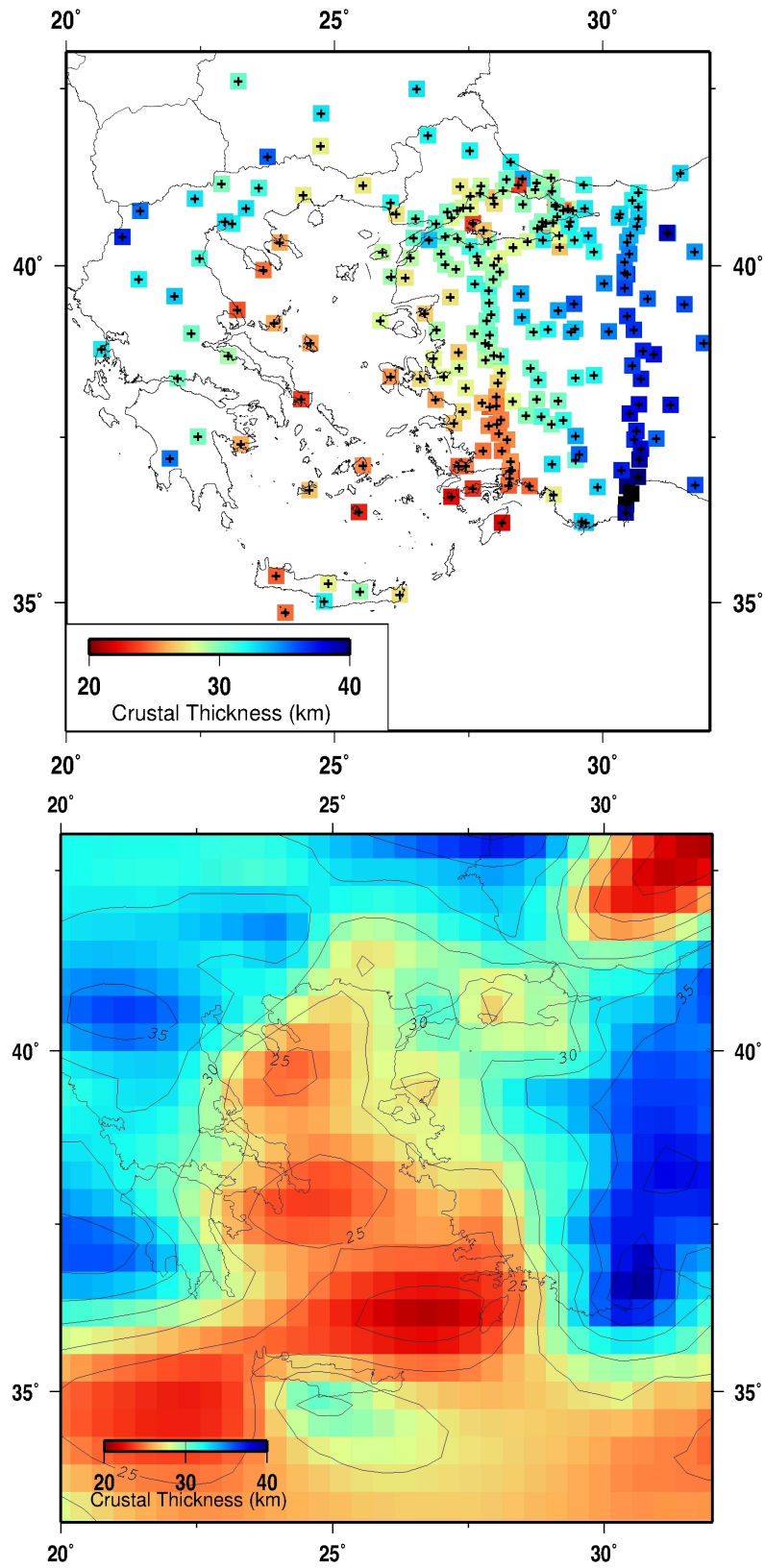


Figure 5.7. Top: The map of the seismic stations used in this study. The colors indicate the crustal thicknesses estimated from receiver function analysis. Bottom: the crustal thickness

map computed from the receiver function measurements at stations shown in top figure. The crustal thickness estimates for the Black Sea (Starostenko et al. (2004); Yegorova et al. (2013)) are included prior to interpolation. Blue color indicates the thick crust (>40 km), while red colors indicate thin crust (<30 km).

Mainland of Turkey is surrounded by a thin crust from north, south and west. Thinnest crust observed in Black Sea, Aegean Sea and eastern Mediterranean Sea with values less than 25 km. Likewise thin crust (25-32 km) is present in western Anatolia due to N-S extension. Crustal thicknesses are increasing from west to east, across the central Anatolia, which is a broad transition region between the thin crust of western Anatolia and the thicker crust of eastern Anatolia, it is averagely 37 km. To investigate the crustal thickness changes in details from north to south and east to west we performed CCP imaging along two dense transects WAP and CAP which are presented in chapter 5.4.

5.4. CCP Imaging

CCP stacking technique developed by Zhu in 2000. Dueker and Sheehan used CMP stacking method by geographically binning receiver functions according to their piercing points at certain depth. The shortcoming of the method is that the change in the location of piercing point with depth due to the slope of the ray path (Zhu, 2006). CCP is an effective technique for subsurface imaging; both shallow and deep crustal structures can be delineated (Please see chapter 3.3 for further information). Decent azimuthal coverage is required to minimize the errors and enhance the signals. The success of CCP stacking strongly depend on an array of densely distributed stations. In this manner we have deployed 2 dense profiles; WAP and CAP along the coast of the Aegean sea crossing almost perpendicular to the tectonic strike of east-west trending structures and performed CCP stacking technique along the profiles. CCP results will be briefly examined in the following sections 5.4.1 and 5.4.2.

5.4.1. Western Anatolia Profile (WAP)

The North-South extending WAP centered on 28 °E displayed in Figure 5.8 below.

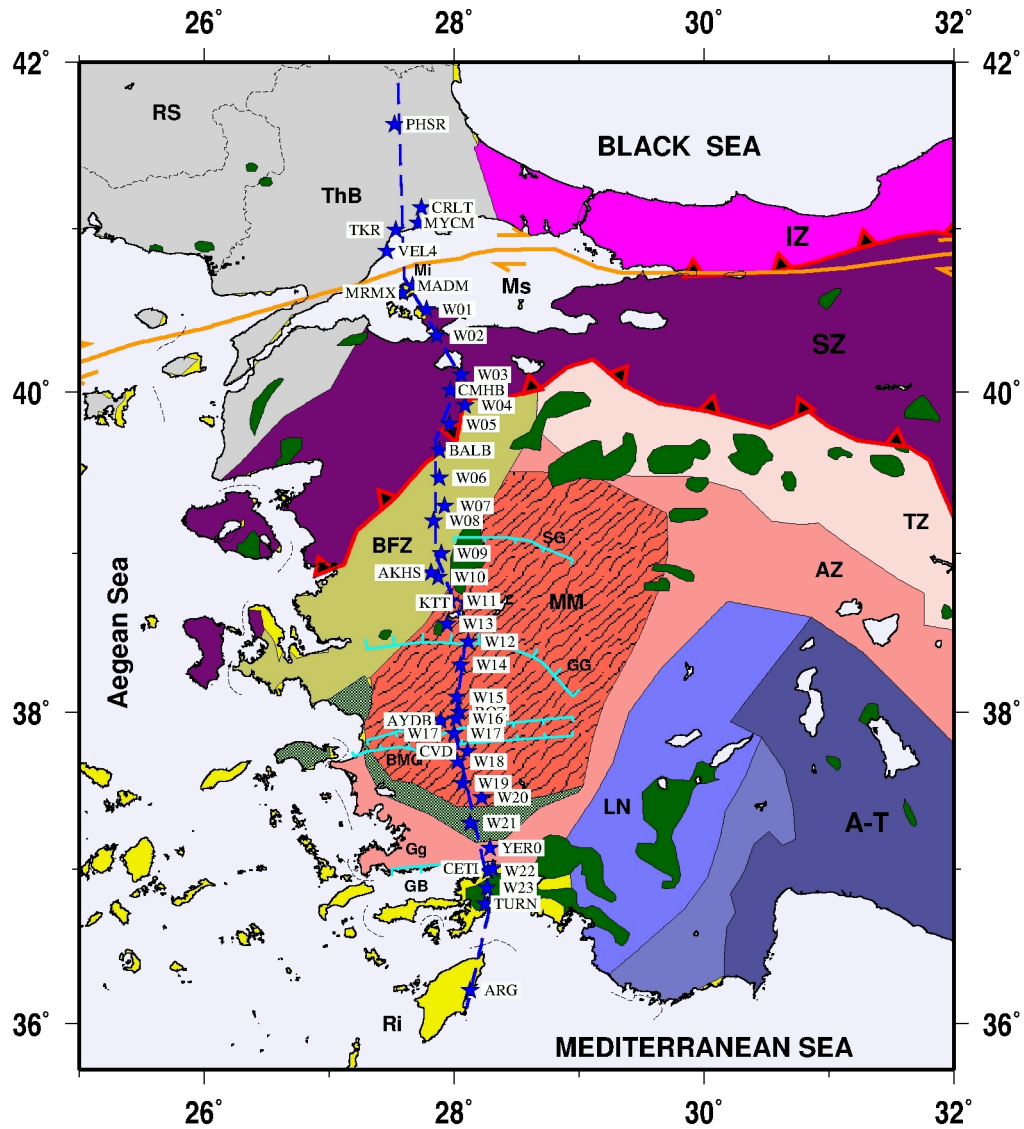


Figure 5.8. Seismic stations of WAP installed during SIMBAAD experiment between 2007-2008, blue stars indicates the location of the stations. Main tectonic features and morpho-tectonic units are also labeled; ATB, Anatolide-Tauride Block; AZ, Afyon Zone; BFZ, Bornova Flysch Zone; BMG, Büyük Menderes Graben; GG, Gediz Graben; GB: Gökova Bay; Gg, Gökova Graben; SG, Simav Graben; IZ, Istanbul Zone; LN, Lycian Nappes; MM, Menderes Massif; PT, Pontides; RS, Rhodope-Strandja Basin; SZ, Sakarya Zone; IASZ, Izmir-Ankara Suture Zone; Ms, Marmara Sea; Mi, Marmara Island; NAFZ, North Anatolian Fault Zone; Ri, Rhodos Island; ThB, Thrace Basin; TZ, Tavşanlı Zone.

Stures are shown by red lines with black triangles on. The main normal faults of the grabens are shown by the thin light blue lines. The magenta line shows the NAF. The ophiolite outcrops labeled with dark green units. Western Anatolia profile shown as a blue

line. Geological map modified from Okay and Tüysüz, 1999, and van Hinsbergen et al, 2010 (Karabulut et al., 2013).

CCP migration, requires a knowledge or assumption on the crustal P-wave velocity, in this sense we computed average crustal P-wave velocities from local earthquakes with epicenters located within 10km of the profile (please see chapter 5.1 for further information) in addition to the initial estimates (Appendix A, Table 1) from grid-search stacking. A reference velocity model, which is a modified IASP91 Earth model with variable P-wave velocity and V_p/V_s beneath each station, constructed along WAP (Appendix A, Table 1). First, we calculated the ray-paths of RFs using the constructed background velocity model. Second, amplitudes corrected for the incidence angle effect. Third, amplitudes at each point on the RF assigned to the corresponding location using the delay time with respect to direct P wave where the P to S conversions occurred. This amplitudes stand for the velocity change of the medium at the conversion point. Fourth, the 2-D model space was divided into constant size cells and all amplitudes of radial RFs of the crossing ray paths summed up, in each cell to obtain the average amplitude and variance. The RFs back-projected from the receiver to the source through these cells with constant ray parameters. The horizontal dimensions of the cells depend on the wavelength of the signal where vertical dimension is related with the sampling rate.

The horizontal resolution of CCP image is determined by the Fresnel zone of the incident P wave that varies with depth z as $\sqrt{\lambda z}$. (Zhu et al., 2006). For a Moho depth of 30 km, an incident P wave with a frequency of 0.3 Hz, the radius of the corresponding Fresnel zone is approximately 10 km at 30km depth for upper-mantle P -velocity of 8.0 km/s and 2-4km at the surface. The vertical resolution depends on seismic discontinuities being separated by more than 1/4 of the S -wave wavelength, for this study somewhere in the range of 3.5–4km for an upper crust P -velocity of 5.0 km/s. The migration mesh was 3 km in the horizontal direction and 0.5km in the vertical direction. Therefore, we used a 15 km horizontally and 2 km vertically smoothing window in order to average a 3-D structure over the Fresnel zone, while avoiding over smoothing and related artefacts of the image. Besides, we computed CCP images for 3 back azimuth ranges (30° - 150° , 150° - 270° , 270° - 30°) to check the azimuthal dependency of the images on the earthquakes sources. The uncertainties on the Moho depth are estimated from the migrated RF depth sections. However the true

uncertainty comes from the uncertainties on V_p/V_s and V_p . As Zhu stated in 2006, a 3 percent uncertainty on V_p/V_s results in a 2 km error on the Moho depth, while the same uncertainty on V_p results in a 1 km error

The P to S converted teleseismic phases are migrated into the spatial images of the lithosphere and upper mantle beneath the receiver array. Appendix A, Table 1 shows that V_p/V_s undergoes rapid and large variations beneath the profile, while V_p varies smoothly. As there might be a trade-off between crustal thickness and V_p/V_s in the H-k analysis, we furthermore tested the accuracy of our estimates by computing CCP migrated sections of the PpPs and PpSs + PsPs multiples which are more sensitive to V_p/V_s than the primary Ps. (Wittlinger et al., 2004, Hetenyi 2007, Karabulut et al., 2013). If the image obtained from the migrated multiples displays a converted phase at the same depth as the Moho in the Ps migrated section, the initial estimate of crustal thickness and V_p/V_s is reliable (Figure 5.9). If the converted phases do not coincide, their depth difference can be used to measure the actual value of the crustal V_p/V_s ratio.

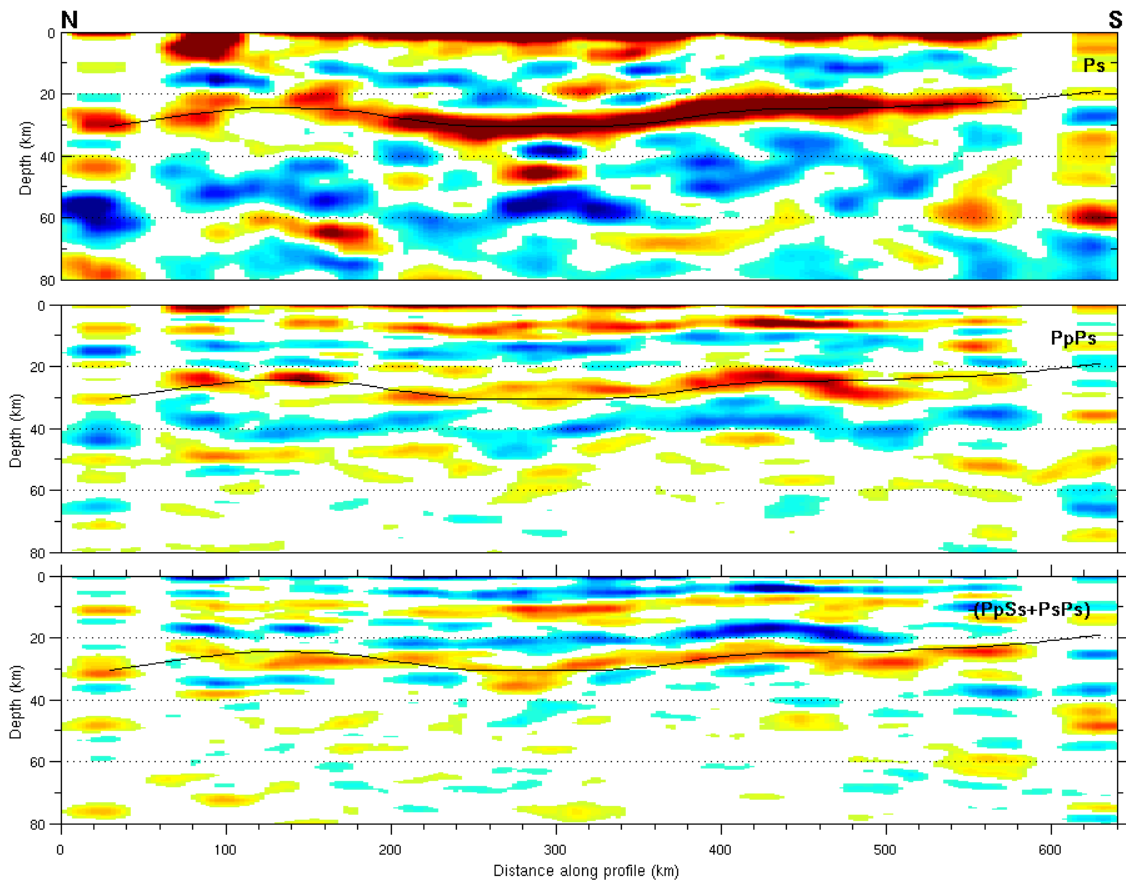


Figure 5.9. Migrated depth sections of Ps (a), PpPs (b) and PpSs+PsPs (c) modes. The black line shows the crust-mantle boundary.

The Moho depth estimates in the three sections should be similar if the velocity model used in the migration is accurate. We used larger smoothing parameters in both vertical and horizontal directions due to the strongly scattered multiple energy on the PpPs and PpSs+PsPs sections. The three images indicate consistent results beneath the Sakarya Zone and Menderes Massif while dissimilarities are observed beneath the Marmara Sea and the Aegean. Fullest extend, the strong similarities between the three migrated sections indicate that the V_p/V_s model is accurate and the depth section of Figure 5.10 is reliable.

5.4.1.1. Results. The results of CCP analysis is presented in Figure 5.10 below.

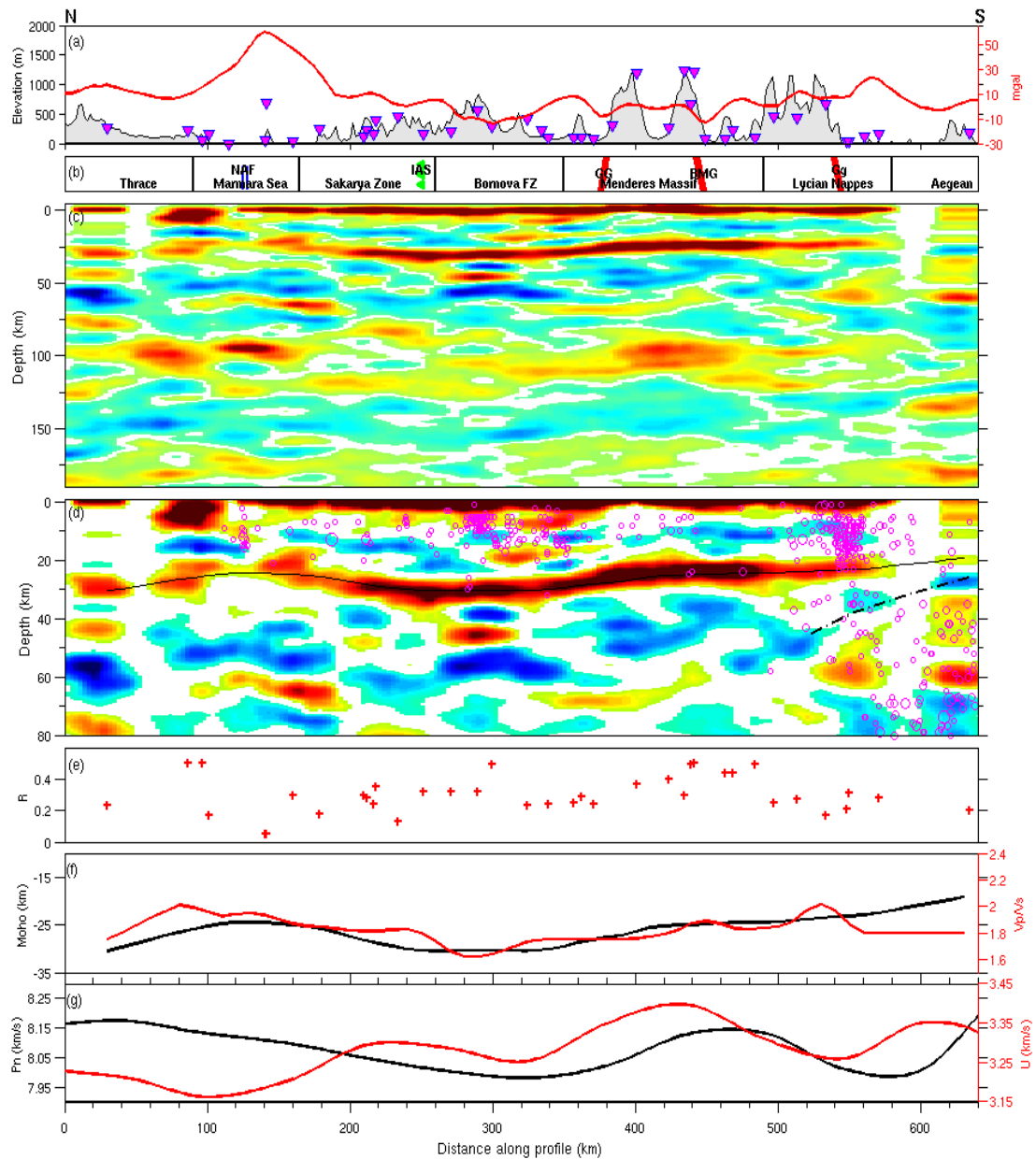


Figure 5.10. Migrated depth section of radial receiver function records of the WAP. Distance is measured with respect to the northernmost station. (a) Topography profile (black), receiver locations (magenta) and Bouguer gravity anomaly (red). (b) Geological units along the profile (c) Common-conversion point depth migrated cross-section (no vertical exaggeration). Red represents positive P-to-S converted amplitudes and indicates sharp increase in velocity with depth. The Moho is the continuous band between 26 and 32 km depth. (d) Common-conversion point depth migrated cross-section with seismicity and major interpreted structures (vertical exaggeration 2). The seismic activity covers a period from 1998 to 2010 with magnitudes $M_l > 3.0$. (e) Ratio R of stacking amplitudes for each

station. (f) Crustal thickness (black) and V_p/V_s (red) variations. (g) 20 sec Love wave group velocities (red) and P_n velocities (black). Same abbreviations as in Figure 5.8.

Figure 5.10 indicates the results of CCP analysis. The top panel in Figure 5.10a shows the topography and Bouguer gravity anomaly along the profile (Ateş et al., 1999). The gravity values are high in the northern part of the profile reaching to 50 mgal in the Marmara Sea and decreasing towards south with increasing topographic variations. Topography correction was also applied at each receiver location as time delays computed using constant velocity. The second panel (Figure 5.10b) indicates locations of the major geologic and tectonic boundaries along the profile.

Figure 5.10c shows the CCP time-to-depth migrated section with no vertical exaggeration. The migration takes into account the lateral variations of the V_p/V_s , which are estimated from the H-k stacking and updated with the results of CCP stacking of multiples. Positive amplitudes (red) are generated by a velocity increase with depth whereas negative amplitudes (blue) correspond to a velocity decrease with depth. Figure 5.10d shows a zoom of the CCP image for the upper 80 km which gives more details on the Moho topography and intracrustal features (vertical exaggeration: 2). The seismicity within a band of 20 km along the profile is also displayed on the image. The high seismic activity is observed in the Marmara Sea, between the stations W06 and W11, on the southern end of the profile in Gökova Gulf and in the subduction zone. The majority of the earthquakes are located in the upper part of the crust as expected. The bold black line is the conversion on the Moho and dashed lines indicate other discontinuities such as African lithosphere dipping northward with an angle between 20° - 30° from approximately 30 km depth beneath Rhodos Island to ~ 50 km beneath station YER in the Lycian Nappes where it terminates suddenly. The crossing rays are an indication of increased resolution of the CCP image. The majority of the crossing rays take place above the depth of 50km. Marmara Sea and Aegean Sea provinces are not well resolved due to the lack of crossing rays because of large station spacings. We estimated ± 2 km uncertainty on the picks of the Moho from the migrated RF depth sections.

Computed R factors shown in Figure 5.10e. In order to quantify the effectiveness of the Moho in producing wave conversions. The stacked amplitude of the Ps and multiple phases normalized by the amplitude of the direct P as suggested by Nair et al. (2006). The

amplitude of the converted Moho phases depends on the velocity contrast between crust and mantle, the thickness of the Moho transition zone and the short-scale topography of the Moho. A sharp Moho with strong velocity contrast produces Ps and multiples with strong amplitudes, leading to a high value of R (Nair et al. 2006, Karabulut et al., 2013). The regional average of R is 0.25, while the largest values (~ 0.45) are observed beneath the southern Menderes Massif (Figure 5.10e).

Figure 5.10f shows the final estimates of V_p/V_s (red curve) and crustal thicknesses (black curve) from the CCP images, which may differ from the initial estimates of H-k, stack (Appendix A, Table 1). The V_p/V_s ratio provides useful information on the composition of the continental crust. Composition, temperature, pressure, onset of partial melting, presence of fluid filled cracks and anisotropy is the some of the factors that are effecting the V_p/V_s of the rocks (Zandt et. al., 1995). The presence of crustal fluids or partial melting decrease the S-wave velocities, on the other hand mafic content, metamorphic grade will increase the P-wave velocities. Both will produce high V_p/V_s and thus high Poisson ratios. High values tend to correspond to the rocks of more Mafic composition, while low values are associated with rocks that contain large amounts of quartz (Fountain & Christensen 1989). The crustal average V_p/V_s ratio measured along the transect ranges from 1.65 to 2.0 (red curve in Figure 5.10f) with an average of 1.78, slightly above the global average of continental crust (Christensen 1996).

Overall, the Moho is observed as laterally continuous positive amplitudes between 25 and 32 km depth (Figures 5.10c and 5.10d). The PpPs multiple appears with laterally discontinuous positive amplitudes in the 90–120 km depth range in Figure 5.10c where as Ps phase appears between 25-32 km. In Thrace Basin, the Moho depth is ~ 29 km. According to Görür and Okay, there is nearly 9km thick sedimentary basin, which induces strong multiples that altered the migrated image to larger depths. Crustal thickness decreases sharply from 29 km to 25 km beneath the Marmara Sea. The high gravity values (~ 50 mgal) also document the crustal thinning (Ateş et al., 1999). The transition from the Marmara Sea to the Sakarya Zone displays a gradual thickening of the crust from 25 to 30 km. In the Sakarya Zone, the crustal thickness increases to a maximum of 32 km beneath the Izmir–Ankara Suture. From the Sakarya Zone to the Lycian nappes in the south, the crust–mantle boundary is clearly defined by a strong Ps and multiples, giving R values larger than 0.2.

Once more, the Moho depth decreases smoothly from its largest value of ~ 32 km beneath the Izmir–Ankara Suture to ~ 28 km beneath the MM (Figure 5.10f). The Moho below the MM is relatively flat and continuous. It is characterized by Ps and PpPs phases of very strong amplitudes as shown by the CCP section of Figure 5.10c (PpPs multiple in the 90–120 km depth range) and the highest values of R Figure 5.10e. Further south beneath the LN we observe changes both on the character of the reflectivity and the depth of Moho. The amplitude of the converted phase weakens abruptly at the stations of the Mediterranean coast and the crustal thickness decreases to ~ 20 km beneath the Rhodos Island at the Southern end of the profile. We also display in Figure 5.10g Love wave group velocities (Cambaz and Karabulut, 2010) and Pn velocities along the profile (Mutlu and Karabulut, 2011).

5.4.1.1. Discussion. Main feature of the continental extension provinces is crustal thinning. Due to the N-S extension in western Turkey, the average crustal thickness measured along the profile is low with 27 km. Our high-resolution lithospheric image spanning the whole width of western Turkey is consistent with the sparser observations of Saunders et al. (1998), Zhu et al. (2006), B'ecel et al. (2009) and lower resolution Moho map of Mutlu & Karabulut (2011). At full length, Moho depth estimates are 1 to 5 km smaller than the measurements of Zhu et al. (2006) conducted at the same locations (BALB, BOZ, central Menderes) using the same RF analysis. The difference arose from the assumed V_p/V_s ratios. Zhu et al. (2006) had only a few broadband stations and had to assume a constant V_p/V_s of 1.76 for the CCP migration along the profile in the Central Menderes Massif where we find 1.81 (Appendix A, Table 1). Our array is only composed of broadband stations with many years of recordings at the permanent stations. Therefore our estimates are probably more trustworthy than those of Zhu et al. (2006). We checked the results of the H-k stack by migrating the multiples (Figure 5.11). In the same way, crustal thickness is 25 km beneath Rhodos Island (station RODO) assuming that V_p/V_s is 1.73 in Sodoudi's 2006 study, where we find 19 km at station ARG with measured V_p/V_s of 1.85. Becel et al. (2009) estimated a crustal thickness of 26 km in the Northern Marmara trough from offshore–onshore refraction and marine reflection profiles, which is very close to the 25 km that we measure at station MRMX.

The minimum 25-km thickness observed beneath the Sea of Marmara and the Menderes Massif is coincide with the average crustal thickness of Makris (1978) reflection study or inversion of gravity data (Tirel et al., 2004). The average crustal thickness along our profile, 27 km, is slightly larger than the average crustal thickness of 25 km estimated for the Aegean Sea by Tirel et al. (2004). The uncertainty in Moho depth determination is 2 km, when this is considered 2 km difference is acceptable. We observe a minimum crustal thickness of 20 km at the southernmost end of the profile beneath the Mediterranean coast and the Island of Rhodos like Tirel et al. 2004.

The flat and continuous Moho imaged in the Basin and Range extensional province of Western U.S.A. by seismic reflection profiles was interpreted as a young feature related to Cenozoic extension (Klemperer et al., 1986; Hauser et al., 1987), where topography had been wiped out by ductile crustal flow at the regional scale (e.g. Block and Royden, 1990). Since then, a flat Moho is considered as the signature of stretched continental crust and it has become a key constraint in models of metamorphic core complexes (e.g. Tirel et al., 2008). The smooth topography of the Moho, with a maximum depth change of 6–7 km along 150 km distance from the Sea of Marmara (25 km) or the Menderes Massif (25 km) to the Bornova Flysh Zone (31.5 km) indicated in Figure 5.10. No sharp Moho depth change is imaged beneath the grabens of the Menderes Massif or Sea of Marmara, although our station coverage is not adequate there to detect Moho depth changes at spatial scale shorter than 20–30 km. Moreover, the Moho is flat (within 2 km) beneath the Central and Southern Menderes Massif. The flat Moho at regional scale is typical for continental extensions like the Basin and Range (Klemperer et al. 1986; Hauser et al. 1987) or the Aegean Sea (Tirel et al. 2004). However, the Moho beneath Western Turkey is, not as flat as beneath the Basin and Range, as lateral Moho depth differences of 6–8 km are observed along the profile. Zhu et al. (2006) and Aktuğ et al. (2009), assume that the crustal thickness in the presently undeforming plateau of Central Anatolia is representative of the crustal thickness before extension started in Western Anatolia.

In Figure 5.10d, beneath the northern MM laterally located repetitive north-dipping conversions are detected. Their polarity is alternatively positive (red), negative (blue) and positive again from surface respectively. The shallowest conversion intersects the surface in the vicinity of the southern bounding fault of the Gediz Graben. This set of signals

interpreted as the conversion at the base of the sediments of the graben and its multiples (Karabulut et al., 2013). According to Yılmaz et al. (2000), the thickness of the sedimentary infill of the Gediz Graben is more than 3 km. However we observed approximately 10 km sedimentary infill in the migrated section of Figure 5.10d. Drawback of using vertically constant V_p and V_p/V_s for the whole crust is that depth estimates are not accurate for shallow structures. More realistic larger values of V_p/V_s in the shallow crust would move the interfaces to shallower depths. The second conversion at a depth of ~ 20 km has amplitude and time suggesting that it may be a multiple bouncing within the graben.

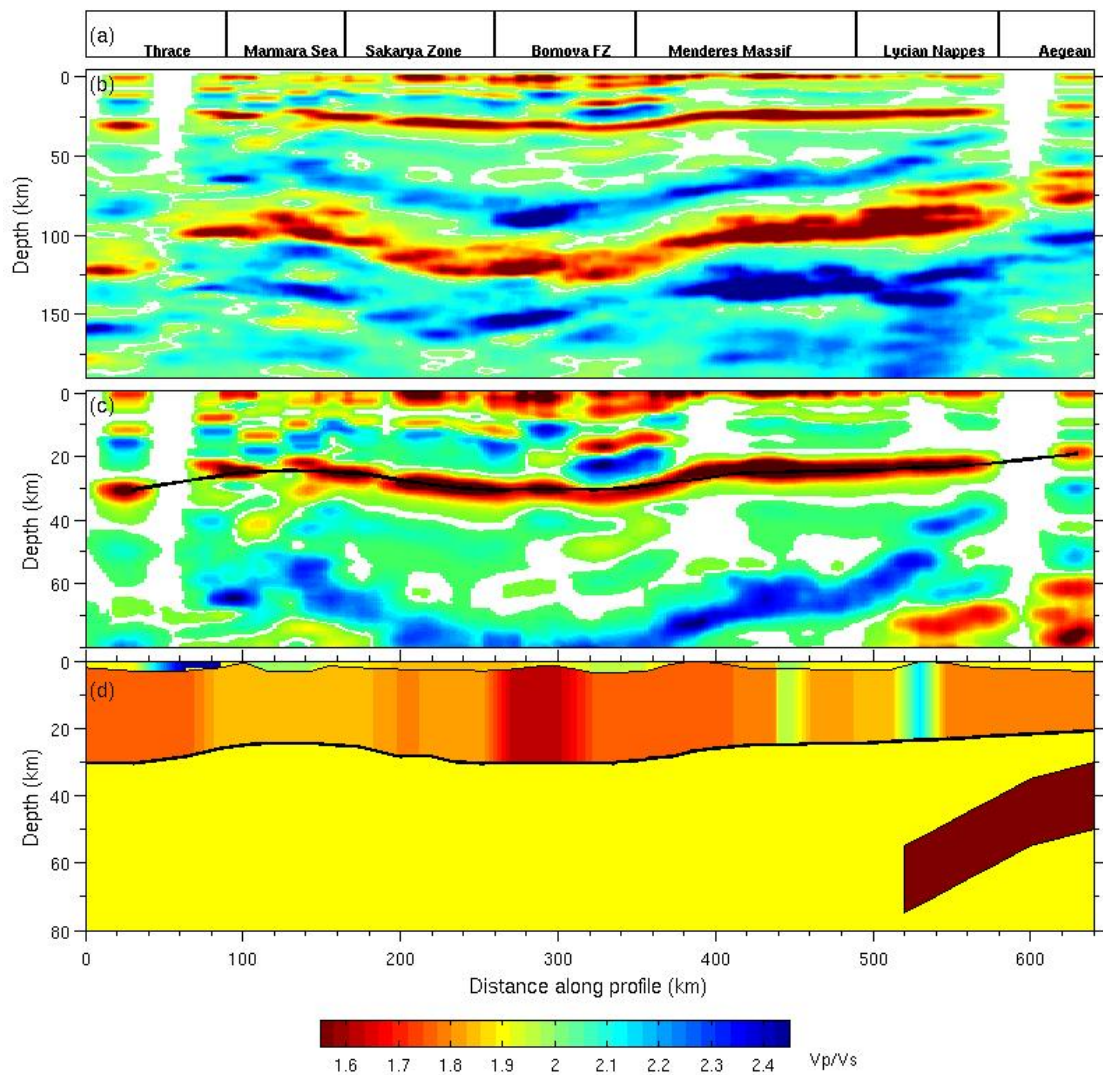


Figure 5.11. (a) Synthetic-CCP-migrated depth section computed from the crustal thickness and V_p/V_s models estimated in this study (Appendix A Table 1). (b) Synthetic-CCP-migrated depth section zoomed for the upper part of model response. (c) Model

geometry and V_p/V_s used for the synthetic CCP depth section. Layer parameters for the subducting plate; $V_p = 6.7$ km/s, $H = 15$ km.

Synthetic CCP section from the crustal thicknesses and V_p/V_s model determined from the receiver-function analysis was computed to check the accuracy of the crustal model obtained from the CCP analysis and see whether the converted energy observed above the crust–mantle boundary may be explained by the shallow structure (Figure 5.11). Synthetic RFs are computed for each station using the 1-D velocity models of Appendix A, Table 1 and the reflectivity method. A shallow structure to the 1-D velocity model beneath each station (Figure 5.11d) were added to improve the fit to the observed depth section of Figure 5.10d. However, the thickness and velocity of the shallow layers are not well known. From reflection and wide-angle refraction surveys performed by Becel in 2009, the thickness of the sediments in the Marmara Sea is known to be 3 to 5 km. In the Thrace basin, it is reported that the maximum thickness might exceed 9 km (Görür & Okay 1996). The thickness of the sediments was reported as at least 3 km from a drilling by the Turkish Petroleum Company (Yılmaz et al. 2000) in the Gediz Graben. However, the shear wave velocities are unknown. Overall, we constructed the shallow velocity structure shown in Figure 5.11d by trial and error under the above-cited constraints to have similarity with the CCP image of Figure 5.10. The synthetic RFs are computed with the same source-station geometry as the observed data. They are subsequently migrated to depth with the CCP technique using the same V_p , V_p/V_s and crustal thickness models as for the migration of the observed RFs (Appendix A, Table 1).

Trial-and-error modelling of the shallow structure successfully leads to a synthetic depth section similar to the observed section (Figure 5.11c). Minor differences on the Moho topography beneath the Gediz Graben are seen based on assuming a constant V_p/V_s ratio for the whole crust and not accounting for the shallow structure in the CCP migration. However, the converted energy observed inside the crust beneath the Gediz Graben in the synthetic section fits well with the observations, confirming the hypothesis that the seemingly intra-crustal conversions of Figure 5.10d are, in fact, produced by the very shallow structure (Karabulut et al. 2013). Similarly, the apparent upper to mid-crustal signals observed beneath the Thrace basin and the Marmara Sea are conversions at the base of the sediments migrated to incorrect depths by the single-layer velocity model. We concluded on

the absence of intracrustal interfaces due to all signals observed at mid or lower crustal depths in the migrated section are artefacts. We could not identify the main geological structures that could have induced velocity contrasts inside the crust, like the Izmir–Ankara suture or the detachments faults of the Menderes metamorphic core complex.

Sea of Marmara which is intersected by the NAF and the Menderes Massif have similar Moho topographies with a small uplift of 6-8 km in a broad scale of 150 km distance. Menderes Moho anomaly has the same width with Menderes Massif, whereas the Marmara Moho anomaly is significantly wider than the Sea of Marmara (Figure 5.10). This suggests that the broad-scale crustal thinning observed beneath the Marmara is not associated with the late opening of the relatively narrow pull-apart basins of the North Marmara Trough (Şengör et al. 2004, Karabulut et al. 2013). We propose that the broad crustal thinning observed beneath the Marmara region originated from this first deformation phase of Aegean N-S extension. However, Figure 5.10 shows that the Moho beneath the Marmara region is not as smooth as beneath the Menderes Massif this may be because of insufficient station coverage in the Marmara region. We observed a significant Moho depth change between two neighbouring stations of the southern shore of the Marmara Sea (Figure 5.10d) in addition rapid and strong variations of the reflectivity factor R are also observed in Figure 5.10e. Moreover, we observe strong variations of the individual RFs with azimuth of the incident wave at stations in the Marmara region, suggesting strong horizontal variations in the crustal structure which are not observed in other parts of the profile (Karabulut et al., 2013). The fact remains that, whether this heterogeneity is an intrinsic characteristic of the crust-mantle boundary in the Marmara area or due to scattering in a very heterogeneous crust due to the superposition of N-S extension with right lateral shear in the broad NAFZ and the later NAF. High V_p/V_s values are observed beneath the Marmara Sea and Thrace Basin (Figure 5.10f). In the same area, Love wave group velocities at 20 s (red curve in Figure 5.10g) are low, while P_n velocities are relatively high (black curve in Figure 5.10g), indicating that the high average V_p/V_s is because of low shear wave velocities in the upper crust due to the presence of thick sedimentary basins (~5km in the Marmara basins and ~7km in the Thrace Basin) and/or pore fluids in highly fractured rocks along the NAF for the Marmara region.

The Menderes Massif exhibits high V_p/V_s values of 1.8 to 1.9 indicative of an intermediate composition as similar as the Marmara Sea and Thrace Basin. The most striking observation is the strong amplitude of the Moho converted phase documented by high (>0.4) and spatially consistent values of R beneath the Southern Menderes Massif (Figure 5.10e). As discussed earlier, the R values mostly reflect the sharpness of the Moho that is the width of the crust–mantle transition (Nair et al. 2006). The high values of R beneath the Southern Menderes Massif suggest a particularly thin Moho transition zone (Karabulut et al. 2013).

On the contrary, the amplitude of the Moho converted phase is significantly weaker in the Lycian Nappes to the south of the Menderes Massif labeled with values of R in the range 0.2–0.3. The most striking observation is a strong converted phase of positive polarity below a negative polarity conversion of similar dip at upper mantle depth of 45–60 km. Although we have lack of stations between Rhodes Island and the Mediterranean coast of Turkey, we strongly believe that the top of subducting African lithosphere is imaged as the negative polarity north dipping boundary underlined by a dot-and dash line in Figure 5.10d. The underlying positive polarity converted phase may correspond to the African Moho. It dips at an angle smaller than 30° from approximately 30 km depth beneath Rhodes Island to ~50 km beneath station YER0 in the Lycian Nappes where it terminates suddenly. Sodoudi et al. (2006) also identified the African Moho in their P wave RFs at station RODO in Rhodes Island, at 46 km depth beneath an Aegean Moho at 25 km. We found more shallower depths, 30 km beneath RODO and 20 km stands for Aegean Moho. The difference comes from the V_p/V_s estimations, they assumed V_p/V_s 1.73 and we measured 1.85 beneath ARG. Lycian Nappes have comparably low R values which may be due to sub-crustal heating above the subduction zone that would reduce the velocity contrast at the Moho. Highest V_p/V_s ratios along the profile reaches to 1.95 at stations close to abundant hydrothermal resources and extremely large values (>2) between stations W20 and YER0 (500–540 km) which are located right above the tip of the subducted African lithosphere. Love wave group velocities at 20 s (red curve in Figure 5.10g) are low where V_p/V_s is high, indicative of low crustal shear wave velocities which are in consistent with a hot crust. Furthermore, P_n velocities (black curve in Figure 5.10g) are low, in agreement with a hot low-velocity mantle wedge above the subduction zone.

Seismicity mostly concentrated within the active fault zones, the NAF, the Izmir–Ankara Suture zone, the Gökova Gulf and the subduction zone (Figure 5.10d). The only departure from the brittle upper crust model is the Gökova Gulf where earthquakes are located down to Moho depth. A possible explanation is partially melted lower crust above the subduction zone. The seismicity has no regular pattern in the subduction zone. The scattered seismicity may be related to poor depth constraints on the hypocentre locations.

5.4.2. Central Anatolia Profile

The profile installed in the transition zone between western and central Anatolia along 30.5° E crossing main structures nearly perpendicularly to their east-west strike (Figure 5.12). 23 stations were installed from the Black Sea coast in the north to the Mediterranean Sea in the south. The number of stations increased to 32 on the profile with an average interstation distance of 15 km (see Appendix A, Table 2) by the use of permanent stations.

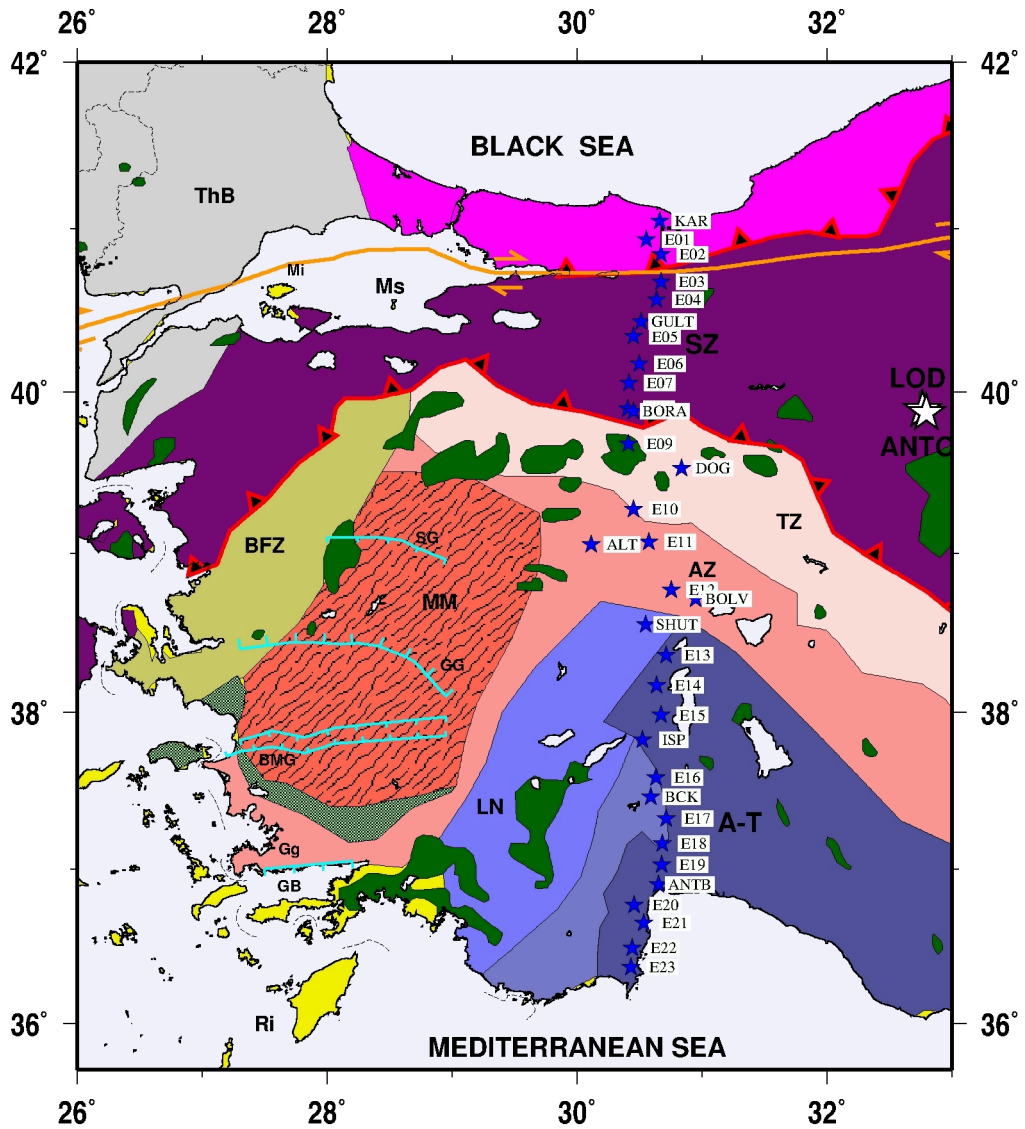


Figure 5.12. Seismic stations of Central Anatolia profile installed during SIMBAAD experiment, blue stars are temporary and white stars are permanent stations. Main tectonic features and morpho-tectonic units are also labeled; ATB, Anatolide-Tauride Block; AZ, Afyon Zone; BFZ, Bornova Flysh Zone; BMG, Büyük Menderes Graben; GG, Gediz Graben; GB: Gökova Bay; Gg, Gökova Graben; SG, Simav Graben; IZ, Istanbul Zone; LN, Lycian Nappes; MM, Menderes Massif; PT, Pontides; RS, Rhodope-Strandja Basin; SZ, Sakarya Zone; IASZ, Izmir-Ankara Suture Zone; Ms, Marmara Sea; Mi, Marmara Island; NAFZ, North Anatolian Fault Zone; Ri, Rhodos Island; ThB, Thrace Basin; TZ, Tavşanlı Zone. Stures are shown by red lines with black triangles on. The main normal faults of the grabens are shown by the thin light blue lines. The magenta line shows the NAF. The ophiolite outcrops labeled with dark green units. Western Anatolia profile

shown as a blue line. Geological map modified from Okay and Tüysüz, 1999, and van Hinsbergen et al, 2010, Karabulut et al., 2013.

The same procedures applied for the WAP, are also applied for the Central Anatolia profile. As discussed earlier CCP requires a accurate knowledge about crustal P wave velocity due to that we calculated P wave velocities from local earthquakes (for further information please see chapter 5.1 and 5.3.1). A modified IASP91 was used as a reference model with a constant P wave velocity of 6.3km/s and variable V_p/V_s beneath each station was constructed. The 2-D model space was divided into two dimensional grid of cells and RFs were back projected with constant ray parameters.

The vertical resolution in this study is in the range 2.5–3 km and the radius of the corresponding Fresnel zone is approximately 10 km at 35 km depth. Using a mesh of 4 km in the horizontal direction and 1.0 km in the vertical direction, we therefore adopted a smoothing window of 15 km horizontally and 2 km vertically. The uncertainties on the Moho depth are estimated from the migrated RF depth sections (Please see chapter 5.4.1 for further information about resolution).

Additionally, to test the accuracy of our estimates we computed the CCP images of the multiples, PpPs and PpSs +PsPs. Moreover they are more sensitive to V_p/V_s than the primary Ps (Heteyni, 2007), so if, the converted phases are in the same depth with the moho the estimates are reliable (Figure 5.13) if not, depth differences can be used to adjust the V_p/V_s ratio.

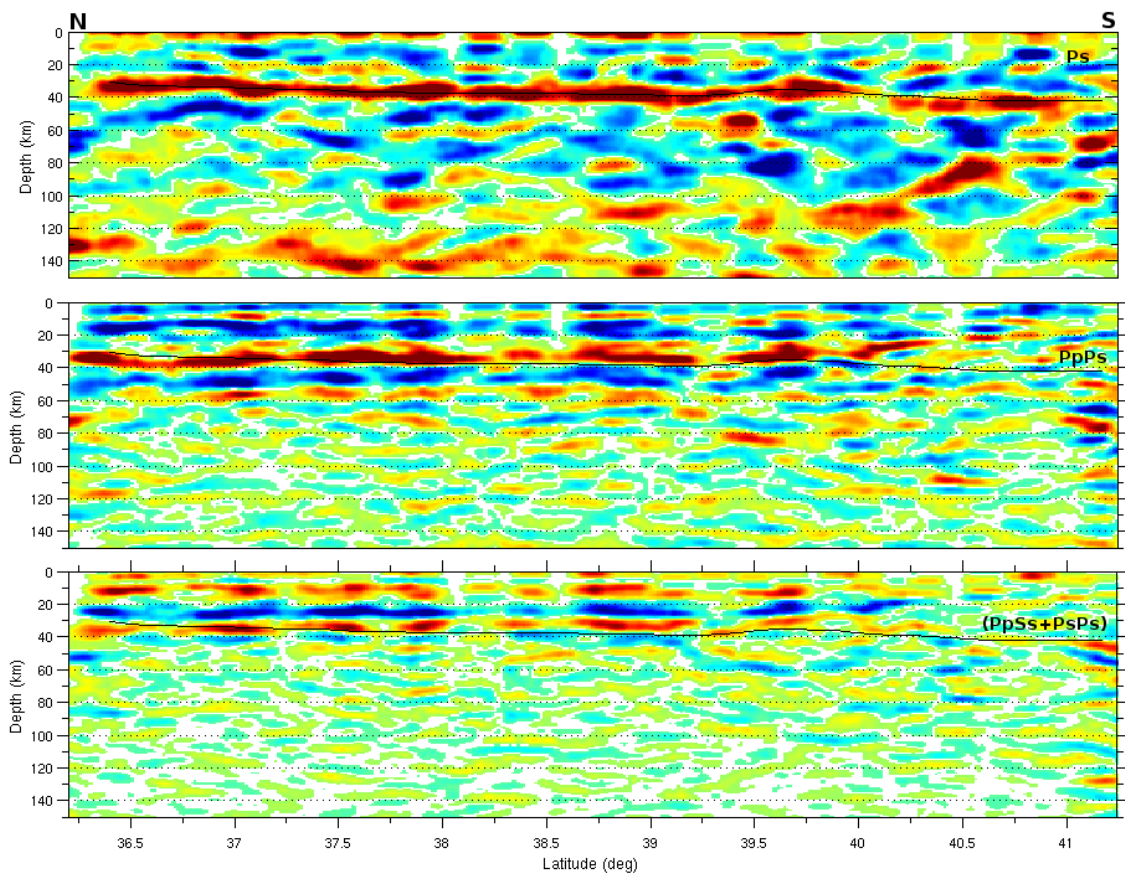


Figure 5.13. Migrated depth sections of Ps (a), PpPs (b) and PpSs+PsPs (c) modes. Moho is labeled with a black line.

The three images indicate consistent results beneath the SZ and AZ while dissimilarities are observed beneath the ATB and southern end. Overall, the strong similarities between the three migrated sections indicate that the V_p/V_s model is accurate and the depth section produced by CCP is reliable.

5.4.2.1. Results. The results of CCP analysis is presented in Figure 5.14 below.

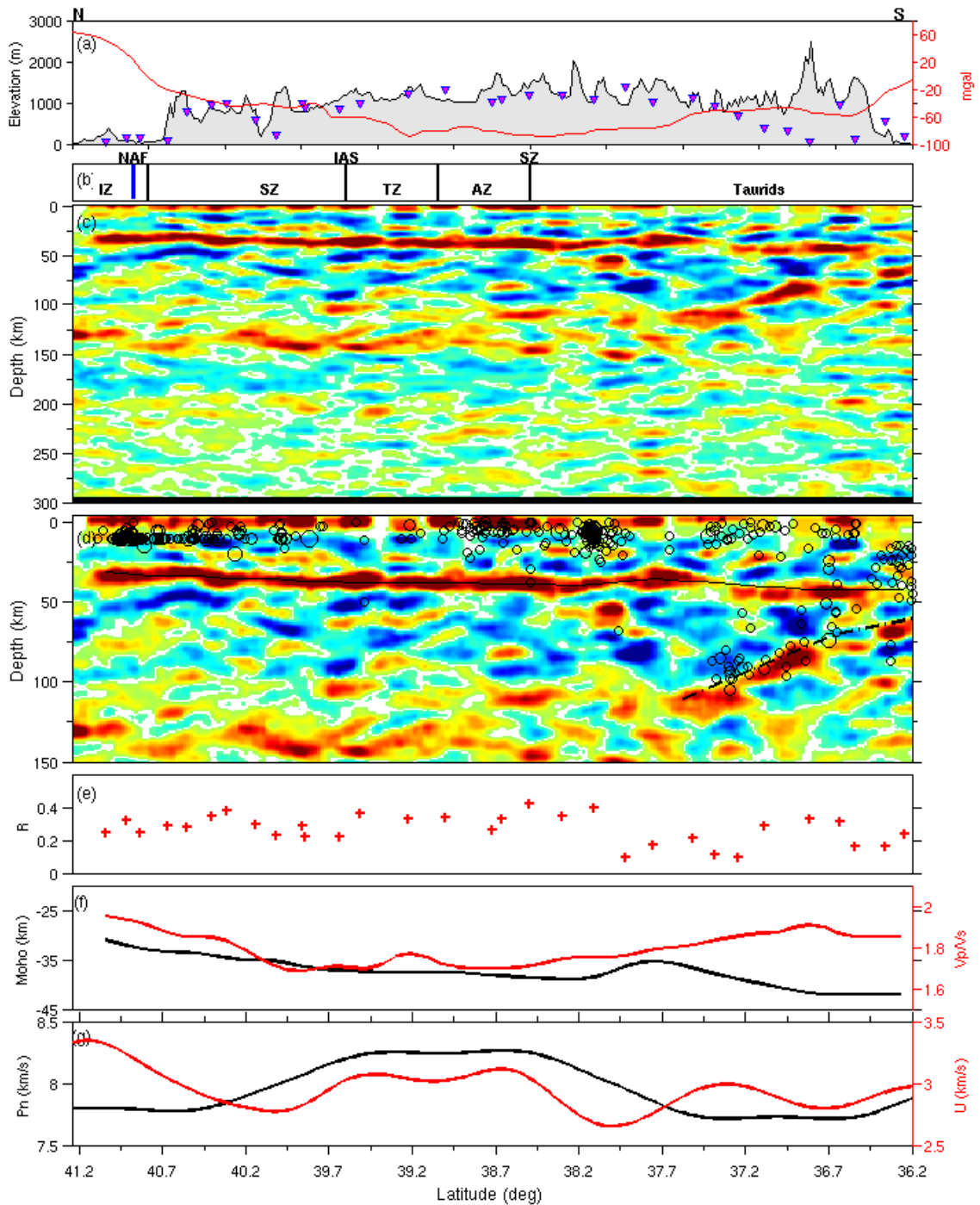


Figure 5.14. Central Anatolia profile CCP results, migrated depth sections. (a) Topography profile (black), receiver locations (magenta) and Bouguer gravity anomaly (red). (b) Geological units along the profile (c) Common-conversion point depth migrated cross-section (no vertical exaggeration). Red represents positive P-to-S converted amplitudes and indicates sharp increase in velocity with depth. (d) Common-conversion point depth migrated cross-section with seismicity and major interpreted structures (vertical

exaggeration 2). The seismic activity covers a period from 1998 to 2012 with magnitudes $M_l > 3.0$. (e) Ratio R of stacking amplitudes for each station. (f) Crustal thickness (black) and V_p/V_s (red) variations. (g) 20 sec Love wave group velocities (red) and P_n velocities (black). Same abbreviations as in Figure 5.12.

Figure 5.14 indicates the results of CCP analysis. The top panel (Figure 5.14a) shows the topography and Bouguer gravity anomaly along the profile (Ateş et al., 1999). The gravity values reach 60 mgal in the Black Sea coast, drops to -80mgal on the Anatolian plateau and rises smoothly to 10mgal towards Antalya Bay. Figure 5.14b indicates locations of the major structural boundaries along the profile. From north to south profile crosses, IZ, SZ, TZ, AZ and nearly half of the stations are deployed in the Anatolide -Tauride block. Figures 5.14c and 5.14d show the CCP time-to-depth migrated section, with no vertical exaggeration (Figure 5.14c) and a vertical exaggeration of 2 (Figure 5.14d). Color of red indicates positive amplitudes that are generated by a velocity increase with depth and blue color corresponds to a velocity decrease by negative amplitude. Hypocenters of local earthquakes located within a band of 20 km along the profile are superimposed on the CCP section in Figure 5.14d. The seismicity along the profile is mostly localised in the upper 15km of the crust. The seismicity concentrates near the NAFZ. It is also interesting to observe a seismic cluster near the Isparta Angle, where Hellenic and Cyprian arcs intersect at a sharp bend, above the depth termination of the imaged subducting plate. Deep seismicity ($>30\text{km}$) on the southern end of the profile along the Cyprus arc is typical of subduction zones with deeper events toward the back-arc region is correlated with the imaged subducting lithosphere and no earthquakes are observed at depths greater than 110km. The bold black line is the conversion on the Moho. Dashed black line shows the subducting Cyprus lithosphere dipping northward with an angle of 40° between ~ 60 and ~ 100 km depths beneath the Antalya Bay at the southern end of the profile.

R -factor shown in Figure 5.14e mostly changes between 0.2-0.4. The amplitude of the Moho converted phase is strong and shows no significant variations between 41.2°N and 38°N but weakens on the south of the Isparta Angle. From the Sakarya Zone to the Anatolide-Tauride block, the crust-mantle boundary is clearly defined by a strong P_s and strong multiples, giving R -values larger than 0.2. Between 38.5°N and 37.5°N , above subduction, both the strength and thickness of reflectivity zone is changing. The highest values of R

(~4.5) are observed at the beginning of Taurids, the crustal thickness reaches its climax beneath Taurids with 43 km. The lowest values of R (~0.1) observed beneath the subducting lithosphere at the Southern end of the profile. The amplitude of the converted phase weakens suddenly at stations of the Mediterranean coast as observed at the Western Anatolia profile.

Figure 5.14f shows the final estimates of crustal thickness (black curve) and Vp/Vs (red curve) from the CCP images which may differ from the initial estimates of the H-k stack given in Appendix A, Table 1. Comprehensively, laterally continuous band of positive amplitude between 34 and 43 km depth is an imprint of Moho (Figures 5.14c and 5.14d). The PpPs multiple appears with laterally discontinuous positive amplitudes in the 110-150 km depth range in Figure 5.14d. Beneath the Istanbul Zone, the Moho depth is ~33 km and gradually increased within the Sakarya zone reaching to ~36km on IASZ. A Moho depth of ~37 km within the Afyon Zone sharply reduced to 35km beneath the Isparta Angle. The crustal thickness attains its maximum value of ~43 km on the southern end of the profile above the subduction zone. The crustal Vp/Vs ratio measured along the array ranges from 1.65 to 2.0 (red curve in Figure 5.14f) with an average of 1.85, slightly above the global average of continental crust (Christensen, 1996). The Vp/Vs is lower (~1.73) in the middle of the profile between 40.0 °N and 37.5 °N indicating mafic composition while higher value on both ends reaching to 1.9.

We also display in Figure 5.14g Love wave group velocities at 20 s (Cambaz and Karabulut, 2010) and Pn velocities along the profile (Mutlu and Karabulut, 2011).

5.4.2.1. Discussion. The segmentation of the subduction in the Eastern Mediterranean into the Hellenic and the Cyprus arcs has major influences on the deformation of the overriding Anatolia plate. The Central Anatolia Plateau appears to be a broad transition between the thin crust of WA and the thicker crust of EA.

The CCP image reveals a smooth Moho geometry when compared to the undulated moho in the WAP. Sharp Moho discontinuity at depths ranging from 32 km beneath the Black Sea coast of the Aegean Sea to 43 km beneath the Antalya Bay. Distinct crustal

sections are identified from the observations of crustal thickness, intracrustal discontinuities and V_p/V_s . The Moho depth smoothly increasing from ~32 km in the Black Sea coast to ~35 km beneath the Sakarya Zone with mafic composition, the central Anatolia is ~37km thick and exhibits intracrustal discontinuities with felsic composition, the southern section with thickness increasing from ~35 km near Isparta angle to 43km in the Antalya bay with high V_p/V_s can be associated with recent volcanism in central anatolia (Vanacore et. al., 2013).

The amplitude of the Moho converted phase is strong and shows no significant variations between 41.2°N and 38°N but weakens on the south of the Isparta Angle. Between 38.5°N and 37.5°N both the strength and thickness of reflectivity zone is changing. A small localised positive anomaly appears beneath the Moho (~50km) at 38.2°N. The mantle wedge above the subducting plate is characterised by a large negative anomaly. The multiples between 110-150 km appear as laterally continuous feature on the CCP section.

We observe laterally continuous midcrustal conversions along the profile between 15-20km depths. The midcrustal arrivals define nearly a coherent horizontal layer from the Black Sea coast to the Isparta angle. However, the midcrustal conversions above the subduction zone appears to be tilted sub-horizontally parallel to the subducting plate. The continuity is interrupted at places with larger station spacing or poor data quality. However the qualitative evaluation of the RF at each station indicates the presence of the midcrustal arrivals.

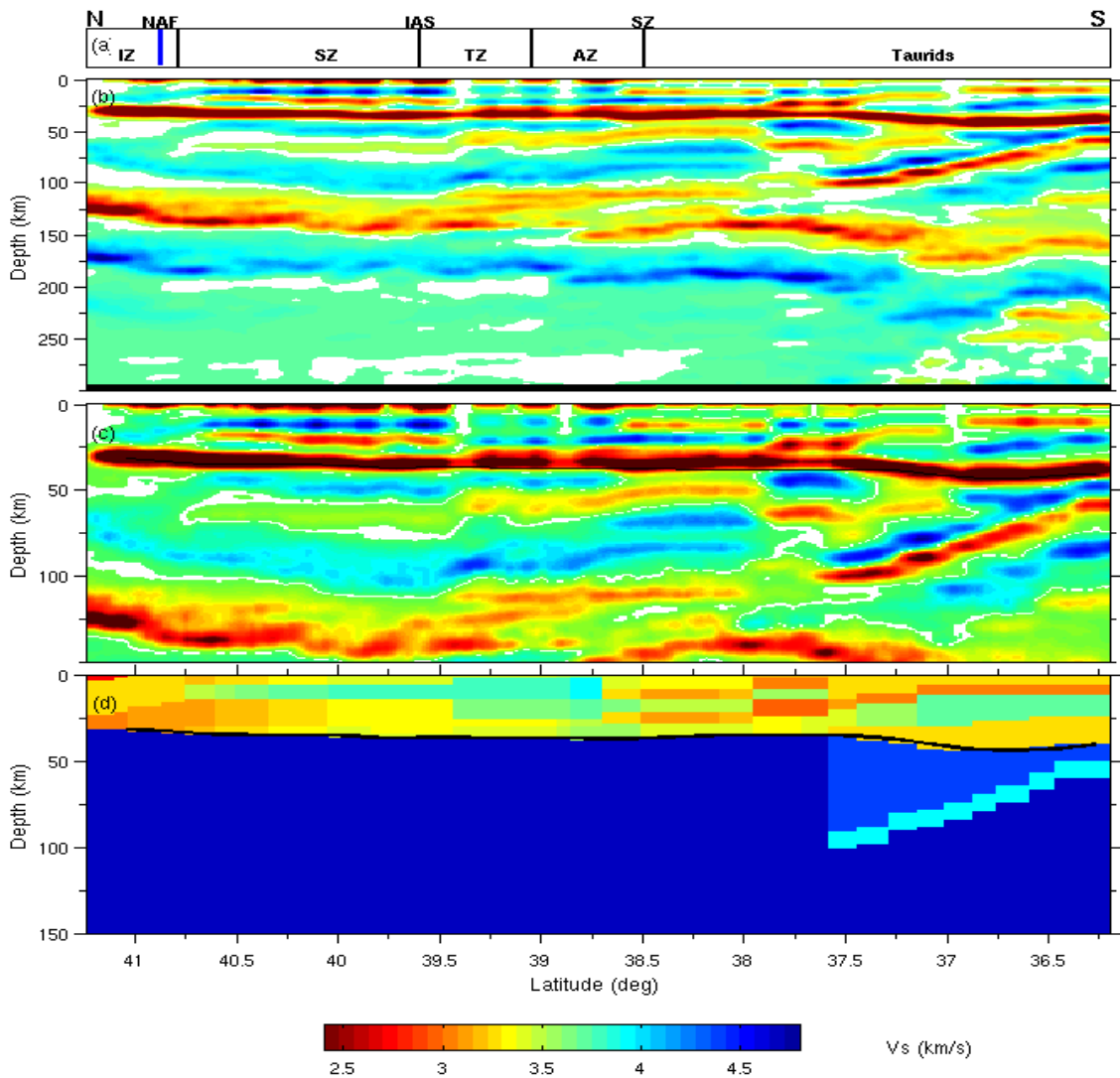


Figure 5.15. (a) Synthetic CCP migrated depth section computed from the crustal thickness and V_p/V_s models estimated in this study (Appendix A Table 2). (b) Synthetic CCP migrated depth section zoomed for the upper part of model response; (c) Model geometry and V_p/V_s used for the synthetic CCP depth section. Layer parameters for the subducting plate; $V_p=6.7\text{km/s}$, $H=15\text{km}$;

Synthetic CCP section was computed (Figure 5.15) from the crustal thicknesses and V_p/V_s ratios obtained from the receiver-function analysis to see the reliability of the crustal model obtained from the CCP analysis and verify the horizontally layered weak midcrustal conversions at 15-20 km and mantle wedge above the subducting plate with negative anomaly. Same source-station geometry with the observed data were used to compute the synthetic RFs and same V_p , V_p/V_s and crustal thickness models (Appendix A, Table 2) used

for the observed RFs were used in migration while performing CCP technique. Although, the thickness and velocity of the shallow layers are poorly known trial-and-error modelling successfully leads to a synthetic depth section similar to the observed section (Figure 5.14c). Minor differences are observed above the Isparta ange due to the assumptions we made, like a constant V_p/V_s ratio for the whole crust. However, the converted energy, observed as a pile of positive (red), negative (blue) and positive polarity, laterally located in the upper, middle and lower crust along nearly the whole profile well fits with the observations (Figure 5.14). The converted energy beneath the Tavşanlı Zone is not well correlated due to the broad station spacings and lack of data (Figure 5.14). In addition, subduction area and the negative polarity conversions on and under the slab beneath the Taurids are correlated with the observations. On the other we could not identify the main geological features like the NAF or the Izmir–Ankara suture which could have induced velocity discrepancy inside the crust.

The average Moho depth along the profile is ~ 37 km, beneath Isparta Angle at $\sim 38.5^\circ\text{N}$, Moho is shallower with 35 km. Vanacora et al. (2013) determined the Moho depth as 34 km under the ISP station with a 1.8 V_p/V_s ratio, they also found 38 km Moho depth beneath LOD station while ours is 37 km, 34 km beneath BCK station while ours is 35 km which are consistent with our estimates. The crust-mantle boundary has a complicated shape on the south of the Isparta angle where a local thinning is followed by a steep increase. The crustal thickness attains its maximum value of ~ 42 km at the southern end of the profile above the subduction zone beneath ANTB station with a 1.83 V_p/V_s ratio where African and Eurasian plates melt. Tezel et al. (2011) found 40 km as a Moho depth with $V_s = 4$ km/s in the Antalya Bay, lower than the global average due to molten or hot upper mantle material. On the central part of the profile the Moho depth is between 37-39 km which is also coherent with Çakır and Erduran (2011). They claimed 38 km Moho depth in the central Anatolia. The teleseismic P-wave tomography by Biryol et al. (2011) find fast wave speed anomalies beneath Anatolia which is compatible with our high V_p/V_s ratios which can be associated with the hot ascending Asthenosphere. In the same manner surface wave tomography of Salaun et al. (2012) shows an overall low-velocity zone (80–200 km depth) beneath Anatolia indicating warm asthenosphere underlying a thin lithosphere. The Moho depth map computed by Hubans (2010) from ambient noise tomography shows a gradual increase of

Moho depth from the western Anatolia to the central Anatolia which is clearly observed in our study when the WAP and CAP compared.

Seismicity along the profile well fits with the character of a relatively ‘non deforming’ Central Anatolia in regard to its surroundings. Mostly seismicity is located in the upper 20 km as expected. Deep seismicity (>30km) on the southern end of the profile along the Cyprus arc is typical of subduction zones with deeper events toward the back-arc region is correlated with the imaged subducting lithosphere and no earthquakes are observed at depths greater than 110 km.

6. CONCLUSIONS

This study is an attempt to contribute to the understanding of long-term debated questions on continental deformation in the Western Anatolia Aegean province by the help of high resolution lithospheric images along western and central Turkey and permanent broadband stations. Determination of reliable Moho depth maps and V_p/V_s ratios lead us to put better constraints on the African lithospheric structure beneath western Turkey and Aegean region.

In continental extension provinces, main feature is crustal thinning. Due to the N-S extension in western Turkey, the average crustal thickness measured along WAP is low with 27 km. Crustal thinning is not uniform in N-S direction along the WAP. Significantly thinned the crust to 25 km beneath the Sea of Marmara and the MM and 20 km beneath the Mediterranean coast. The Moho below the MM is relatively flat and continuous where topography wiped out by hot ductile flow on the lower crust smoothing out the rapid changes in crustal thickness.

Moho of the western Anatolia is not flat at regional scale when compared to Basin and Range type extensional province. It displays long-wavelength undulations with depth differences of 6–7 km in 150-km horizontal distance from the two Moho highs of the Marmara and the Menderes to the Moho low beneath the Izmir–Ankara suture zone. Although, we concluded on the absence of intracrustal interfaces due to all signals observed at mid or lower crustal depths in the migrated section are artefacts, the heterogeneity of the Marmara crust evidenced by strong changes of RF waveforms with backazimuth and a strong Bouguer anomaly. Average V_p/V_s ratio measured along the profile is 1.78, slightly above the global average of continental crustal value. Low V_p/V_s observed in the Marmara region due to low shear wave velocities in the upper crust due to the presence of thick sedimentary basins and/or pore fluids in highly fractured rocks along the NAF for the Marmara region.

African lithosphere imaged at the southern end of the WAP. It dips at an angle smaller than 30° from approximately 30 km depth beneath Rhodos Island to ~ 50 km beneath station YER in the Lycian Nappes where it terminates abruptly. High V_p/V_s ratio right above the northernmost tip of the African Moho due to low shear wave velocities could be indicative

of a hot crust. The abrupt termination of the subducted lithosphere confirms the presence of a slab tear beneath southwest Anatolia, as suggested by body wave tomography (Spakman et al. 1993) and surface wave tomography (Salaün et al., 2012).

Comperatively undeforming central Anatolia, is the westernmost part of the Iranian-Anatolian high plateau at an average elevation of 1.5-2 km. The average crustal thickness is 36 km on the CAP. As expected Moho depths are increasing from west to east as the topography smoothes from long wavelength undulations to a more flat moho. CAP displays a smooth Moho topography at regional scale when compared to WA. The absence or very thin mantle lid beneath Anatolia results in a low strength, hot lower crust and uppermost mantle, in contrast with the colder and stronger lithospheres of the Taurides. Viscous flow in the lower crust wipes out any lateral changes in the crustal structure (thickness and internal structure) expected from such a heterogeneous collage of continental fragments.

The Moho depth smoothly increasing from ~32 km in the Black Sea coast to ~35 km beneath the Sakarya Zone with mafic composition, the central Anatolia is ~37km thick and exhibits intracrustal discontinuities with felsic composition, the southern section with thickness increasing from ~35 km near Isparta angle to 43km in the Antalya bay where African and Eurisian plates melt. Deeper seismic activity observed beneath Antalya bay due to the upwelling of hot asthenospheric material.

Likewise, slightly high V_p/V_s ratios ~1.8 observed in the central Anatolia can be associated with the recent volcanism.

The subducted Cyprus lithosphere is clearly imprinted on the southernmost end of the CAP transect beneath Antalya Bay. Dipping northward with an angle of 40° between ~50 and ~100 km depths. In the western Cyprus and Hellenic arcs, the distribution of earthquake hypocentres outlines a Wadati–Benioff zone at 90–120 km. The Cyprus arc has lower seismicity rate than the Hellenic arc.

REFERENCES

Ateş, A., P. Kearey, and S. Tufan, “New gravity and magnetic anomaly maps of Turkey”, *Geophys. J. Int.*, 136, pp. 499–502, 1999.

Aktuğ, B., J. M. Nocquet, A. Cingöz, B. Parsons, Y. Erkan, P. England, O. Lenk, M. A. Gürdal, A. Kılıçoğlu, H. Akdeniz, and A. Tekgül, “Deformation of western Turkey from a combination of permanent and campaign GPS data: limits to block-like behavior”, *J. Geophys. Res.*, 114, B10404, 2009.

Barka, A. A., and K. Kadinsky-Cade, “Strike-slip fault geometry in Turkey and its influence on earthquake activity”, *Tectonics*, 7, pp. 663-684, 1988.

Barka A. A., and R. Reilinger, “Active tectonics of the Mediterranean region: deduced from GPS, neotectonic and seismicity data”, *Annale de Geofisica*, XL, pp. 587-610, 1997.

Barka, A. A., and L. Gülen, “New constraints on age and total offset of the North Anatolian Fault Zone: implications for tectonics of the eastern Mediterranean region”, *Middle East Tech. Univ. J. Pure Appl Sci.*, 31, pp. 39-63, 1988.

Barka, A. A., “The North Anatolian Fault Zone”, *Annales Tectonicae*, 6, pp. 164-195, 1992.

Bécel, A., M. Laigle, B. de Voogdb, A. Hirna, T. Taymaz, A. Galvéa, H. Shimamurad, Y. Muraid, J. Lépine, M. Sapina, and S. Özalaybey, “Moho, crustal architecture and deep deformation under the North Marmara Trough, from the SEISMARMARA Leg 1 offshore–onshore reflection–refraction survey”, *Tectonophysics*, 467, pp. 1-21, 2009.

Block, L. and L. H. Royden, “Core complex geometries and regional scale flow in the lower crust”, *Tectonics*, 9, pp. 557-567, 1990.

Boray, A., F. Saroglu, and O. Emre, “Isparta bolumunun Kuzey Kesminde D-B Daralma icin bazi veriler”, *Jeoloji Mühendisligi*, 23, pp. 9–20, 1985.

Bozkurt, E., and R. Oberhänsli, “Menderes Massif (Western Turkey): structural, metamorphic and magmatic evolution a synthesis”, *Int. J. Earth Sci.*, 89, pp. 679–708, 2001.

Cambaz, M. D., and H. Karabulut, “Love wave group velocity maps of Turkey and surrounding regions”, *Geophys. J. Int.*, 181, pp. 502–520, 2010.

Cosentino, D., T. F. Schildgen, P. Cipollari, C. Faranda, C. Gliozzi, E. Hudáčková, S. Lucifora, and M. Strecker, “Late Miocene surface uplift of the southern margin of the central Anatolian Plateau, Central Taurides, Turkey”, *Geological Society of America Bulletin*, 124, pp. 133–145, 2012.

Çemen, İ., “Extensional tectonics in the Basin and Range, the Aegean, and Western Anatolia: Introduction”, *Tectonophysics*, 488, pp. 1-6, 2010.

Çakır O., and M. Erduran, “On the P and S receiver functions used for inverting the one-dimensional Upper Mantle shear-wave velocities”, *Surv Geophys*, 32, pp. 71-98, 2011.

Christensen, N.I., “Poisson’s ratio and crustal seismology”, *J. Geophys. Res.*, 101, B2, pp. 3139-3156, 1996.

Chu, D., *The globec kriging software package easykrig 2.1, Technical report*, Woods Hole Oceanographic Institution, 2000.

Dilek, Y., “Collision tectonics of the Mediterranean region: Causes and consequences”, *Geological Society of America Special Paper*, 409, pp. 1-13, 2006.

Dilek, Y., and E. A. Sandvol, “Seismic structure, crustal architecture and tectonic evolution of the Anatolian-African Plate Boundary and the Cenozoic Orogenic Belts in the Eastern Mediterranean Region”, *J. Geol. Soc. London, Special Publications*, 327, pp. 127 – 160, 2009.

England, P. C., and D. P. McKenzie, A thin viscous sheet model for continental deformation, *Geophys. J. R. Astr. Soc.*, 70, pp. 295–321, 1982.

Erdoğan, B., “Tectonic relations between İzmir-Ankara Zone and Karaburun belt”, *Bulletin of the Mineral Research and Exploration of Turkey*, 110, pp. 1-15, 1990.

Eyidoğan, H., and J. A. Jackson, “Seismological study of normal faulting in the Demirci, Alaşehir and Gediz earthquakes of 1969-70 in western Turkey: implication for the nature and geometry of deformation in the continental crust”, *Geophys. Journal of Royal Astronomical Society*, 81, pp. 569-607, 1985.

Fountain, D. M., and N. I. Christensen, “Composition of the continental crust and upper mantle; a review”, *Geol. Soc. Am. Mem.*, 172, pp. 711– 742, 1989.

Faccenna, C., O. Bellier, J. Martinod, C. Piromallo, and V. Regard, “Slab detachment beneath eastern Anatolia: a possible cause for the formation of the North Anatolian fault”, *Earth Planet Sc Lett*, 242, pp. 85 – 97, 2006.

Faccenna, C. and T. Becker, “Shaping mobile belts by small-scale convection”, *Nature*, 465, pp. 602 – 605, 2010.

Faccenna, C., T. Becker, L. Jolivet, and M. Keskin, “Mantle convection in the Middle East: Reconciling Afar upwelling, Arabia indentation and Aegean trench rollback”, *Earth Planet Sc Lett*, 375, pp. 254 – 269, 2013.

Floyd, M.A., H. Billiris, D. Paradissis, G. Veis, A. Avallone, P. Briole, S. McClusky, J. M. Nocquet, K. Palamartchouk, B. Parsons, and P. C. England, “A new velocity field for Greece: implications for the kinematics and dynamics of the Aegean”, *Journal of Geophysical Research*, 115, B10403, 2010.

Gallagher, K., and M. Sambridge, “Genetic algorithms: a powerful tool for large-scale non-linear optimization problems Comput”, *Geoscience*, 20(7/8), pp. 1229–1236, 1994.

Görür, N. And A. I. Okay, “A fore-arc origin for the Thrace Basin, NW Turkey”, *Geol. Rundsch.*, 85, pp. 662–668, 1996.

Gurnis, M., “Bounds on global dynamic topography from Phanerozoic flooding of continental platforms”, *Nature*, 344, pp. 754–766, 1990.

Hammersley, J. M. and D. C. Handscomb, *Monte Carlo Methods*, Chapman & Hall, London, 1964.

Hauser, E., C. Potter, T. Hauge, S. Burgess, S. Burtch, J. Mutschler, R. Allmendinger, L. Brown, S. Kaufman, and J. Oliver, “Crustal structure of eastern Nevada from COCORP deep seismic reflection data”, *Bull. Geol. Soc. Am.*, 99, pp. 833–844, 1987.

Holland, J. H., *Adaptation in Natural and Artificial Systems*, Ann Arbor, University of Michigan Press, 1975.

Hubans, F., *Utilisation des corrélations de bruit micro-sismique pour l’analyse des propriétés du champ d’onde et l’imagerie crustale*, Ph. D. Thesis, Grenoble University, 2010.

Jackson, J., “Active tectonics of the Aegean region”, *Annual Review of Earth and Planetary Sciences*, 22, pp. 239–271, 1994.

Jolivet, L., J. P. Brun, S. Gautier, S. Lellemand, and M. Patriat, “3D kinematics of extension in the Aegean from the early Miocene to the present: insight from the ductile crust”, *Bulletin de la Societe Geologique de France*, Vol. 165, pp. 195–209, 1994.

Jolivet, L. and C. Faccenna, “Mediterranean extension and the Africa-Eurasia collision”, *Tectonics*, 19, pp. 1095-1106, 2000.

Jolivet, L., C. Faccenna, B. Goes, E. Burov, and P. Agard, “Subduction tectonics and exhumation of high-pressure metamorphic rocks in the Mediterranean orogens”, *Am J Sci*, 303, pp. 353-409, 2003.

Jolivet, L., C. Faccenna, B. Huet, L. Labrousse, L. Le Pourhiet, O. Lacombe, E. Lecomte, E. Burov, Y. Denèle, J. Brun, M. Philippon, A. Paul, G. Salaun, H. Karabulut, C. Piromallo, P. Monie, F. Gueydan, A. I. Okay, R. Oberhansli, A. Pourteau, R. Augier, L. Gadenne, and O. Driussi, “Aegean tectonics: strain localisation, slab tearing and trench retreat”. *Tectonophysics*, 597–598, pp. 1–33. 2013.

Kind, R., T. Eken, F. Tilmann, F. Sodoudi, T. Taymaz, F. Bulut, X. Yuan, B. Can, and F. Schneider, “Thickness of the lithosphere beneath Turkey and surroundings from S-receiver functions”, *Solid Earth*, 6, pp. 971 – 984, 2015.

Kim, Hyun-seung., *Mapping Crustal Structure of the Nechako Basin using Teleseismic Receiver Functions*, B.S. Thesis, University of Washington, 2007.

Kirkpatrick, S. C., D. Gelatt, and M. P. Vecchi, “Optimization by simulated annealing”, *Science*, 220, pp. 671–680, 1983.

Kiratzi, A. and E. Louvari, “Focal mechanisms of shallow earthquakes in the Aegean Sea and the surrounding lands determined by waveform modeling: a new database”, *J. Geodyn.*, 36, pp. 251–274, 2003.

Klemperer, S. L., T. A. Hauge, E. C. Hauser, J. E. Oliver, and C. J. Potter, “The Moho in the northern Basin and Range province, Nevada, along the COCORP 40°N seismic-reflection transect”, *Bull. geol. Soc. Am.*, 97, pp. 603– 618, 1986.

Koulakov, I. and S. V. Sobolev, “Moho depth and three-dimensional P and S structure of the crust and uppermost mantle in the Eastern Mediterranean and Middle East derived from tomographic inversion of local ISC data”, *Geophysical Journal International*, 164, 1, pp. 218-235, 2006.

Langston, C.A., “The effect of planar dipping structure on source and receiver responses for constant ray parameter”, *Bull. Seismol. Soc. Am.*, 67, pp. 1029-1050, 1977.

Le Pichon, X. and C. Kreemer, “The Miocene to Present kinematic evolution of the eastern Mediterranean and Middle East and its implications for dynamics”, *Ann. Rev. Earth planet. Sci.*, 38, pp. 323–351, 2010.

Le Pichon, X., A. M. C. Sengor, E. Demirbağ, C. Rangin, C. İmren, A. Armijo, N. Gorur, N. Cagatay, B. Mercier de Lepinay, B. Meyer, R. Saatçılar, and B. Tok, “The active Main Marmara Fault”, *Earth and Planetary Science Letters*, 192, pp. 595-616, 2001.

Ligorria, J. P. and C. J. Ammon, “Iterative deconvolution and receiver-function estimation”, *Bull. Seismol. Soc. Am*, 89, pp. 1395–1400, 1999.

Li, X., A. G. Bock, R. Vafidis, H. P. Kind, W. Harjes, K. Hanka, M. Wylegalla, V. D. Meijde, and X. Yuan, “Receiver function study of the Hellenic subduction zone: Imaging crustal thickness variations and the oceanic Moho of the descending African lithosphere”, *Geophys. J. Int.*, Vol. 155, pp. 733– 748, 2003.

Liu, Q.Y., R. D. Van Der Hilst, Y. Li, H. J. Yao, J. H. Chen, B. Guo, S. H. Qi, J. Wang, H. Huang, and S. C. Li, “Eastward expansion of the Tibetan Plateau by crustal flow and strain partitioning across faults”. *Nature Geoscience*, 7, pp. 361 – 365, 2014.

Maggi, A., J. A. Jackson, D. P. McKenzie, and K. Priestley, “Earthquake focal depths, effective elastic thickness, and the strength of the continental lithosphere”, *Geology*, 28, pp. 495-498, 2000.

Makris, J., “The crust and upper mantle of the Aegean region from deep seismic sounding”, *Tectonophysics*, 46, pp. 269–284, 1978.

Moix, P., L. Beccaletto, H. W. Kozur, C. Hochard, F. Rosselet, G. M. Stampfli, “A new classification of the Turkish terranes and sutures and its implication for the paleotectonic history of the region”. *Tectonophysics*, 451, pp. 7–39, 2008.

McClusky, S., S. Balassanian, A. A. Barka, C. Demir, S. Ergintav, I. Georgiev, O. Gurkan, M. Hamburger, K. Hurst, H. Kahle, K. Kastens, G. Kekelidze, R. King, V. Kotzev, O. Lenk, S. Mahmoud, A. Mishin, M. Nadariya, A. Ouzonis, D. Paradissis, Y. Peter, M.

Prilepin, R. Reilinger, I. Şanlı, H. Seeger, A. Tealeb, M. N. Toksöz, and G. Veis, “Global Positioning System constraints on plate kinematics and dynamics in the eastern Mediterranean and Caucasus”, *Journal of Geophysical Research*, 105, pp. 5695–5720, 2000.

McClusky, S., R. Reilinger, S. Mahmoud, D. Ben Sari, D. and A. Tealeb, “GPS constraints on Africa (Nubia) and Arabia plate motions”, *Geophys. J. Int.*, 155, pp. 126–138, 2003.

McKenzie, D.P., “Plate tectonics of the Mediterranean region”, *Nature*, 226, pp. 239–243, 1970.

McKenzie, D.P., “Active tectonics in the Mediterranean region”, *Geophys. J. R. Astron. Soc.*, 30, pp. 109–185, 1972.

McKenzie, D.P., “Active tectonics of the Alpine-Himalayan belt: The Aegean Sea and surrounding regions”, *Geophys. J. R. Astron. Soc.*, 55, pp. 217–254, 1978.

McKenzie, D.P., F. Nimmo, J. A. Jackson, P. B. Gans, and E. L. Miller, “Characteristics and consequences of flow in the lower crust”, *J. Geophys. Res.*, 105, pp. 11,029– 11,046, 2000.

Mutlu, A.K., H. Karabulut, “Anisotropic Pn tomography of Turkey and adjacent regions”, *Geophysical Journal International*, 187, pp. 1743–1758, 2011.

Nair, K.S., S. G. Gao, K. H. Liu, and P. G. Silver, “Southern African crustal evolution and composition: constraints from receiver function studies”, *J. geophys. Res.*, 111, B02304, 2006.

Nyst, M., and T. Thatcher, “New constraints on the active tectonic deformation of the Aegean”, *J. geophys. Res.*, Vol. 109, B11406, 2004.

Oberhänsli, R., J. Partzsch, O. Candan, and M. Çetinkaplan, “First occurrence of Fe–Mg-carpholite documenting a high-pressure metamorphism in meta sediments of the Lycian Nappes, SW Turkey”, *International Journal of Earth Sciences*, 89, pp. 867–873. 2001.

Okay, A.I., “Distribution and characteristics of the north-west Turkish blueschists”, *The Geological Evolution of the Eastern Mediterranean Special Publications*, Geological Society, London, pp. 455–466, 1984.

Okay, A.I. and O. Tüysüz, “Tethyan Sutures of Northern Turkey the Mediterranean Basins: tertiary extension within the Alpine Orogen”, *Geological Society*, 156, pp. 475-515, 1999.

Okay, A.I., “Jadeite-chloritoid-glaucophane-lawsonite blueschists in northwest Turkey: unusually high P/T ratios in continental crust”, *Journal of Metamorphic Geology*, 20 (8), pp. 757–768, 2002.

Okay, A.I., and M. Satir, “Coeval plutonism and magmatism in a latest Oligocene metamorphic core complex in Northwest Turkey”, *Geological Magazine* 137 (5), pp. 495–516, 2000.

Okay, A.I., “Geology of Turkey: A synopsis”, *Anschnitt*, 21, pp. 19-42, 2008.

Owens, T.J., G. Zandt, and S. R. Taylor, “Seismic evidence for ancient rift beneath the Cumberland plateau, Tennessee: A detailed analysis of broadband teleseismic P waveforms”, *J. Geophys. Res.*, 89, pp. 7783-7795, 1984.

Özeren, S.M. and W. E. Holt, “The dynamics of the eastern Mediterranean and eastern Turkey”, *Geophys J. Int.*, 183, pp. 1165 – 1184, 2010.

Papazachos, B. C., and A. Kiratzi, “A detailed study of the active crustal deformation in the Aegean and surrounding area”, *Tectonophysics*, Vol. 253, pp. 129-153, 1996.

Papazachos, B. C., V. G. Karakostas, C. B. Papazachos, and E. M. Scordilis, “The geometry of the Wadati-Benioff zone and lithospheric kinematics in the Hellenic arc”, *Tectonophysics*, Vol. 319, pp. 275–300, 2000.

Pasyanos, M. E., W. R. Walter, and S. E. Hazler, “A surface wave dispersion study of the Middle East and North Africa for monitoring the Comprehensive Nuclear-Test-Ban Treaty”, *Pure Appl. Geophys.*, 158, pp. 1445–1474, 2001.

Pourteau, A., R. Oberhänsli, O. Candan, E. Barrier, and B. Vrielynck, “Neotethyan Closure History of Western Anatolia: A Geodynamic Discussion”, *International Journal of Earth Sciences*, 105, pp. 23-24, 2016.

Price, S. and B. Scott, “Fault block rotations at the edge of a zone of continental extension: southwest Turkey”, *J. Struct. Geol.*, 16, pp. 381–392, 1994.

Reilinger, R., S. McClusky, M. B. Oral, W. King, and M. N. Toksöz, “Global Positioning System measurements of present-day crustal movements in the Arabia–Africa–Eurasia plate collision zone”, *J. Geophys. Res.*, 102, pp. 9983–9999, 1997.

Reilinger, R., S. McClusky, D. Paradissis, S. Ergintav, and P. Vernant, “Geodetic constraints on the tectonic evolution of the Aegean region and strain accumulation along the Hellenic subduction zone”, *Tectonophysics*, 488, pp. 22–30, 2010.

Reilinger, R., S. McClusky, P. Vernant, S. Lawrence, S. Ergintav, R. Çakmak, H. Özener, F. Kadirov, I. Guliev, R. Stepanyan, M. Nadariya, G. Hahubia, S. Mahmoud, K. Sakr, A. ArRajehi, D. Paradissis, A. Al-Aydrus, M. Prilepin, T. Guseva, E. Evren, A. Dmitrotsa, S. V. Filikov, F. Gomez, R. Al-Ghazzi, and G. Karam, “GPS constraints on continental deformation in the Africa–Arabia–Eurasia continental collision zone and implications for the dynamics of plate interactions”, *J. Geophys. Res.*, 111, B004051, 2006.

Robertson, A.H.F., A. Poisson and Ö. Akıncı, “Developments in research concerning Mesozoic-Tertiary Tethys and Neotectonics in the Isparta Angle, SW Turkey”, *Geol. J.*, 38(3–4), pp. 195–234, 2003.

Robertson, A.H. F., O. Parlak, and T. Ustaömer, “Melange genesis and ophiolite emplacement related to subduction of the northern margin of the Tauride–Anatolide continent, central and western Turkey, in Collision and Collapse at the Africa–Arabia–Eurasia Subduction Zone”, *Geological Society of London*, Special Publication no. 311, pp. 9–66, 2009.

Roumelioti, Z., A. Kiratzi, and C. Benetatos, “Time-Domain Moment Tensors for shallow ($h \leq 40$ km) earthquakes in the broader Aegean Sea for the years 2006 and 2007: The database of the Aristotle University of Thessaloniki”, *Journal of Geodynamics*, 51, pp. 179–189, 2011.

Saunders, P., K. Priestley, and T. Taymaz, “Variation in the crustal structure beneath western Turkey”, *Geophys. J. Int.*, 134, pp. 373–389, 1998.

Salaün, G., H. A. Pedersen, A. Paul, V. Farra, H. Karabulut, D. Hatzfeld, C. Papazachos, D. M. Childs, C. Pequegnat, and SIMBAAD Team, “High-resolution surface wave- tomography of the Aegean-Anatolia region: constraints on upper mantle structure”, *Geophys. J. Int.*, 190, pp. 406–420, 2012.

Sen M., and P. L. Stoffa, “Global Optimization Methods in Geophysical Inversion”, *Advances in Exploration Geophysics* Vol. 4, Elsevier, Amsterdam, 1995.

Sodoudi, F., R. Kind, D. Hatzfeld, K. Priestley, W. Hanka, K. Wylegalla, G. Stavrakakis, A. Vafidis, H. P. Harjes, and M. Bohnhoff, “Lithospheric Structure of the Aegean Obtained from P and S Receiver Functions”, *J. Geophys. Res.*, Vol. 111, B12307, 2006.

Starostenko, V., V. Buryanov, I. Makarenko, O. Rusakov, R. Stephenson, A. Nikishin, G. Georgiev, M. Gerasimov, R. Dimitriu, O. Legostaeva, V. Pehelarov, and C. Sava, “Topography of the crust-mantle boundary beneath the Black Sea Basin”, *Tectonophysics*, 381, pp. 211–233, 2004.

Stoffa, P. L., and M. K. Sen, “Nonlinear multiparameter optimization using genetic algorithms: Inversion of plane wave seismograms”, *Geophysics*, 56, pp. 1794–1810, 1991.

Şengör, A.M.C., “Mid-Mesozoic closure of Permo - Triassic: Tethys and its implications”, *Nature*, 279, pp. 590 -593, 1979.

Şengör, A. M. C. and Y. Yılmaz, “Tethyan evolution of Turkey: a plate tectonic approach”, *Tectonophysics*, 75, pp. 181–241, 1981.

Sengör, A.M.C., M. Satir, and R. Akkök, “Timing of tectonic events in the Menderes Massif, western Turkey: implications for tectonic evolution and evidence for Pan-African basement in Turkey”, *Tectonics*, 3, pp. 693–707, 1984.

Şengör, A. M. C., N. Görür, F. Saroğlu, “Strike-slip faulting and related basin formation in zones of tectonic escape: Turkey as a case study”, In: Biddle, K. T., and Christie-Blick, N. (eds), *Strike-slip Faulting and Basin Formation, Soc. Econ. Paleont. Miner. Spec. Publ.*, Vol. 37, pp. 227-264, 1985.

Şengör, A.M.C., O. Tüysüz, C. İmren, M. Sakınç, H. Eyidoğan, N. Görür, X. Le Pichon, X. and C. Rangin, “The North Anatolian fault: a new look”, *Ann. Rev. Earth Planet. Sci.*, 33, pp. 1–75, 2004.

Schildgen, T. F., C. Yıldırım, D. Cosentino, and M. R. Strecker, “Linking slab break-off, Hellenic trench retreat, and uplift of the Central and Eastern Anatolian plateaus”, *Earth-Science Reviews*, 128, pp. 147–168, 2014.

Tapponnier, P., G. Peltzer, A. Y. L. Dain, R. Armijo, and P. Cobbold, “Propagating extrusion tectonics in Asia: new insights from simple experiments with plasticine”, *Geology*, 10, pp. 611–616, 1982.

Taymaz, T., J. Jackson, and D. McKenzie, “Active tectonics of the north and central Aegean Sea”, *Geophys. J. Int.*, Vol. 106, pp. 433–490, 1991.

Tirel, C., F. Gueydan, C. Tiberi, and J. P. Brun, “Aegean crustal thickness inferred from gravity inversion, Geodynamical implications”, *Earth Planet. Sci. Lett.*, 228, pp. 267–280, 2004.

Tezel, T., T. Shibutani, and B. Kaypak, “Crustal thickness of Turkey determined by receiver function”. *J Asian Earth Sci*, 75, pp. 36-45, 2013.

Tezel, T., T. Shibutani, and B. Kaypak, “Crustal structure variation in western Turkey inferred from the receiver function analysis”, *Tectonophysics*, Vol. 492, pp. 240-252, 2010.

Tirel, C., J. P. Brun, and E. Burov, “Dynamics and structural development of metamorphic core complexes”, *J. Geophys. Res.*, 113, B04403, 2008.

Tirel, C., F. Gueydan, C. Tiberi, and J. Brun, “Aegean crustal thickness inferred from gravity inversion. Geodynamical implications”, *Earth Planet. Sci. Lett.*, Vol. 228, pp. 267–280, 2004.

Tseng, T. L. and W. P. Chen, “Probing the Southern Indian shield with P-wave receiver-function profiles”, *Bull. Seism. Soc. Am.*, 96, pp. 201-213, 2006.

Vanacore, E.A., T. Taymaz, and E. Saygın, “Moho structure of the Anatolian Plate from receiver function analysis”, *Geophys. J. Int.*, 193, pp. 329–337, 2013.

Van Der Meijde, M., S. Van Der Lee, and D. Giardini, “Crustal structure beneath broad-band seismic stations in the Mediterranean region”, *Geophys. J. Int.*, Vol. 152, pp. 729–739, 2003.

Van Hinsbergen, D.J.J., N. Kaymakçı, W. Spakman, and T. H. Torsvik, “Reconciling the geological history of western Turkey with plate circuits and mantle tomography”, *Earth Planet. Sci. Lett.*, 297, pp. 674–686, 2010.

Van Hinsbergen, D.J.J., “A key metamorphic extensional complex reviewed and restored: the Menderes Massif of western Turkey”, *Earth-Science Reviews*, 102, pp. 60–76, 2010.

Westaway, B., “Present-day kinematics of the Middle East and eastern Mediterranean”, *Journal of Geophysical Research*, Vol. 99, pp. 12071–12090, 1994.

Wdowinski, S., Z. Ben-Avraham, R. Arvidsson, and G. Ekstrom, “Seismo-tectonics of the Cyprian Arc”, *Geophys. J. Int.*, 164, pp. 176–181, 2006.

Wittlinger, G., J. Vergne, P. Tapponnier, V. Farra, G. Poupinet, M. Jiang, H. Su, G. Herquel, and A. Paul, “Teleseismic imaging of subducting lithosphere and Moho offsets beneath Western Tibet”, *Earth planet. Sci. Lett.*, 6974, pp. 1–14, 2004.

Yağmurlu, F., M. Y. Savasçın, and M. Ergun, “Relation of alkaline volcanism and active tectonism within the evolution of Isparta Angle, SW Turkey”, *Journal of Geology*, Vol.105, pp. 717–728, 1997.

Yegorova, T., V. Gobarenko, and T. Yanovskaya, “Lithospheric structure of the Black Sea from 3-D gravity analysis and seismic tomography”, *Geophys. J. Int.*, 193, pp. 287–303, 2013.

Yılmaz, Y., C. Genç, F. Gürer, M. Bozcu, K. Yılmaz, Z. Karacık, Z. Altunkaynak, and A. Elmas, “When did the western Anatolian grabens begin to develop, in Tectonics and Magmatism in Turkey and the Surrounding Area”, *Geological Society of London, Special Publication Vol. 173*, pp. 353–384, 2000.

Zandt, G., and C. J. Ammon, “Continental Crustal composition constrained by measurements of crustal Poisson’s ratio”, *Nature*, 374, pp. 152-154, 1995.

Zhu, L. P., “Crustal structure across the San Andreas Fault, southern California from teleseismic converted waves”, *Earth planet. Sci. Lett.*, 179, pp. 183–190, 2000.

Zhu, L. P. and H. Kanamori, “Moho depth variation in southern California from teleseismic receiver functions”, *J. Geophys. Res.*, 105, pp. 2969–2980, 2000.

Zhu, L. P., B. J. Mitchell, N. Akyol, İ. Çemen, and K. Kekovalı, “Crustal thickness variations in the Aegean region and its implications for the extension of continental crust”, *J. Geophys. Res.*, 111, B01301, 2006.

APPENDIX A: Station Coordinates and Parameters of Crustal Structure

Table A.1. Western Profile

No	Name	Lat(^o)	Lon(^o)	Elev(m)	H (km)	V _p /V _s	V _p (km/s)	V _{pn} (km/s)
1	PHSR	41.630	27.524	262	30.5	1.73	6.2	8.2
2	CRLT	41.128	27.736	217	29.0	1.85	6.2	8.2
3	TKR	40.989	27.535	148	26.0	1.85	6.2	8.2
4	VEL4	40.863	27.459	-900	20.5	1.90	6.2	8.1
5	MRMX	40.609	27.583	687	20.0	2.00	6.2	8.1
6	W01	40.506	27.777	27	21.5	1.95	6.2	8.1
7	W02	40.346	27.862	246	22.5	1.90	6.2	8.0
8	W03	40.108	28.058	112	28.5	1.85	6.2	8.0
9	GONE	40.047	27.686	150	28.5	1.85	6.2	8.0
10	CMHB	40.012	27.970	212	28.5	1.85	6.2	8.0
11	W04	39.918	28.086	397	28.5	1.82	6.2	8.0
12	W05	39.803	27.963	447	30.0	1.82	6.2	8.0
13	BALB	39.640	27.880	159	32.0	1.85	6.2	8.0
14	W06	39.468	27.884	201	31.0	1.66	6.4	8.0
15	W07	39.296	27.921	548	31.5	1.75	6.4	8.0
16	W08	39.204	27.834	277	31.5	1.75	6.4	7.9
17	W09	38.998	27.895	417	31.0	1.75	6.2	7.9
18	AKHS	38.879	27.814	217	30.5	1.75	6.2	8.9
19	W10	38.849	27.874	104	30.5	1.75	6.2	8.0
20	W11	38.703	27.969	91	30.0	1.75	6.2	8.0
21	KTT	38.688	28.093	100	29.5	1.75	6.2	8.0
22	W13	38.559	27.942	72	28.0	1.75	6.2	8.0
23	W12	38.446	28.112	305	27.5	1.75	6.2	8.0
24	W14	38.301	28.049	1198	27.5	1.80	6.1	8.0
25	W15	38.098	28.021	270	25.5	1.80	6.1	8.0
26	BOZ	38.000	28.040	1240	25.5	1.80	6.0	8.0
27	W16	37.960	28.017	670	25.5	1.80	6.0	8.0

28	AYDB	37.946	27.89	1202	25.0	1.80	6.0	8.0
29	W17	37.864	27.999	71	25.0	1.80	6.0	8.0
30	CVD	37.752	28.107	71	25.0	1.82	6.0	8.0
31	W18	37.687	28.027	217	25.0	1.85	6.0	8.0
32	W19	37.549	28.065	88	24.0	1.85	6.0	8.1
33	W20	37.458	28.219	446	24.0	1.85	6.0	8.1
34	W21	37.293	28.128	433	24.0	1.95	5.9	8.0
35	YER0	37.136	28.286	665	23.0	2.25	5.9	8.0
36	CETI	37.003	28.307	45	23.0	1.95	5.9	8.0
37	W22	36.984	28.271	27	23.0	1.95	6.0	8.0
38	W23	36.877	28.262	123	23.0	1.95	6.0	8.0
39	TURN	36.775	28.244	150	23.0	1.95	6.0	7.9
40	ARG	36.216	28.126	181	19.0	1.95	6.0	8.2

Table A.2. Central Anatolia Profile

No	Name	Lat(⁰)	Lon(⁰)	Elev(m)	H (km)	Vp/Vs	Vp (km/s)	Vpn (km/s)
1	KAR	41.043	30.662	51	31.0	1.95	6.3	7.9
2	E01	40.933	30.554	164	32.0	1.92	6.3	7.9
3	E02	40.842	30.671	155	33.0	1.95	6.3	7.9
4	E03	40.675	30.669	76	33.5	1.85	6.3	7.9
5	E04	40.563	30.635	789	33.4	1.85	6.3	7.9
6	GULT	40.432	30.515	933	34.0	1.85	6.3	7.9
7	E05	40.341	30.453	986	35.0	1.85	6.3	7.9
8	E06	40.172	30.496	594	35.0	1.75	6.3	7.9
9	E07	40.054	30.413	233	35.0	1.70	6.3	7.9
10	E08	39.896	30.404	998	36.0	1.70	6.3	7.9
11	BORA	39.880	30.453	900	37.0	1.65	6.3	7.9
12	E09	39.677	30.409	838	37.0	1.75	6.3	7.9
13	DOG	39.528	30.837	1000	37.5	1.65	6.3	7.9
14	E10	39.273	30.452	1207	37.5	1.80	6.3	7.9
15	E11	39.071	30.576	1307	37.5	1.70	6.3	7.9

16	E12	38.770	30.751	1010	38.0	1.70	6.3	7.9
17	BOLV	38.713	30.950	1080	38.5	1.70	6.3	7.9
18	SHUT	38.553	30.551	1180	38.5	1.70	6.3	7.9
19	E13	38.360	30.714	1177	39.0	1.75	6.3	7.9
20	E14	38.168	30.636	1092	39.0	1.75	6.3	7.9
21	E15	37.981	30.673	1372	36.0	1.75	6.3	7.9
22	ISP	37.822	30.522	1024	35.0	1.80	6.3	7.9
23	E16	37.585	30.632	1107	36.0	1.80	6.3	7.9
24	BCK	37.461	30.587	919	38.0	1.84	6.3	7.9
25	E17	37.320	30.713	692	39.0	1.85	6.3	7.9
26	E18	37.163	30.681	375	40.0	1.88	6.3	7.9
27	E19	37.027	30.675	301	41.0	1.85	6.3	7.9
28	ANTB	36.899	30.653	42	42.0	1.95	6.3	7.9
29	E20	36.766	30.458	941	42.0	1.85	6.3	7.9
30	E21	36.650	30.535	114	42.0	1.85	6.3	7.9
31	E22	36.490	30.441	554	42.0	1.85	6.3	7.9
32	E23	36.366	30.430	199	42.0	1.85	6.3	7.9

Table A.3. Broadband Stations

Name	Lat (°)	Lon (°)	Elevation (km)	H (km)	Vp/Vs
ADVT	40.433	29.738	190	32.9021	1.690
AHLR	40.887	32.773	1240	37.6670	1.790
ALN	40.896	26.050	110	31.8000	1.800
ALT	39.055	30.110	1060	35.0001	1.640
ALTM	41.088	28.740	0	29.0000	1.800
ARMT	40.568	28.866	320	29.8522	1.750
ATI	40.138	27.653	620	30.9083	1.780
AYDB	37.947	27.891	1250	24.2006	1.980
BAG	38.655	26.852	90	27.8449	1.800
BALB	39.640	27.880	120	31.6061	1.850
BALY	39.740	27.619	650	31.2488	1.800

BBD	37.802	28.853	910	31.1742	1.850
BCK	37.461	30.588	860	35.08161	1.850
BEL	37.971	31.265	1240	37.6233	1.840
BGKT	41.181	28.773	80	29.8000	1.700
BLCB	38.385	27.042	150	29.0173	1.695
BLKV	40.861	32.752	1270	36.3928	1.920
BODT	37.062	27.310	380	24.2654	1.850
BORA	39.880	30.453	960	36.4123	1.650
BOZX	40.534	28.782	120	29.8072	1.770
BUYB	40.852	29.118	230	26.0885	1.800
BYDR	40.824	32.774	1210	37.4081	1.780
BZGM	40.172	26.986	160	29.5255	1.870
CAM	38.748	27.312	0	26.6000	1.740
CANB	40.017	27.062	230	29.6363	1.880
CAVI	40.202	29.838	670	31.8340	1.650
CDK	40.968	32.185	1050	37.4560	1.740
CETI	37.003	28.307	0	23.2000	1.860
CHBY	38.582	32.890	1086	38.0004	1.600
CHOS	38.387	26.051	850	25.4954	1.810
CINR	40.614	29.075	0	28.1092	1.870
CIV	38.411	29.838	1100	32.1092	1.850
CMA	39.257	28.491	660	33.4089	1.690
CMHB	40.012	27.970	200	29.0884	1.840
CMLK	40.965	32.794	1360	37.4976	1.820
CRLT	41.137	27.738	230	28.4787	2.000
CTKS	41.237	28.507	50	34.0500	1.750
CTYL	41.476	28.290	80	32.1485	1.760
DAD	39.908	32.753	880	35.7328	1.760
DALT	36.769	28.637	550	24.4644	1.900
DEMI	39.043	28.716	920	30.4370	1.780
DGB	38.052	26.883	20	25.6533	1.790
DKL	39.071	26.905	35	29.0887	1.840

DOG	39.528	30.837	1000	35.5730	1.690
DURS	39.601	28.474	960	34.0480	1.740
DUV	38.220	27.449	250	27.7902	1.680
EDC	40.347	27.863	300	29.9191	1.740
EDRB	41.847	26.744	210	32.2265	1.630
ELBA	41.147	28.431	330	23.4773	1.860
ELL	36.748	29.909	1230	33.1497	1.820
ENEZ	40.736	26.153	100	27.4082	1.920
ERE	39.748	30.029	0	28.200	1.750
ERIK	40.671	26.513	40	30.6010	1.730
ERMK	36.641	32.911	1855	38.0394	1.920
ESK	40.607	28.945	20	25.0982	1.750
EVK	39.024	27.609	380	29.3668	1.900
EZN	39.827	26.326	50	27.4449	1.850
FETY	36.635	29.084	210	27.5969	1.760
GAZI	36.235	32.316	390	29.8699	1.670
GBZX	40.787	29.450	270	28.0979	1.800
GCAM	37.700	27.233	40	26.4638	1.750
GDZ	39.089	29.481	1370	33.0774	1.810
GELI	40.398	26.474	130	30.4940	1.850
GEMT	40.435	29.189	220	28.6416	1.860
GLHS	37.156	29.498	1100	30.4205	1.800
GOLH	37.236	29.559	1090	35.6479	1.700
GONE	40.047	27.686	140	29.1721	1.870
GULT	40.432	30.515	942	33.8912	1.860
GUN	37.515	29.493	1100	34.1224	1.800
GYTE	40.812	29.349	10	28.6807	1.950
HAR	38.341	28.799	900	31.2188	1.740
HDMB	36.964	32.486	1950	35.3463	1.890
HIS	39.157	32.865	1390	34.0523	1.950
HYRS	40.790	29.262	0	24.4441	1.800
IGD	40.264	29.201	150	26.4241	1.870

INL	36.129	32.550	380	28.7743	1.610
ISK	41.066	29.059	130	30.0750	1.800
ISP	37.843	30.509	1100	37.8727	1.870
JMB	42.491	26.530	250	32.6386	1.780
KAS	36.213	29.684	510	33.4284	1.850
KCTX	40.263	28.335	450	27.0975	1.850
KDHN	38.521	32.116	1120	37.6363	1.730
KHAL	38.370	29.492	1140	31.5528	1.710
KIZT	38.881	31.883	1222	36.1373	1.650
KKZM	41.127	27.345	150	27.4998	1.950
KLYT	41.253	29.042	30	29.2075	1.960
KMR	40.418	27.069	40	32.4535	1.750
KNL	40.271	27.526	30	31.4960	1.780
KONT	37.945	32.361	1100	38.6804	1.830
KORT	37.001	30.350	1300	37.3239	1.850
KOY	39.544	27.164	230	27.2314	1.760
KRB	40.262	28.335	0	29.2000	1.620
KRBG	40.393	27.298	70	29.6038	1.750
KRC	40.263	28.335	440	27.8075	1.740
KTT	38.688	28.093	490	31.0962	1.720
KULA	38.514	28.661	920	30.4072	1.710
KZB	38.881	31.883	1240	35.7373	1.670
LADK	38.200	32.365	1170	36.2579	1.800
LAP	40.370	26.759	230	33.4416	1.900
LEF	35.112	32.843	150	26.4196	1.820
LOD	39.889	32.764	900	37.0000	1.780
MAN	36.782	31.725	210	36.1110	1.680
MARM	40.967	27.960	0	26.2000	1.930
MDNY	40.371	28.885	110	32.3793	1.700
MDUB	40.471	31.198	1109	38.7270	1.820
MFTX	40.787	27.281	920	28.8584	1.880
MLSB	37.295	27.776	500	24.7434	1.950

MRMT	40.606	27.584	213	23.6175	2.020
MSDM	40.349	28.600	0	28.4000	1.940
MYCM	41.032	27.713	0	29.4000	1.820
NEV	39.954	27.263	330	29.8324	1.770
ORE	38.024	28.328	930	28.0130	1.780
PASA	40.869	32.624	990	37.8272	1.780
PHSR	41.631	27.524	260	32.1419	1.710
POL	39.617	32.058	860	36.5160	1.820
RKY	40.688	27.178	690	28.1590	1.700
SART	40.689	27.180	800	28.0475	1.710
SAUV	40.740	30.327	165	32.8423	1.800
SEK	40.198	31.719	750	34.4699	1.740
SGTM	40.767	27.108	0	30.0000	1.880
SHUT	38.553	30.551	1220	36.3763	1.750
SIMA	39.083	28.982	984	32.0561	1.730
SLV	41.073	28.140	30	28.9836	1.800
SVRH	39.447	31.523	1000	36.1314	1.700
TIRR	44.458	28.413	77	36.7000	1.590
TROY	40.110	26.418	100	28.8388	1.960
TVSB	39.450	29.462	1090	35.9000	1.710
UMT	39.352	29.168	1330	34.2637	1.770
YNC	37.814	28.573	250	29.8316	1.780
ZKR	35.115	26.217	270	27.2907	1.950